UNIVERSITÀ DEGLI STUDI DI TORINO

Facoltà di Scienze Matematiche, Fisiche e Naturali

Dottorato di ricerca in Fisica XV ciclo

Study of spin observables in COMPASS

Candidato

Andrea Ferrero

Relatore

Prof.sa Maria Pia Bussa

Correlatore

Dott. Angelo Maggiora

Coordinatore del ciclo

Prof. Ezio Menichetti

2000-2002

ad Anna.

Introduction

In the Deep Inelastic Scattering (DIS) experiments, a beam of leptons, either electrons, muons or neutrinos, interacts with the nucleons of a polarized target, through the exchange of a virtual photon. The virtual photon acts as an high energy probe of the structure of the nucleon, with a resolution given by its associated wavelength $\hbar/Q^2$ (Q^2 is the virtual photon four-momentum squared).

COMPASS belongs to this typology of experiments, and uses the longitudinally polarized 160 GeV muon beam produced in the M2 beamline of the Super Proton Synchrotron (SPS) at CERN. Other experiments in the past, like EMC and SMC, have used the same muon beam to investigate the nucleon spin structure. In particular EMC has studied the quark contribution to the nucleon spin, and the small measured value has lead to the so-called "proton spin crisis" and to a huge theoretical and experimental effort to accommodate this surprising result with the present understanding of the nucleon structure. Any improvement in this field requires from the experimental side the separate measurement of the contributions to the nucleon spin by each quark flavor and by the gluons.

COMPASS has been designed to answer questions like: how large is the gluonic contribution to the nucleon spin? Or: are strange sea-quarks anti-

correlated with the nucleon spin? Moreover, it has the possibility to give new informations on the transversity distribution $h_1(x)$, which describes the spin dynamics of quarks in a transversely polarized nucleon and is almost experimentally unknown. Together with the helicity-averaged and helicity-dependent distribution functions, $h_1(x)$ provides the complete twist-2 description of the nucleon internal structure.

The COMPASS apparatus has been designed to reconstruct the DIS process in a wide kinematical range, from quasi-real photon exchange ($Q^2 \approx 0$ (GeV)^2) up to $Q^2 \simeq 40$ (GeV)^2. This is obtained using a double magnetic spectrometer with complementary kinematical ranges. The Large Angle Spectrometer (LAS) has a large angular acceptance and is designed to reconstruct low momenta hadrons and large Q^2 muons; particle identification is provided by a Ring Image Cherenkov (RICH) detector. The Small Angle Spectrometer (SAS) is designed to reconstruct particles with momentum $p > 10$ GeV/c, using a MultiWire Proportional Chambers (MWPC) and a Gas Electron Multipliers (GEM) tracking system. In particular the MWPC system is fundamental for the tracking of scattered muons in the low Q^2 region. The MWPC project has been part of the work of the thesis presented here, and has been successfully completed with the installation of 10 stations in year 2001 and 1 additional station in year 2002.

In year 2002 part of the COMPASS data taking has been devoted to the study of transversity. This new and challenging measurement requires, in the case of lepton-nucleon DIS, the measurement of a semi-inclusive reaction. In this thesis the Λ^0 hyperon production channel has been chosen and a preliminary study of spin observables will be presented. The self-analyzing properties of the weak decay $\Lambda^0 \to p\pi^-$ allow to investigate spin transfer effects from the struck nucleon to the final state Λ^0, while the dependence of the Λ^0 production cross-section on the *transverse* target spin direction can provide new informations on the transversity quark distributions. The availability of transversity data in COMPASS is only recent and the analysis is ongoing, but some preliminary results on single spin asymmetries are already available and will be presented

here.

Outline of the thesis

This thesis describes the measurement of polarized semi-inclusive DIS with the COMPASS spectrometer at CERN, with particular highlights on the Λ^0 production channel.

In chapter 1 I will introduce the physics of the lepton Deep Inelastic Scattering, both with unpolarized and polarized beam and target. I will discuss the current status of understanding of the nucleon spin structure, and describe the new measurements planned for the COMPASS experiment. I will focus my attention on the Λ^0 production in polarized semi-inclusive DIS (SIDIS) as a powerful tool to get new informations on the polarized quark distribution functions of the nucleon. As a special case, I will describe the transverse target spin configuration and the associated spin observables which can be extracted from polarized SIDIS.

COMPASS is a challenging experiment not only from the physics point of view. The design performances of 100 kHz trigger rate and 2 TBytes/day of data rate, with a total of $\sim$ 250 000 readout channels, are at the edge of modern readout and data acquisition technologies. The experimental apparatus and the Data Acquisition (DAQ) system are described in chapter 2.

Tracking in the SAS is mainly based on a MultiWire Proportional Chambers (MWPC) and Gas Electron Multipliers (GEM) system. In chapter 3 I will introduce the main features of MWPC relevant for the COMPASS case, and I will describe the detectors installed in COMPASS. I will also discuss the choice

of the proper gas mixture needed for the particle flux and to fulfill the dead time requirements of the COMPASS experiment. The readout electronics and the laboratory tests I performed during the development and commissioning will be presented.

The performances of MWPC detectors during the 2001 and 2002 data taking periods are discussed in chapter 4. Results on noise performances, efficiency, crosstalk, spatial and time resolutions are presented both for the laboratory measurements and for the analysis of the available data. Many results are obtained using a dedicated tracking system fast enough to perform online analysis, which is described in the appendices. An effective data selection criterion which could enhance the tracking efficiency by reducing the detector hit multiplicity is suggested at the end of the chapter.

The analysis which is ongoing on the data of the 2002 run is described in chapter 5. The proposed measurement of spin observables in the Λ^0 production channel with transverse target spin are introduced, and the MonteCarlo simulations performed to study the apparatus acceptance are presented. A large amount of work has been devoted to the selection of the Λ decay events and their separation from the background. The selection criteria are described in detail through that chapter, and the purity of the selected Λ^0 sample is evaluated from MonteCarlo analysis. Finally the preliminary results on single spin asymmetries are presented both for the Λ^0 and the K^0 samples.

The conclusions on the thesis can be found in chapter 6.

Introduzione

Negli esperimenti di urto profondamente inelastico (DIS), un fascio di leptoni, siano essi elettroni, muoni o neutrini, interagisce con i nucleoni di un bersaglio polarizzato, attraverso lo scambio di un fotone virtuale. Il fotone virtuale agisce come una sonda di alta energia che rivela la struttura dei nucleoni del bersaglio, con una risoluzione data dalla sua lunghezza d'onda associata $\hbar/Q^2$ (Q^2 è il quadrato del quadrimpulso del fotone).

COMPASS appartiene a tale tipologia di esperimenti, ed usa il fascio di muoni polarizzati longitudinalmente prodotto nella linea di fascio M2 del Super ProtoSincrotrone (SPS) del CERN. Altri esperimenti nel passato, come EMC ed SMC, hanno utilizzato la stessa linea di fascio per investigare la struttura dei nucleoni. In particolare EMC ha studiato il contributo dei quark allo spin dei nucleoni, ed il piccolo valore misurato ha portato alla cossiddetta "crisi dello spin del protone" e ad un enorme sforzo sia teorico che sperimentale per spiegare tale sorprendente risultato con le attuali conoscenze della struttura del nucleone. Qualunque progresso in tale campo richiede dal punto di vista sperimentale la misura separata dei contributi allo spin del nucleone dei gluoni e di ciascun tipo di quark.

COMPASS è stato progettato per rispondere a domande del tipo: quanto è

grande il contributo dei gluoni allo spin del nucleone? Oppure: i quark strani del mare sono anticorrelati con lo spin del nucleone? Inoltre, COMPASS ha la possibilità di rivelare nuove informazioni sulla funzione di trasversità $h_1(x)$, che descrive la dinamica dello spin in un nucleone polarizzato trasversalmente ed è sostanzialmente sconosciuta dal punto di vista sperimentale. Assieme alle funzioni di distribuzione mediate sull'elicità e dipendenti dall'elicità, $h_1(x)$ fornisce la completa descrizione al twist-2 della struttura interna dei nucleoni.

L'apparato sperimentale di COMPASS è stato progettato per ricostruire il processo di DIS in un largo intervallo cinematico, dallo scambio di fotoni quasi reali ($Q^2 \approx 0$ (GeV)^2) fino a $Q^2 \simeq 40$ (GeV)^2. Tale risultato è ottenuto mediante l'utilizzo di un doppio spettrometro magnetico, con intervalli cinematici complementari. Lo spettrometro a largo angolo (LAS) ha una grande accettanza angolare ed è progettato per ricostruire gli adroni con basso impulso ed i muoni a grande Q^2; l'identificazione delle particelle è fornita dal un rivelatore Ring Image Cherenkov (RICH). Lo spettrometro a piccolo angolo (SAS) è al contrario progettato per ricostruire particelle con impulso $p > 10$ GeV/c, ed utilizza un sistema di tracciamento composto da camere proporzionali multifili (MWPC) e rivelatori "Gas Electron Multiplier" (GEM). In particolare le camere MWPC sono fondamentali per il tracciamento dei muoni nella regione a piccolo Q^2. Il progetto delle MWPC costituisce parte della tesi presentata in questo lavoro, ed è stato completato con successo con l'installazione di 10 stazioni nell'anno 2001 e di un'ulteriore stazione nell'anno 2002.

Nell'anno 2002 una parte della presa dati di COMPASS è stata dedicata allo studio della trasversità. Questa nuova e complessa misura richiede, nel caso del DIS di leptoni su nucleoni, lo studio di una reazione semi-inclusiva. In questa tesi è stato scelto il canale di produzione dell'iperone Λ^0 e verrà presentato uno studio preliminare delle osservabili di spin della reazione. Le proprietà auto-analizzanti del decadimento debole $\Lambda^0 \to p\pi^-$ permettono di studiare gli effetti di trasferimento di spin dal nucleone alla Λ^0 nello stato finale, mentre la dipendenza della sezione d'urto di produzione dallo spin trasverso del nucleone potrebbe fornire nuove informazioni sulla struttura di spin trasverso dei quark

nel nucleone. La disponibilità di dati di spin trasverso in COMPASS è solo recente e l'analisi è in corso, ma alcuni risultati preliminari sulle asimmetrie singole di spin sono attualmente disponibili e saranno presentati in questa tesi.

Struttura della tesi

Questa tesi descrive misure di DIS polarizzato semi-inclusivo ottenute con l'apparato sperimentale di COMPASS al CERN, con particolare attenzione al canale di produzione di Λ^0.

Nel capitolo 1 introdurrò la fisica del DIS, con leptoni e bersagli sia polarizzati che non polarizzati. Presenterò lo stato attuale della conoscenza della struttura di spin del nucleone, e descriverò le nuove misure previste nel programma dell'esperimento COMPASS. Focalizzerò la mia attenzione sulla produzione di Λ^0 nel DIS semi-inclusivo polarizzato (SIDIS polarizzato) quale potente strumento per estrarre nuove informazioni sulle funzioni di distribuzione dipendenti dallo spin del nucleone. Descriverò la configurazione di spin trasverso del bersaglio quale caso speciale, ed introdurrò le osservabili di spin che possono essere studiate nel DIS polarizzato.

COMPASS è un esperimento innovativo non solo dal punto di vista del programma fisico. La frequenza massima di trigger di 100 kHz e il flusso di dati raccolti, pari a 2 TBytes al giorno, con un numero totale di canali di lettura pari a ~ 250000, sono al limite delle attuali tecnologie di lettura ed acquisizione dati. L'apparato sperimentale ed il sistema di acquisizione (DAQ) sono descritti nel capitolo 2.

Il tracciamento nello spettrometro SAS è basato principalmente su un sis-

tema di camere MWPC e GEM. Nel capitolo 3 introdurrò le principali caratteristiche dei rivelatori MWPC, con particolare riguardo agli aspetti rilevanti per il loro utilizzo in COMPASS, e descriverò i rivelatori utilizzati in COMPASS. Discuterò anche la scelta della miscela di gas più appropriata, in relazione al flusso di particelle ed al massimo tempo morto di rivelazione consentito dal sistema di acquisizione dell'esperimento. Nel capitolo descriverò anche l'elettronica di lettura ed i test che ho svolto durante la fase di sviluppo della stessa.

Le prestazioni dei rivelatori MWPC durante i periodi di presa dati del 2001 e 2002 sono discusse nel capitolo 4. Sono ivi presentati i risultati delle misure di rumore, efficienza, cross-talk e risoluzione spaziale e in tempo, da me ottenuti sia da misure di laboratorio che dall'analisi dei dati disponibili. Molti dei risultati presentati sono ottenuti utilizzando un algoritmo di tracciamento dedicato, la cui velocità è sufficiente per eseguire l'analisi in tempo reale delle prestazioni dei rivelatori. Tale algoritmo è descritto in appendice. Al termine del capitolo è suggerito un efficace metodo di selezione dei dati che potrebbe migliorare le prestazioni del programma di tracciamento, riducendo la molteplicità media dei segnali del rivelatore.

L'analisi, attualmente in corso, dei dati acquisiti nel corso del 2002 è presentata nel capitolo 5. In tale capitolo è inoltre descritta la misura proposta delle osservabili di spin nel canale di produzione di Λ^0, assieme alle simulazioni MonteCarlo svolte per studiare l'accettanza dell'apparato. Una notevole quatità di lavoro è stata dedicata allo studio del miglior metodo di selezione degli eventi di decadimento della Λ^0 ed alla loro separazione dal fondo. I criteri di selezione adottati sono descritti in dettaglio nel capitolo, assieme alle stime di purezza del campione di Λ^0 ottenute dall'analisi delle simulazioni Montecarlo. I risultati preliminari sulla misura delle asimmetrie singole di spin sono presentati alla fine del capitolo, sia per il campione delle Λ^0 che per quello dei K^0.

Nel capitolo 6 sono presentate le conclusioni della tesi.

Contents

1 Seminclusive Λ production from polarized targets **1**
1.1 Lepton-nucleon scattering process 2
1.1.1 Kinematics 2
1.1.2 The inclusive DIS cross-section 3
1.1.3 Unpolarized lepton-nucleon scattering 5
1.1.4 Polarized lepton-nucleon scattering 6
1.1.5 Sum rules 9
1.1.5.1 The nucleon spin and the Ellis-Jaffe sum rules . 10
1.2 EMC and the "proton spin crisis" 11
1.3 Gluon polarization $\Delta G/G$ and COMPASS 12
1.4 Polarization of strange sea quarks of the nucleon 14
1.4.1 Λ polarization in deep inelastic lepton scattering 15
1.4.2 Target fragmentation region 15
1.5 The transverse spin of the nucleon 16
1.6 Λ production with a transversely polarized target 18

2 The experimental apparatus **20**
2.1 The M2 beamline 21
2.2 The polarized target 25
2.3 Tracking system 28
2.3.0.1 Beam definition 28
2.3.0.2 Muon trigger 28
2.3.0.3 Calorimetry 32

2.3.0.4 Event reconstruction and particle identification 33
2.4 Data Acquisition System 43

3 The COMPASS MWPC detector and electronics 46
3.1 Introduction 46
3.2 Principle of operation 46
3.2.0.5 Electrical field in a multiwire structure 46
3.3 Detector characteristics 48
3.4 Choice of the gas mixture 49
3.4.0.6 Characteristics of the wire signal 51
3.5 Readout electronics 53
3.5.1 Laboratory tests of front-end chips 57
3.5.2 Tests with small chamber prototipe 59
3.6 Online test system 67
3.6.0.1 VME control board 67
3.6.0.2 Pulser box 68

4 MWPC detector performances during 2001-2002 data taking 71
4.1 Introduction 71
4.2 Laboratory tests of MWPC detectors 72
4.2.0.3 Noise performances 72
4.2.0.4 Detector efficiency measurement 73
4.2.0.5 Crosstalk measurement 75
4.3 Analysis of 2002 data 76
4.3.1 Efficiency measurement 77
4.3.2 Spatial resolution 79
4.3.3 Hit timing analysis 84
4.3.3.1 Track time and MWPC timing resolution measurement 85
4.3.3.2 Time-based cluster rejection 88

5 Analysis of 2002 data set with transverse target spin 92
5.1 The analyzing power 93
5.2 Useful symmetries 94
5.3 MonteCarlo simulations 96
5.4 Λ vertex selection 99
5.5 MonteCarlo analysis of apparatus asymmetries 103
5.6 Measurement of $A_Y^{\uparrow(\downarrow)}$ in real data 104
5.7 Kaon contamination and asymmetries 111

6 Conclusions 115

A Calibration procedure of MWPC frontend electronics 118

B Tracking algorithm for MWPC efficiency analysis 122
B.0.0.3 Space points reconstruction 123
B.0.0.4 Candidate track finding 123
B.0.0.5 Track fitting & merging 124

C Target acceptance correction by means of independent measurements with opposite cell polarizations 128
C.0.0.6 Statistical error 132
C.0.0.7 Second-order acceptance corrections 132
C.0.0.8 A_Y measurement using left/right data samples . 133

Bibliography 135

Chapter 1

Seminclusive Λ production from polarized targets

The scattering of polarized leptons on polarized nucleon targets has been used since 1974 by several experiments to probe the structure of the nucleons and to measure the partonic and gluonic contribution to the total nucleon spin.

The data from polarized lepton-nucleon deep-inelastic scattering (DIS) show that the spin structure of nucleons is much more complicated than what is described by the parton model. The experimental results suggest that contributions from sea-quarks, gluons and their angular momenta can be significant. In this context measurements of spin dependent structure functions for the individual gluon and strange quark contributions are needed. Moreover, the transversity distribution $h_1(x)$, which is the equivalent of the $g_1(x)$ for a transversely polarized target, is currently of great theoretical interest. The measurement of $h_1(x)$ involves the study of semi-inclusive hadron leptoproduction, and requires additional informations on the quark fragmentation functions available from polarized proton-proton scattering.

In this chapter I will describe the physics of polarized DIS and sketch the measurements that are foreseen in COMPASS, with a special highlight on seminclusive Λ leptoproduction and on the feasibility of the measurement of $h_1(x)$ in this particular channel.

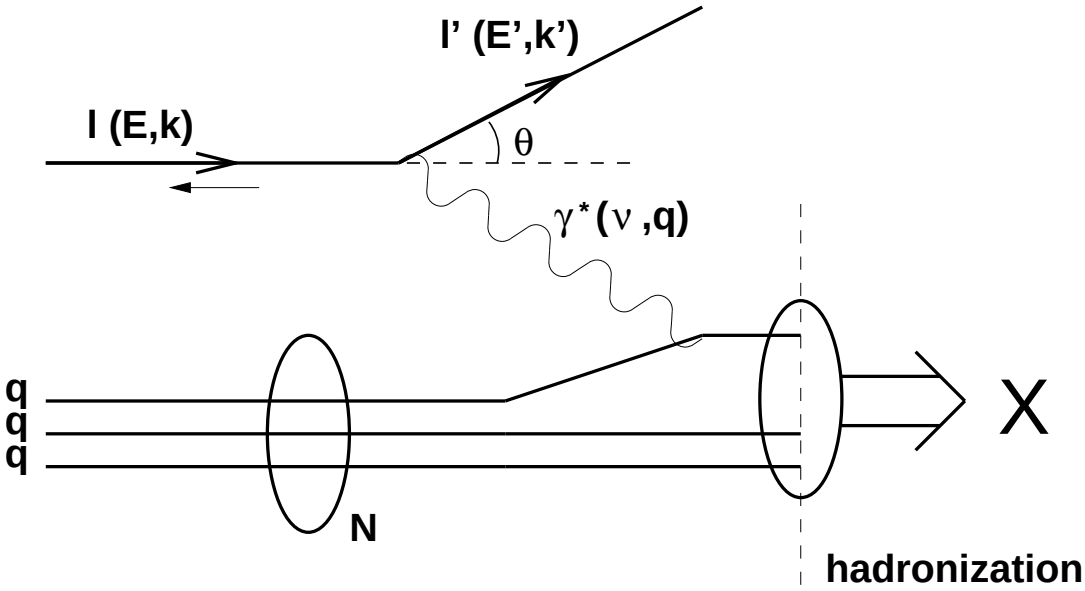

Figure 1.1: *Deep-inelastic lepton-nucleon scattering process. The lepton emits a virtual photon which is absorbed by one of the quarks in the nucleon. The struck quark and the target remnants fragment into hadrons in the final state.*

1.1 Lepton-nucleon scattering process

In the lepton-nucleon DIS, schematically depicted in Fig. 1.1, an incoming lepton emits a virtual photon which is absorbed by a quark in the nucleon (struck quark). As a consequence, the nucleon breaks up and the struck quark and the target remnants fragment into hadrons in the final state. In the inclusive DIS measurement only the incoming and scattered leptons are detected. Semi-inclusive measurements require the additional detection of one of the hadrons in the final state, and provide additional informations on the nucleon structure and on the properties of the DIS process.

1.1.1 Kinematics

The lepton-nucleon DIS kinematics is usually described by the following Lorentz-invariant variables:

1. The squared four-momentum transfer,

$$Q^2 = -q^2 = -(k - k')^2 = 4EE' \sin^2(\theta/2); \tag{1.1}$$

2. the energy transfer to the hadronic system,

$$\nu = p \cdot q/M = E - E'; \tag{1.2}$$

3. the square of the invariant mass of the photon-nucleon system,

$$W^2 = M^2 + 2M\nu - Q^2; \tag{1.3}$$

4. the Bjorken scaling variable,

$$x = Q^2/2p \cdot q = Q^2/2M\nu; \tag{1.4}$$

5. the fraction of the incident energy transferred,

$$y = p \cdot q/p \cdot k = \nu/E. \tag{1.5}$$

In these equations, k, k', p and q are the four-vectors of the incoming and scattered lepton, the target nucleon and the exchanged boson. M is the mass of the target nucleon, whereas the lepton mass is not considered. E, E' are the energies of the incident and scattered lepton, and θ the lepton scattering angle in the laboratory frame.

1.1.2 The inclusive DIS cross-section

The inclusive lepton-nucleon DIS cross-section can be expressed as

$$\frac{d^2\sigma}{d\Omega dE'} = \frac{\alpha^2}{2MQ^4}\frac{E'}{E}\, L_{\mu\nu}W^{\mu\nu} \tag{1.6}$$

where α is the fine structure constant and M is the mass of the target nucleon. $L_{\mu\nu}$ is a tensor which describes the lepton-photon vertex; it can be calculated exactly in the framework of Quantum Electro Dynamics (QED):

$$L_{\mu\nu} = \sum_{\lambda'} \left[\bar{u}(k', \lambda')\gamma_\mu u(k, \lambda)\right] \left[\bar{u}(k', \lambda')\gamma_\nu u(k, \lambda)\right]^*, \tag{1.7}$$

where k (k') and λ (λ') are the four-momentum and the helicity of the incoming (scattered) lepton, $u(k,\lambda)$ is the Dirac spinor, γ_μ are the Dirac matrices, and $\epsilon_{\mu\nu\alpha\beta}$ is the totally antisymmetric Levi-Civita tensor. In the expression for $L_{\mu\nu}$ an implicit summation is performed over repeated indexes. The $L_{\mu\nu}$ can be factorized in two terms, one symmetric (S) and one anti-symmetric (A) under the exchange of the μ and ν indexes:

$$L_{\mu\nu} = 2L^S_{\mu\nu} + 2iL^A_{\mu\nu}, \tag{1.8}$$

$$L^S_{\mu\nu} = k_\mu k'_\nu + k'_\mu k_\nu - g_{\mu\nu} k \cdot k', \tag{1.9}$$

$$L^A_{\mu\nu} = \lambda \epsilon_{\mu\nu\rho\beta} k^\rho k'^\beta. \tag{1.10}$$

The tensor $W^{\mu\nu}$ describes the absorption of the virtual photon by the nucleon; it contains the whole information about the unknown nucleon structure, and there is not an exact calculation for it. The form of the $W_{\mu\nu}$ tensor can be derived from symmetry considerations and conservation laws; as for $L_{\mu\nu}$, it can be splitted into symmetric and anti-symmetric terms [4]:

$$W_{\mu\nu} = W^S_{\mu\nu} + iW^A_{\mu\nu}, \tag{1.11}$$

$$W^S_{\mu\nu} = -g_{\mu\nu}\ F_1(\nu, Q^2) + \frac{p_\mu p_\nu}{\nu}\ F_2(\nu, Q^2), \tag{1.12}$$

$$W^A_{\mu\nu} = \frac{\epsilon_{\mu\nu\alpha\beta}\ q^\alpha s^\beta}{\nu}\ g_1(\nu, Q^2) + \frac{\epsilon_{\mu\nu\alpha\beta}\ q^\alpha (p\cdot q\ s^\beta - s\cdot q\ p^\beta)}{\nu^2}\ g_2(\nu, Q^2). \tag{1.13}$$

Taking into account the fact that the product of a symmetric tensor with and anti-symmetric one is null, the DIS cross-section can be written as

$$\frac{d^2\sigma}{d\Omega dE'} = \frac{\alpha^2}{2MQ^4}\frac{E'}{E}\ \left[L^{(S)}_{\mu\nu} W^{\mu\nu(S)} - L^{(A)}_{\mu\nu} W^{\mu\nu(A)}\right]. \tag{1.14}$$

The symmetric and the anti-symmetric terms in square brackets in eq. 1.14 are related to the unpolarized and to the polarized DIS processes respectively.

1.1.3 Unpolarized lepton-nucleon scattering

When the DIS cross-section is averaged over all the possible spin states of the incoming and outgoing lepton and over those of the target (unpolarized DIS), the differential cross-section is expressed by

$$\frac{d^2\sigma}{dQ^2dx} = \frac{4\pi\alpha^2}{Q^2}\frac{1}{x}\left[xy^2F_1(\nu,Q^2) + \left(1 - y - \frac{Mxy}{2E}\right)F_2(\nu,Q^2)\right] \tag{1.15}$$

In passing from eq. 1.14 to eq. 1.15 the azimuthal lepton emission angle Φ has been integrated over the 2π range and a transformation $dE'd\cos\theta \rightarrow dQ^2dx$ has been performed.

When $(\nu, Q^2) \rightarrow \infty$ but the ratio ν/Q^2, and therefore x, remains finite (Bjorken limit), the structure functions are no more dependent on both Q^2 and ν, but they are only functions of one variable $x = Q^2/2M\nu$ (Bjorken scaling). The dependence on a single kinematical variable is typical of the scattering off point-like particles. If the nucleon is considered in a reference frame where its momentum is infinite, the transverse momentum of the partons inside the nucleon can be neglected and the x variable is interpreted as the fraction of the nucleon momentum carried by the struck parton.

In the Quark Parton Model (QPM), the scaling phenomenon has been interpreted as due to the incoherent sum of scattering processes between the lepton and point-like spin-$\frac{1}{2}$ constituents of the nucleon, called quarks.

The structure functions $F_1(x)$ and $F_2(x)$ have a simple interpretation in the Quark Parton Model (QPM):

$$F_1(x) = \frac{1}{2}\sum_i e_i^2\left[q_i(x) + \bar{q}_i(x)\right] \tag{1.16}$$

$$F_2(x) = \sum_i e_i^2 x\left[q_i(x) + \bar{q}_i(x)\right], \tag{1.17}$$

where $q_i(x)$ ($\bar{q}_i(x)$) is the probability to find a quark (anti-quark) of flavor i and carrying a fraction x of the momentum of the nucleon, and e_i the charge of the quark flavor i. In the hypotesis of spin-$\frac{1}{2}$ quarks, the two structure functions $F_1(x)$ and $F_2(x)$ obey the so-called Callan-Gross relation:

$$F_2(x) = 2xF_1(x). \tag{1.18}$$

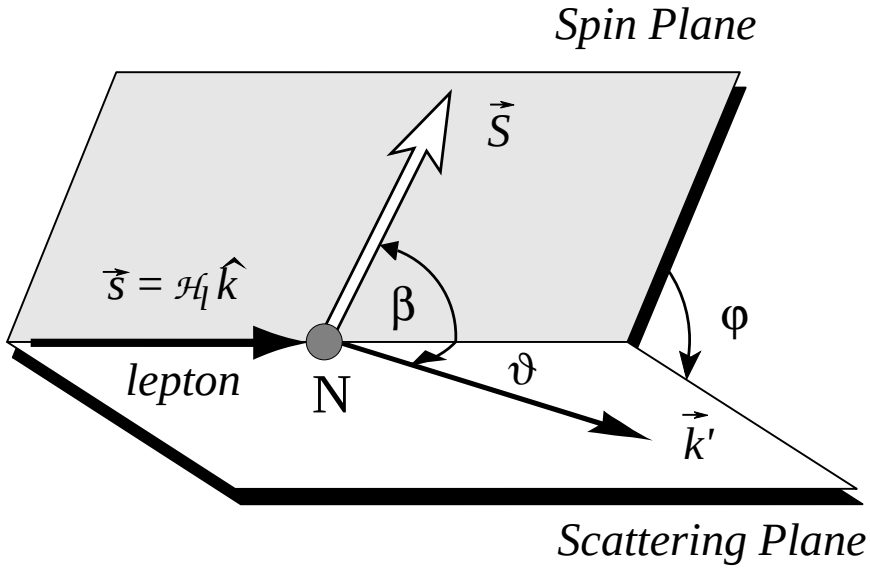

Figure 1.2: *Kinematics of polarized deep-inelastic lepton-nucleon scattering*

1.1.4 Polarized lepton-nucleon scattering

Let's now turn to the case of a longitudinally polarized lepton beam and a polarized target. The differential cross-section additionally depends on the relative direction of the target spin and of the incoming lepton momenta. It is useful to introduce two planes, the scattering plane and the spin plane, defined respectively by the directions of the incoming and scattered lepton, and of the incoming lepton and target spin axis (see Fig. 1.2). The corresponding cross-section can be decomposed into a spin-independent term σ_0 and a spin-dependent contribution $\Delta\sigma$[2]:

$$\frac{d^3\sigma(\beta)}{dQ^2\ dx\ d\phi} = \frac{d^3\sigma_0}{dQ^2\ dx\ d\phi} - \frac{d^3\Delta\sigma(\beta)}{dQ^2\ dx\ d\phi}, \tag{1.19}$$

where the β represents the angle between the target spin vector and the incoming lepton momentum vector, and ϕ is the angle between the scattering and the spin planes, as shown in Fig. 1.2.

The spin-independent part $\frac{d^3\sigma_0}{dQ^2\ dx\ d\phi}$ of the cross-section is given by eq. 1.15, while the spin-dependent part $\frac{d^3\Delta\sigma(\beta)}{dQ^2\ dx\ d\phi}$ contains the structure functions $g_1(\nu, Q^2)$

and $g_2(\nu, Q^2)$, related to the anti-symmetric part of the hadronic tensor $W_{\mu\nu}$ (see eq. 1.13). It can be expressed as

$$\frac{d^3\Delta\sigma(\beta)}{dQ^2\ dx\ d\phi} \propto \cos(\beta)\left[a\ g_1(\nu,Q^2) + b\ g_2(\nu,Q^2)\right] - \cos(\phi)\ \sin(\beta)\ c\ \left[\frac{y}{2}\ g_1(\nu,Q^2) + g_2(\nu,Q^2)\right]. \quad (1.20)$$

The parameters a, b and c are of the order $\mathcal{O}(1)$, $\mathcal{O}(1/Q^2)$ and $\mathcal{O}(1/Q)$ respectively when $Q^2 \to \infty$. Therefore, the distribution $g_1(x)$ dominates at large Q^2 in the first term of the right hand side of the above expression.

The functions $g_1(\nu, Q^2)$ and $g_2(\nu, Q^2)$ present the same scaling properties as $F_1(x)$ and $F_2(x)$. The $g_1(x)$ function has a simple interpretation in the QPM:

$$g_1(x) = \frac{1}{2}\sum_i e_i^2\ \left[(q_i^+(x) + \bar{q}_i^+(x)) - (q_i^-(x) - \bar{q}_i^-(x))\right], \quad (1.21)$$

where $q_i(x)$ ($\bar{q}_i(x)$) is the probability of finding a quark (anti-quark) of flavor i, at a certain value of x. The sign + ($-$) indicates that the spin of the quark is oriented in the same (opposite) direction as the spin of the nucleon. The same interpretation holds for $\bar{q}_i^+(x)$ ($\bar{q}_i^-(x)$) in the case of anti-quarks.

An intuitive picture of how $g_1(x)$ is sensitive to spin degrees of freedom and how it can be measured in polarized lepton-nucleon DIS is given in Fig. 1.3. When a beam of longitudinally polarized leptons is scattered off a longitudinally polarized target, the lepton preferentially emits a circularly polarized virtual photon with spin projection pointing to the right of the picture[4]. Angular momentum conservation requires that the virtual photon is absorbed by a quark with spin oriented in **opposite** direction (pointing to the left of the picture), since the final state quark must have spin 1/2. This corresponds to a value of the angle β appearing in eq. 1.20 of either 0° or 180°. Therefore, only the first term in the right hand side of that equation contributes. In this term the main contribution comes from the $g_1(x)$ distribution, since $g_2(x)$ is suppressed by the parameter b.

When the spin orientation of the nucleon is that of the struck quark (top picture in Fig. 1.3), the cross-section is sensitive to the distribution $q^+(x)$. This

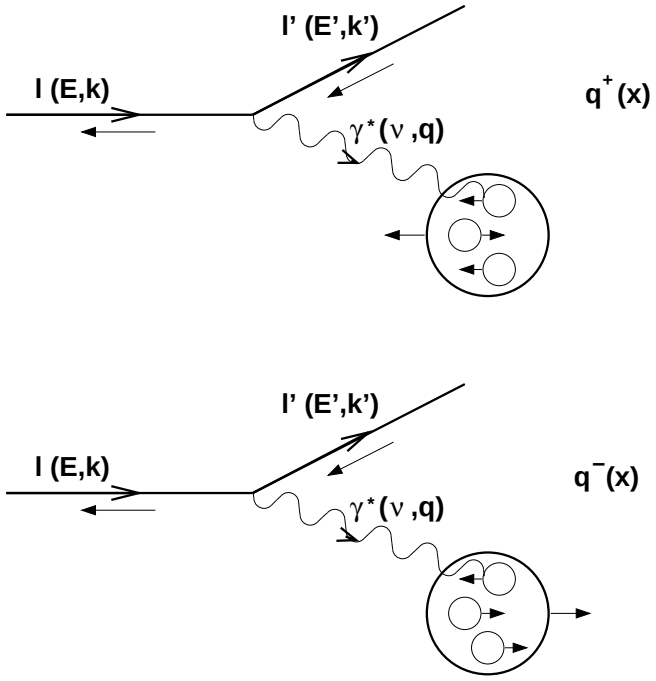

Figure 1.3: *Diagram of polarized deep inelastic scattering. A longitudinally polarized lepton emits a virtual photon that preferentially hits a quark with opposite spin orientation. The upper diagram is therefore sensitive to the $q^+(x)$ distribution, while the bottom one is sensitive to $q^-(x)$ (see text).*

cross-section will be denoted as $\sigma^{\uparrow\downarrow}$, where $\uparrow$ is the direction of the spin of the incoming lepton and $\downarrow$ is the direction of the nucleon spin. If the target spin is reversed (pointing to the left of the picture) the measured cross-section corresponds to parallel beam and target spins, and is denoted as $\sigma^{\uparrow\uparrow}$ (bottom picture in Fig. 1.3). The elementary photon-quark interaction is however unchanged, because the spin of the struck quark must be oriented anti-parallel to the photon spin. Therefore, the $\sigma^{\uparrow\uparrow}$ cross-section is sensitive to the $q^-(x)$ distribution. The same rule holds when the virtual photon is absorbed by an anti-quark.

In inclusive DIS the flavor of the struck quark is not identified, and a summation over all possible quarks and anti-quarks is implicit in the measurement. From eq. 1.21 it is clear that $g_1(x)$ can be extracted from the double-spin asym-

metry

$$A_{\parallel} = \frac{\sigma^{\uparrow\downarrow} - \sigma^{\uparrow\uparrow}}{\sigma^{\uparrow\downarrow} + \sigma^{\uparrow\uparrow}}. \tag{1.22}$$

As already mentioned, the longitudinal spin asymmetry is dominated by the $g_1(x)$ structure function. To access $g_2(x)$, the target spin has to be oriented perpendicular to the beam direction ($\beta = 90°$ or $270°$), thus selecting the second term in eq. 1.20. However, the asymmetry is in this case suppressed by a factor $c \sim \mathcal{O}(1/Q)$, making the measurement more difficult.

1.1.5 Sum rules

The measurement of the parton distribution functions can give important informations on the validity of the models used to depict the internal structure of the nucleon. The experimental observation of the scaling properties of the $F_1(\nu, Q^2)$ and $F_2(\nu, Q^2)$ structure functions confirmed the hypothesis that the nucleon is made up of point-like, spin 1/2 constituents. The small deviations from the scaling observed have been explained by the Altarelli-Parisi equations in the perturbative QCD (PQCD) theory.

No theoretical predictions are currently available for the x-dependence of the spin-dependent structure functions. Nevertheless definite predictions do exist for the quantities

$$\Gamma_1^N = \int_0^1 g_1^N(x)\ dx, \tag{1.23}$$

where the superscript N denotes the nucleon type (p or n). A certain number of sum rules have been derived, which relate the Γ_1^N to the polarizations Δq_i of the quarks in the nucleon, defined as

$$\Delta q_i = \int_0^1 \left[(q_i^+(x) + \overline{q}_i^+(x)) - (q^-(x) + \overline{q}^-(x))\right]\ dx. \tag{1.24}$$

The most fundamental of these relations is the so-called **Bjorken sum rule**, which predicts the difference of the Γ_1 moments for the proton and the neutron:

$$\Gamma_1^p - \Gamma_1^n = \frac{1}{6}(\Delta u - \Delta d) = \frac{1}{6}\left|\frac{g_A}{g_V}\right|, \tag{1.25}$$

where g_A and g_V are the axial and vector weak coupling constants of the neutron β-decay. The Bjorken sum rule does not rely on a particular model of the internal structure of the nucleons, and is verified at a 10% level by several DIS experiments.

1.1.5.1 The nucleon spin and the Ellis-Jaffe sum rules

The most general expression for the spin of the proton (or the neutron) is given, in units of $\hbar$, by

$$\frac{1}{2} = \frac{1}{2}\Delta\Sigma + \Delta G + L. \tag{1.26}$$

In this expression $\Delta\Sigma = \sum_i \Delta q_i$ is the overall quark contribution to the nucleon spin, and L is the angular momentum contribution. The gluon contribution ΔG is given by

$$\Delta G = \int_0^1 \left[G^+(\eta) - G^-(\eta)\right]\ d\eta, \tag{1.27}$$

where $G^{+(-)}(\eta)$ is the probability of finding a gluon with the spin oriented parallel (anti-parallel) to the nucleon spin, and η is the fraction of the nucleon momentum carried by the gluon.

A prediction for the quantity $\Delta\Sigma$ can be derived in the hypothesis that the nucleon is composed only by three quarks flavours ($u(\bar{u})$, $d(\bar{d})$ and $s(\bar{s})$). Inserting in eq. 1.23 the expression 1.21 for $g_1(x)$ one gets

$$\Gamma_1^p = \frac{1}{2}\left(\frac{4}{9}\Delta u + \frac{1}{9}\Delta d + \frac{1}{9}\Delta s\right), \tag{1.28}$$

and, from isospin invariance,

$$\Gamma_1^n = \frac{1}{2}\left(\frac{1}{9}\Delta u + \frac{4}{9}\Delta d + \frac{1}{9}\Delta s\right), \tag{1.29}$$

Additional informations on the Δq_i can be extracted from the neutron and hyperon β decays. Linear combinations of the Δq_i moments are related to the

weak axial-vector constants a_0, a_3 and a_8 by [2][3]

$$a_0 = \Delta u + \Delta d + \Delta s \equiv \Delta\Sigma \tag{1.30}$$

$$a_3 = \Delta u - \Delta d = \left|\frac{g_A}{g_V}\right| = F + D \tag{1.31}$$

$$a_8 = \Delta u + \Delta d - 2\Delta s = 3F - D, \tag{1.32}$$

where F and D are $SU(3)$ coupling constants. Then eqs. 1.28–1.29 can be rewritten as

$$\Gamma_1^{p(n)} = +(-)\frac{1}{12}a_3 + \frac{1}{36}a_8 + \frac{1}{9}a_0. \tag{1.33}$$

The equations 1.33 are the Ellis-Jaffe sum rules for the proton and the neutron.

Using the values of $F + D = 1.257 \pm 0.003$ and $F/D = 0.575 \pm 0.016$ derived from the neutron and hyperon β-decays, and with the hypothesis that the strange sea-quarks are unpolarized ($\Delta s = 0$, $a_0 = a_8$), one obtains $\Delta\Sigma = \Delta u + \Delta d \simeq 0.58$ [2]. The corresponding Ellis-Jaffe prediction for Γ_1^p is $\Gamma_1^p \simeq 0.19$.

1.2 EMC and the "proton spin crisis"

The Ellis-Jaffe sum rules can be verified by measuring the $g_1(x)$ distribution over a range of x as wide as possible, both with proton and neutron targets. The experimental value of Γ_1^p can also be used to derive, together with the a_3 and a_8 constants, the total quark contribution $\Delta\Sigma$ to the nucleon spin. The measurement has been performed by the EMC experiment at CERN (see Fig. 1.4), with a surprising result: the calculated value of Γ_1^p implied that $\Delta\Sigma = 0.12 \pm 0.16$ [6], i.e. the quark contribution to the proton spin is compatible with zero.

The EMC result, confirmed later by the SMC and E154 experiments, raised new possible descriptions for the structure of the nucleon within the framework of QCD. However, despite the theoretical efforts a clear explanation of the polarized DIS results is still missing. Various models have been proposed which either claim for a large gluon contribution to the nucleon spin, or introduce

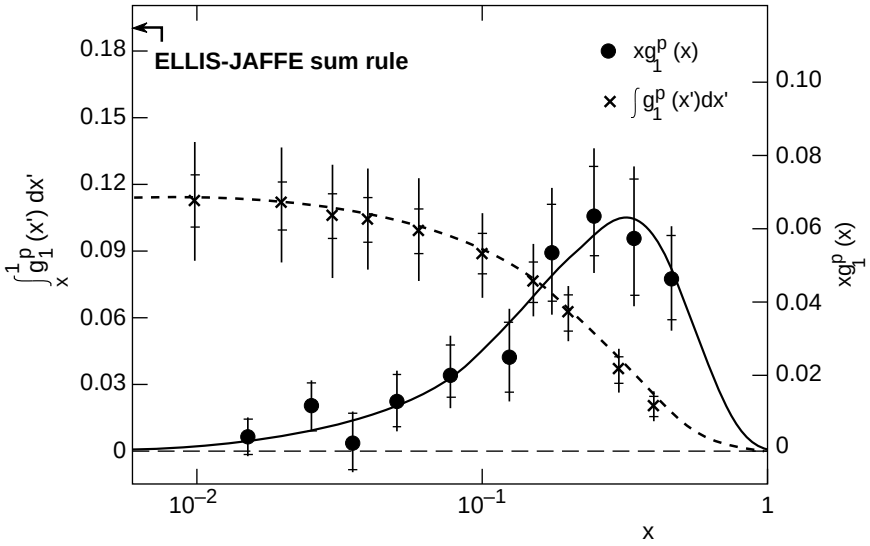

Figure 1.4: *The EMC result for the Ellis-Jaffe sum rule: solid line is the measured structure function $xg_1^p(x)$, dashed line is the integral $\int_x^1 g_1^p(x')\ dx'$. The measured $\Gamma_1^p = \int_0^1 g_1^p(x)\ dx$ is compared with the Ellis-Jaffe prediction. Curves are plotted as a function of x.*

a seizable negative strange sea-quark polarization which effectively "screens" the valence quark contribution. Angular momentum could contribute as well to the nucleon spin, but it is not clear if a direct measurement of the angular momentum contribution is possible [9]. In order to discriminate between the existing models, it is necessary to perform semi-inclusive polarized DIS measurements, which allow to independently measure the quark and gluon polarized distribution functions and verify the model predictions.

1.3 Gluon polarization $\Delta G/G$ and COMPASS

A possible solution of the "proton spin crisis" can be given by a large contribution of the gluon polarization. It is therefore mandatory to perform precise measurements of the polarized gluon distribution function $\Delta G(\eta)$.

The measurement of $\Delta G(\eta)/G(\eta)$ distribution, where $G(\eta)$ represents the unpolarized gluon distribution function, is one of the main programs of the

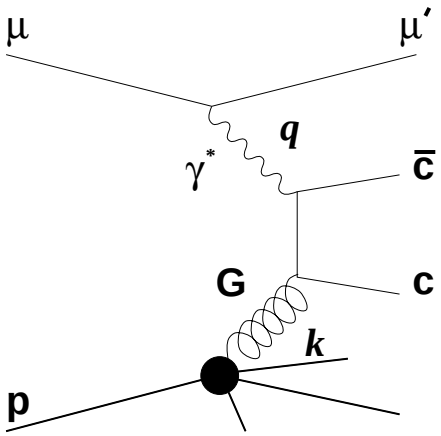

Figure 1.5: *The photon-gluon fusion diagram. The incoming muon emits a virtual photon which is absorbed by a gluon in the nucleon, through an intermediate state, that fragments into charmed hadrons in the final state.*

COMPASS experiment. Among the various suggestions to measure the gluon distribution function, the most promising for COMPASS is the longitudinal spin asymmetry of open charm leptoproduction. In the dominant process for this production, charm quarks are produced via the photon-gluon fusion (PGF) diagram shown in Fig. 1.5. The $\Delta G(\eta)$ distribution is extracted from the measured asymmetry $A_{\mu N}^{c\bar{c}}$ for charm muon-production, with parallel and anti-parallel longitudinal spin orientations of the incoming muon and of the target nucleon. The experimentally measured asymmetry for charm production

$$A^{exp} = \frac{N_{c\bar{c}}^{\uparrow\downarrow} - N_{c\bar{c}}^{\uparrow\uparrow}}{N_{c\bar{c}}^{\uparrow\downarrow} + N_{c\bar{c}}^{\uparrow\uparrow}} \propto A_{\gamma N}^{c\bar{c}} = f\left(\frac{\Delta G(\eta)}{G(\eta)}\right), \tag{1.34}$$

where $N_{c\bar{c}}^{\uparrow\downarrow}$ ($N_{c\bar{c}}^{\uparrow\uparrow}$) is the number of charm events for anti-parallel (parallel) orientations of the spin of the incoming lepton and of the target nucleon, is proportional to the virtual photon asymmetry $A_{\gamma N}^{c\bar{c}}$. This quantity is in turn function of the ratio $\Delta G(\eta)/G(\eta)$.

The charm quarks hadronize into D^0 mesons approximately 60% of the time, and 20% in $D^{*\,+}$. The COMPASS apparatus has been specifically designed to detect, from their $D^0 \to K^-\pi^+$ decay, D^0 mesons produced in the hadronization of the $c\bar{c}$ pair. The $D^{*\,+} \to D^0\pi^+ \to (K^-\pi^+)\,\pi^+$ decay can be tagged by

requiring an additional soft pion in the final state. A specific trigger has also been prepared to allow the reconstruction of the DIS kinematics in the quasi-real photon absorption region ($Q^2 \approx 0$), where the cross-section for the photon-gluon fusion process is expected to be maximal.

1.4 Polarization of strange sea quarks of the nucleon

The content of strange quarks in the nucleon is currently of great theoretical and experimental interest. This because the strange sea quarks could be negatively polarized with respect to the parent nucleon, and this fact could explain the small value of $\Delta\Sigma = \Delta u + \Delta d + \Delta s$ measured by the experiments.

A model has been proposed in [10] which is based on two major observations. First of all, the fact that the the masses of pions and kaons are small at the typical hadronic scale can be attributed to the existence of a strong attraction between quarks and anti-quarks in the pseudoscalar channel $J^{PC} = 0^{-+}$. Therefore all the diquark pairs $q_i\bar{q}_j$ inside the nucleon are expected to have these quantum numbers, which imply spin singlet states. The second point is that in the vacuum the quantum numbers must be $J^{PC} = 0^{++}$, therefore only the $^3P_0$ state is allowed. Between the diquark pairs of the vacuum the strange content ($s\bar{s}$) is expected to have a density of the same order of that of light quarks.

Therefore a possible contribution to the proton spin can be attributed to an interaction of the valence quarks of the proton wave function with the strange anti-quarks of the vacuum, through an interaction that should select a spin singlet state. Therefore the spin of the strange anti-quarks must be opposite oriented to that of the valence quark. The requirement that the $s\bar{s}$ pairs of the vacuum are in a triplet state supports than that also the s quark is with a spin opposite oriented to that of the valence quark, and hence to that of the nucleon.

Therefore the contribution to the nucleon spin of the strange content (Δs) is expected to be negative.

1.4.1 Λ polarization in deep inelastic lepton scattering

The Λ hyperons produced in polarized deep inelastic lepton scattering are of special interest for the measurement of the strange sea-quarks properties. In the simple parton model representation of hadrons, the Λ hyperons contain a ud pair in a singlet state, and an s quark carrying all the spin of the hyperon. The Λ hyperons undergo weak decay in $p\pi^-$ in 64% of the cases. Due to the parity-violating properties of weak interactions, the distribution of the decay products in the Λ rest frame is not isotropic, but the proton is emitted preferentially in the direction of the Λ spin vector. Thus if the produced Λ have a net polarization P_Λ along a certain direction $\hat{n}$, the decay proton distribution is given by

$$W(\theta_p^*) = \frac{1}{4\pi}\left[1 + \alpha P_\Lambda \cos(\theta_p^*)\right], \tag{1.35}$$

where θ_p^* is the polar angle between the proton direction and the polarization axis $\hat{n}$, measured in the Λ center of mass frame.

When discussing the production of Λ hyperons in polarized lepton-nucleon DIS, it is fundamental to distinguish between the *target fragmentation region* and the *current fragmentation region*, according to the sign of the x-Feynman (x_F) kinematical variable, defined as the ratio between the measured and the maximum allowed Λ longitudinal momenta, in the $\gamma^* N$ center of mass frame:

$$x_F = \frac{p_L^\Lambda}{p_{L_{MAX}}^\Lambda} = \frac{2p_L^\Lambda}{\sqrt{s}}. \tag{1.36}$$

1.4.2 Target fragmentation region

The polarization of the strange sea quarks inside the nucleon can be measured by looking at the polarization of Λs produced at $x_F < 0$ (target fragmentation region) in the deep-inelastic scattering of longitudinally polarized muon beams on longitudinally polarized nucleons. The argument is based on the fact that the cross-section for the electromagnetic interaction of longitudinally polarized leptons and nucleons depends on the longitudinal polarization states of the quarks in the nucleon[12]. The exchanged virtual photon is preferentially absorbed by a quark with the spin oriented anti-parallel to the spin of the beam muon. In this

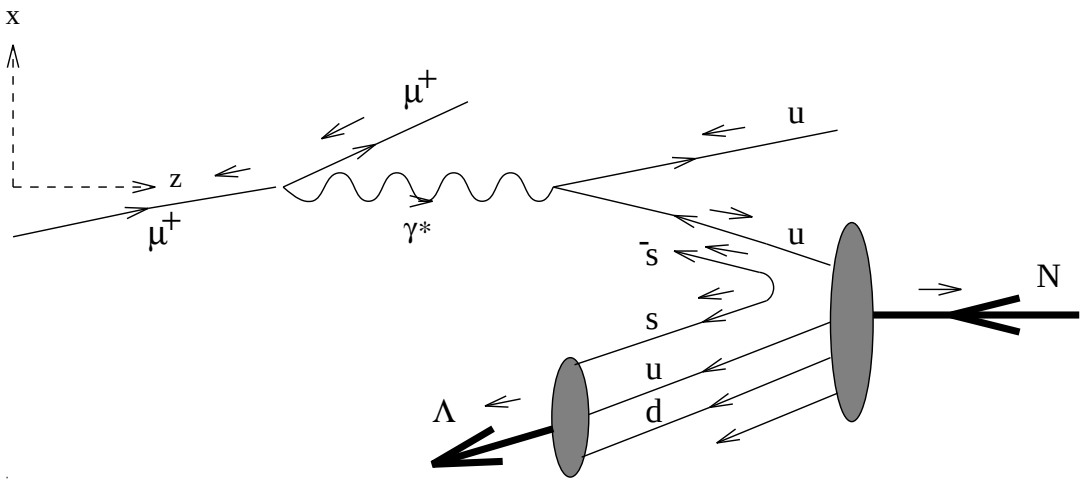

Figure 1.6: *Expected Λ polarization in deep-inelastic μN scattering on a valence u quark. The exchanged virtual photon preferentially selects a quark with the spin aligned parallel to the proton spin. The opposite orientation of the $s\bar{s}$ pair is reflected in the polarization of the Λ produced in the target fragmentation region.*

case the Λ hyperons produced in the target fragmentation region are expected to originate from a spin-triplet $s\bar{s}$ pair with their spins oriented anti-parallel to the spin of the struck quark. If s-quark polarization is transferred to the final state Λ, the observation of the distribution of the decay proton with respect to the direction of the virtual photon gives information on the polarization of the strange sea-quarks.

1.5 The transverse spin of the nucleon

The leading-order description of the internal structure of the nucleon requires, for each quark and anti-quark flavor, three different distribution functions. Two of them are the $q(x)$ and $\Delta q_i(x) = q_i^+(x) - q_i^-(x)$ distributions which have been already introduced when discussing the unpolarized DIS and the polarized DIS with longitudinally polarized targets respectively. The third one is introduced to describe the distribution of quarks in a transversely polarized nucleon, and

is denoted as $\Delta_T q_i(x) = q_i^{\uparrow}(x) - q_i^{\downarrow}(x)$. Here $q_i^{\uparrow}(x)$ ($q_i^{\downarrow}(x)$) represents the probability of finding a quark at a certain x and with its spin oriented parallel (anti-parallel) to the **transverse** spin of the nucleon. A similar definition applies for anti-quarks. We also introduce a new structure function, denoted with $h_1(x)$ and defined as:

$$h_1(x) = \sum_i \left[(q_i^{\uparrow} + \bar{q}_i^{\uparrow}) - (q_i^{\downarrow} + \bar{q}_i^{\downarrow}) \right], \tag{1.37}$$

which is the equivalent of $g_1(x)$ for a transversely polarized target.

Transversity is a pure relativistic effect: when the nucleon is at rest, there is no reason why the quark spin distributions should differ if the nucleon spin is rotated of 90 degrees. However the distribution functions are usually defined in the so-called infinite momentum frame, in which the transverse momentum of the quarks can be neglected. In this frame the longitudinal spin configuration is not equivalent to the transverse spin anymore, since Lorentz boosts and rotations do not commute. The difference between helicity and transversity distributions therefore derives from relativistic effects which can give important informations on the internal structure of nucleons.

The measurement of the transversity distribution functions is experimentally more difficult than the elicity-dependent distributions $\Delta q_i(x)$. The transverse spin of quarks cannot be probed in inclusive DIS with longitudinally polarized leptons. An intuitive argument to explain this fact is the following. The transverse spin states can be expressed in the helicity basis as:

$$|\uparrow> = \frac{1}{2}\left[|+> + i|->\right], \qquad |\downarrow> = \frac{1}{2}\left[|+> - i|->\right]. \tag{1.38}$$

Therefore a transversely polarized quark can be found in both + and − helicity states with equal probability. For this reason, the elementary lepton-quark interaction, and therefore the inclusive DIS process, does not depend on the transverse spin state of the struck quark.

A more rigorous argument is based on the fact that the transversity distributions are chiral-odd objects, involving an helicity-flip of the struck quark. The elementary photon-quark scattering conserves chirality, and cannot reveal

a chiral-odd object like $h_1(x)$. The measurement of $h_1(x)$ is possible only if combined with another chiral-odd distribution. In polarized SIDIS this distribution is a chiral-odd quark fragmentation function $D_q^H(z)$, describing the probability for a quark q to fragment into a certain hadron H carrying a fraction z of the quark momentum. However, semi-inclusive measurements, involving the detection of a particular hadron H in addition to the scattered lepton, are experimentally more difficult than inclusive ones. In the next section the Λ production case will be considered.

1.6 Λ production with a transversely polarized target

The polarization of Λ hyperons produced in the scattering of an unpolarized lepton off a transversely polarized nucleon can be expressed as[14]:

$$P_{0\uparrow}^H = \hat{D}_{NN}(y)\frac{\sum_i e_{q_i}^2\ \Delta_T q_i(x)\ \Delta_T D_{q_i}^H(z)}{\sum_i e_{q_i}^2\ q_i(x)\ D_{q_i}^H(z)}. \tag{1.39}$$

The factor $\hat{D}_{NN}(y)$ takes into account the spin dependence of the elementary lepton-quark interaction:

$$\hat{D}_{NN}(y) = \frac{d\hat{\sigma}^{lq^\uparrow \to lq^\uparrow} - d\hat{\sigma}^{lq^\uparrow \to lq^\downarrow}}{d\hat{\sigma}^{lq^\uparrow \to lq^\uparrow} + d\hat{\sigma}^{lq^\uparrow \to lq^\downarrow}} = \frac{2(1-y)}{1+(1-y)^2}. \tag{1.40}$$

In eq. 1.39 we have introduced the transversity fragmentation functions $\Delta_T D_{q_i}^H(z)$ defined as

$$\Delta_T D_{q_i}^H(z) = D_{q_i^\uparrow}^{H^\uparrow}(z) - D_{q_i^\uparrow}^{H^\downarrow}(z), \tag{1.41}$$

where $D_{q_i^\uparrow}^{H^{\uparrow(\downarrow)}}(z)$, which represent the probability for a quark q_i of fragmenting into a Λ hyperon carrying a fraction z of the quark momentum and with the spin correlated (anti-correlated) with the transverse spin of the quark.

In the polarized SIDIS, the quantities $\Delta_T q(x)$ can only be measured together with the transversity fragmentation functions $\Delta_T D_q^H(z)$. For this reason, additional informations on the $\Delta_T D_q^H(z)$ functions are needed in order to isolate

the $\Delta_T q(x)$ distribution functions. Such information can be extracted from the data coming from the $pp^{\uparrow} \rightarrow \Lambda^{\uparrow} X$ reaction[18], and the combined measurements of $pp^{\uparrow}$ and μN interactions can lead to the $\Delta_T q(x)$ measurement.

Chapter 2

The experimental apparatus

The COMPASS apparatus is a double magnetic spectrometer with complementary kinematical ranges. The two spectrometers have a similar structure and are based on dipole magnets called SM1 and SM2 respectively. Each spectrometer is equipped with several tracking devices with different spatial and timing resolutions, and one RICH (Ring Image CHerenkov) detector for particle identification.

Tracking of charged particles is performed by means of a large variety of detectors. Beam particles are tracked using scintillating fiber and silicon detectors, which provide good spatial and time resolutions and are suitable for high particle fluxes. Outside the beam spot region gas multiplication detectors are used. Particles emitted with small angles are detected using Micromegas detectors in the region between the target and SM1, and Gas Electron Multiplier detectors in the rest of the apparatus. This kind of detectors provide an active area of $\sim 30 \times 30$ cm^2 and a spatial resolution of ~ 70 μm, and are complemented in the central region by scintillating fibers. Large area tracking is performed using drift chambers, straw detectors, MWPC chambers and plastic Iarocci tube detectors. Drift chambers and straws provide the tracking of large angle particles before and behind the first spectrometer magnet SM1, while MWPCs represent the main tracking system of the second, small angle spectrometer. Two large area drift chambers, mounted in front of the second muon absorber, provide ad-

LAS		SAS	
SM1 aperture:	2.0×1.6 m^2	SM2 aperture:	2.0×1.0 m^2
SM1 field integral:	1 Tm	SM2 field integral:	4.4 Tm
Angular acceptance:	$\theta > 30$ mrad	Angular acceptance:	$\theta < 30$ mrad
Momentum range:	$p < 60$ GeV/c	Momentum range:	$p > 10$ GeV/c

Table 2.1: *Characteristics of the Large Angle Spectrometer (LAS) and of the Small Angle Spectrometer (SAS) of the COMPASS apparatus.*

ditional track points for muons scattered at large angles. Particle identification is performed using a Ring Image CHerenkov (RICH) detector located between SM1 and SM2. Muon identification is performed by means of two thick Fe hadron absorbers, called μF1 amd μF2. Tracking stations before and behind the absorbers allow to separate muons and charged hadrons, since the latters are stopped and do not produce signals in the detectors downstream of the absorbers. Tab. 2.1 summarizes the characteristics of the two spectrometers with respect to the allowed kinematical ranges and angular acceptances.

A typical event with Λ candidates in the final state is shown in Fig. 2.1; the scattered muon is tracked along the full apparatus and identified by the crossing of the second muon filter, while Λs are reconstructed from the "V^0-like" decay vertexes in the first spectrometer.

2.1 The M2 beamline

The muon beam used in COMPASS is a tertiary beam of positive muons produced in the M2 beamline at the CERN SPS. The available kinematic range goes from $\pm$60 to $\pm$190 GeV/c with fluxes up to $2 \cdot 10^8$ muons per SPS cycle. It is a pulsed beam with a burst length of ~ 4 s and a period of ~ 14 s, produced using a 450 Gev/C primary proton beam extracted from the SPS toward the North Experimental Area. A fraction of the proton beam is selected by two stages of septum magnets and interacts with the primary T6 target, a 500 mm

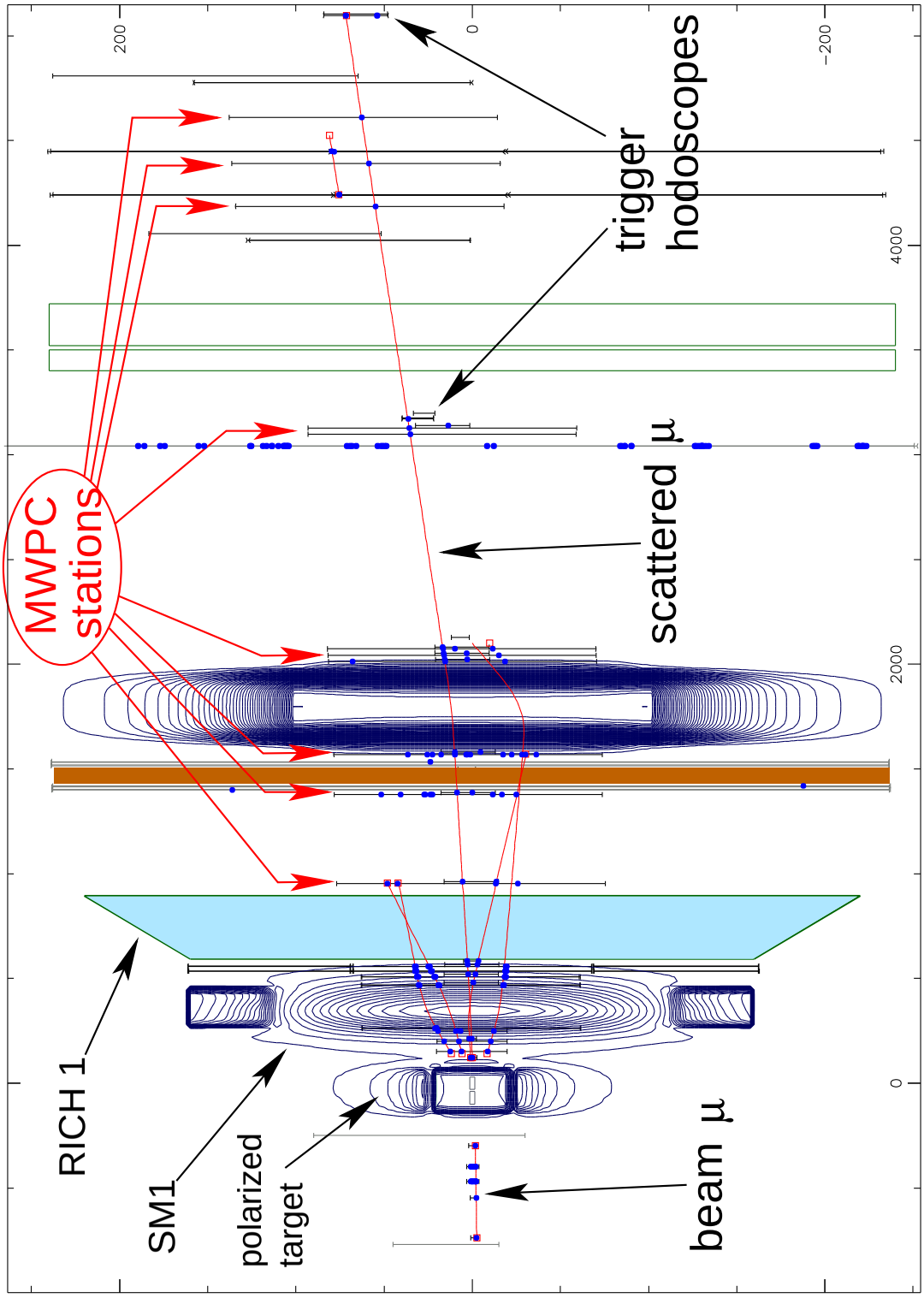

Figure 2.1: *DIS event with two h+/h- pairs.*

long and 3 mm thick beryllium plate. A secondary beam of positive or negative pions and kaons is derived from the target at zero production angle. The beam line can transport to the experiment either the primary π and k or the decayed μ or electron. In the latter case pions and kaons with a momentum spread of 5%, are selected by the first bending magnet and are transported through a 500 m long line of focusing and defocusing quadrupoles (see Fig. 2.2). In this section the tertiary muon beam is generated from pion and kaon decay and is transported toghether with the hadrons. At the end of the hadron section the beam is focused onto a 9.9 m long hadron absorber made of beryllium and located 700 m downstream of the production target. At this point the beam contains a muon fraction of about 6% for the standard pion energy of 208 GeV/c.

The absorber is located inside the bending magnet, which selects a muon momentum band of about 3%. In the following 300 m long muon section the beam is cleaned and focused onto the target of the experiment.

The muons produced from the parity violating pion decay $\pi \rightarrow \mu\nu$ (see Fig. 2.3) are naturally longitudinally polarized. The polarization depends on the decay angle in the pion rest frame with respect to its direction of flight in the laboratory rest frame. Positive forward (backward) muons are polarized anti parallel (parallel) to their momentum in the laboratory frame. Highest polarization is obtained for a muon to pion energy ratio close to unity. For the SMC experiment an operating point of $E_\mu/E_\pi = 0.91$ was chosen as a compromise of muon flux and polarization, leading to a measured polarization of -0.8. COMPASS uses a muon beam with the same characteristics. The polarization value measured in SMC is considered valid also for the COMPASS beam.

The COMPASS setup of the M2 muon beam provides a spot size at the polarized target of 7.8×7.8 mm and a divergence of 0.4×0.8 mrad, with a flux of $\sim 2 \cdot 10^8$ using the 500×3 mm beryllium target. Different target lengths can be selected in order to reduce the beam flux and allow data taking with spectrometer magnets off for alignment purposes.

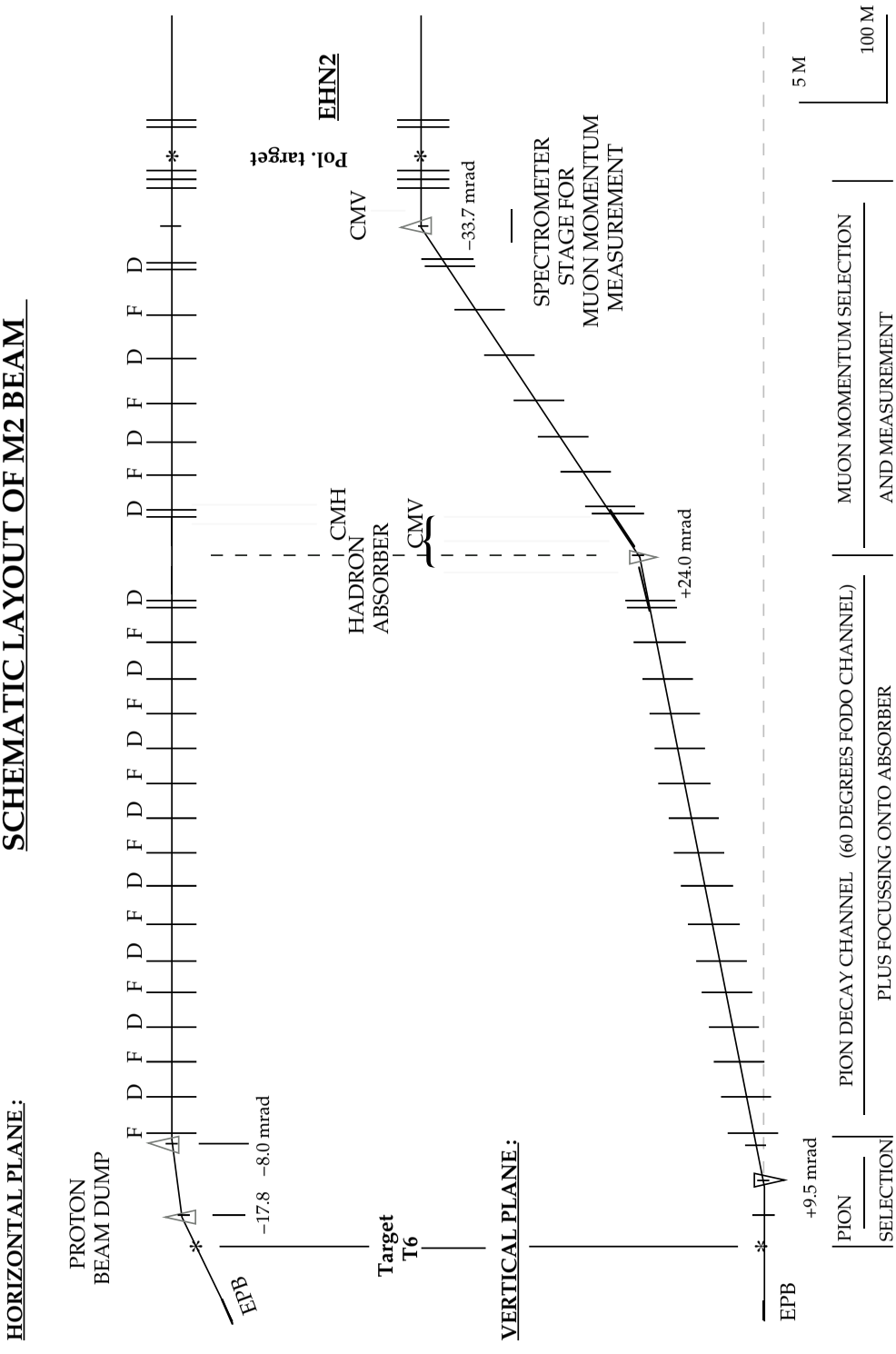

Figure 2.2: *Schematic view of the M2 beamline used in COMPASS.*

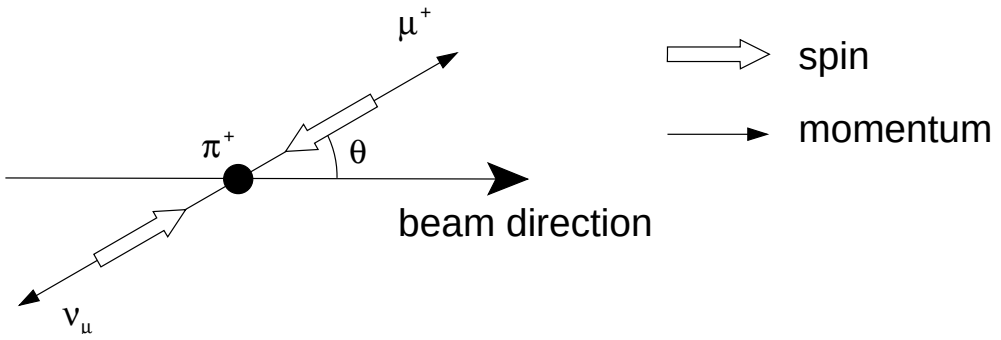

Figure 2.3: *Weak π^+ decay in the pion rest frame. Outgoing muon polarization is obtained by selecting θ angles close to zero.*

2.2 The polarized target

The COMPASS apparatus for the muon program uses a solid state polarized target in order to achieve high luminosities. The polarization of the target material is obtained using the technique of dynamic nuclear polarization which allows to greatly exceed the values given by the Curie law, which for spin-$\frac{1}{2}$ and spin-1 particles reads

$$P_{\frac{1}{2}} = \frac{N_{\frac{1}{2}} - N_{-\frac{1}{2}}}{N_{\frac{1}{2}} + N_{-\frac{1}{2}}} = \tanh\left(\frac{\hbar\omega}{2kT}\right) \tag{2.1}$$

and

$$P_1 = \frac{N_1 - N_{-1}}{N_1 + N_0 + N_{-1}} = \frac{4\tanh\left(\frac{\hbar\omega}{2kT}\right)}{3 + \tanh^2\left(\frac{\hbar\omega}{2kT}\right)}. \tag{2.2}$$

Here $\omega = \mu B/\hbar$ is the Larmor frequency, μ the magnetic moment of the particle, k the Boltzmann constant and N_m the population of the magnetic sublevel m. The formula 2.1 gives for the electron a polarization value of 0.998 for a typical field of $B = 2.5$ T and a thermal equilibrium temperature of $T = 2.5$ K, while at the same conditions the result for proton and deuteron is 0.0051 and 0.0011 respectively.

The dynamic nuclear polarization technique allows to transfer part of the almost complete electron polarization of the electrons to the nucleons using

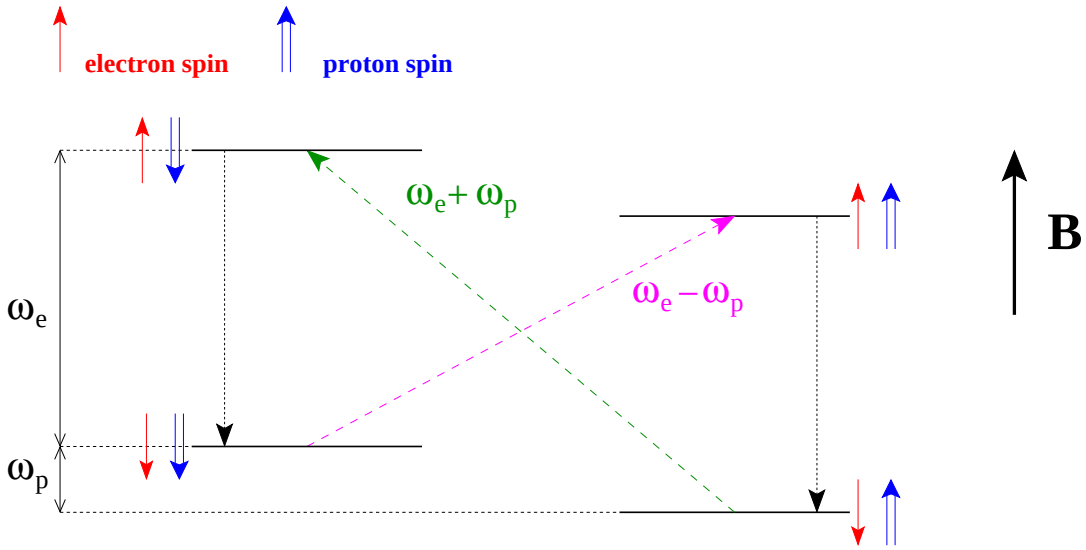

Figure 2.4: *Energy levels of an electron-proton pair in a strong magnetic field, B. The NMR-induced transitions exploited by the DNP technique are also shown.*

microwave irradiation. At the temperature of 0.5 K basically only the two lower magnetic sublevel are populated, with the spin of the electron aligned anti-parallel to the direction of the magnetic field (electron's magnetic moment parallel to the field) and the spin of the nucleons either parallel or anti-parallel to the electron's spin (see Fig. 2.4). The transitions $|\downarrow\Uparrow> \rightarrow |\uparrow\Downarrow>$ and $|\uparrow\Downarrow> \rightarrow |\downarrow\Uparrow>$ can be induced by microwaves of frequency $\omega_e+\omega_p$ and $\omega_e-\omega_p$ respectively. Since the relaxation time of the electron is of the order of 10^{-3} s while the relaxation time of the proton is 10^6 times bigger the microwave irradiation results in a net positive (negative) polarization of the protons for frequencies equal to $\omega_e + \omega_p$ $(\omega_e - \omega_p)$.

Target cell polarization direction can be reversed applying a varying solenoidal and dipolar magnetic fields. The rotation procedure takes around 30 minutes and implies a minimal loss in the polarization of the target material. The systematic reversal, performed every 8 hours, allows to minimize the influence of the apparatus acceptance on asymmetry measurements, when data from two different target cells are compared.

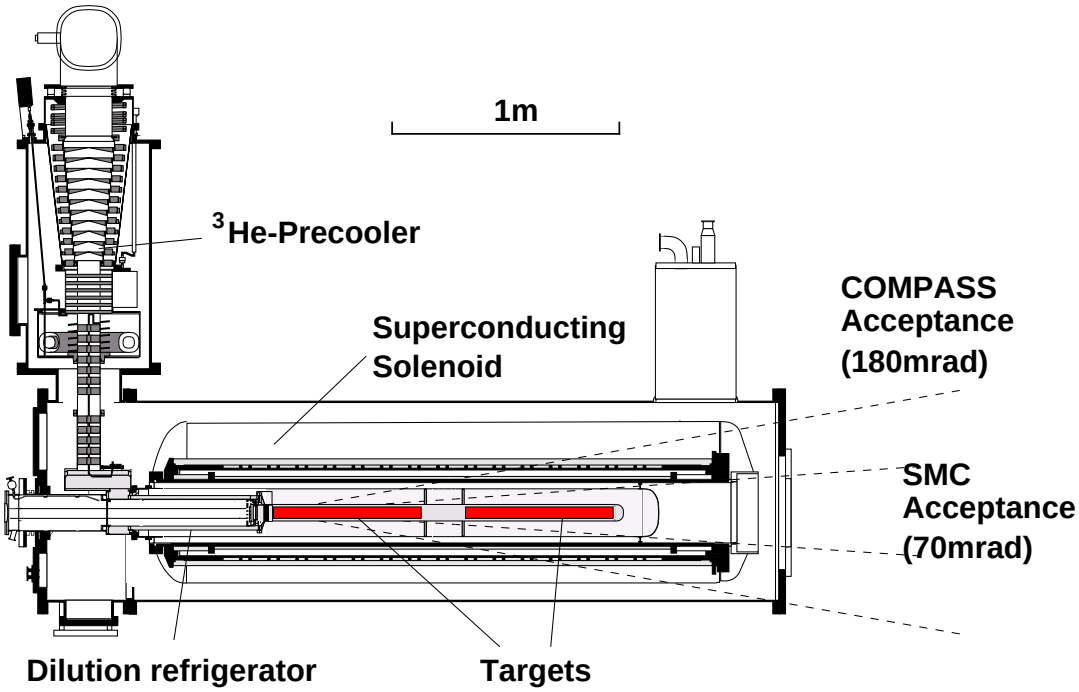

Figure 2.5: *Schematic view of the polarized target used in COMPASS. The actual acceptance is limited to 70 mrad.*

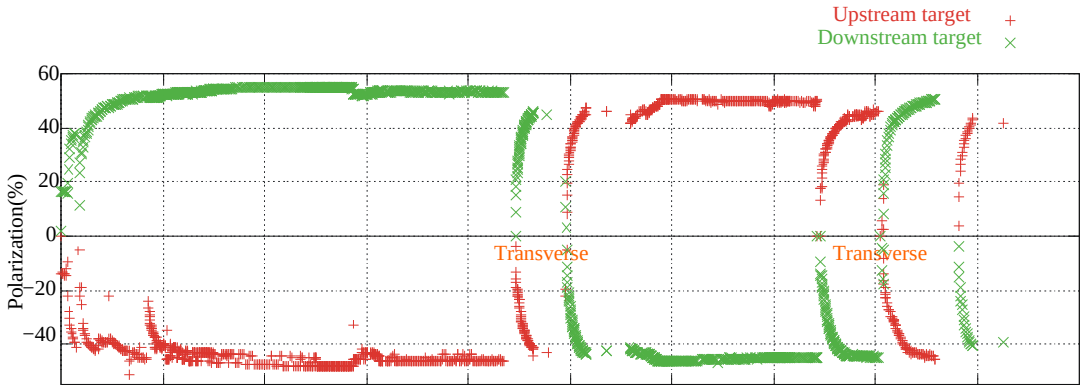

Figure 2.6: *Measured upstream and downstream target cell polarizations during 2002 data taking period.*

If rotation is stopped halfway and a dipolar magnetic field of $\sim$ 0.5 Tesla is kept, the target spin orientation is freezed in transverse configuration, with a time constant of several hundred hours. This configuration is used for the

measurement of the trasnversity distribution function discussed in the previous chapter. The polarization cannot be measured in the trasnverse target configuration.

The measured value of the target cell polarization during the 2002 data taking period is shown in Fig. 2.6.

2.3 Tracking system

2.3.0.1 Beam definition

The momentum of each incoming muon is measured at the Beam Momentum Station (BMS) consisting of four scintillating fiber planes and the last dipole magnet bending the muon beam vertically into the experimental hall (see Fig. 2.2). The scintillator planes form two telescopes upstream and downstream of the magnet and allow the measurement of the muon momentum. Only tracks with at least three fired BMS planes are reconstructed. Time correlation between BMS and beam hodoscopes is used to select good beam muon track candidates in the BMS. Fig. 2.7 shows the reconstructed beam momentum when 4 fired BMS planes are required.

2.3.0.2 Muon trigger

The COMPASS experiment is equipped with a multi-trigger acquisition system, which allows to perform several measurements at the same time. Each event is tagged with the kind of trigger which activated the front-end equipments, allowing fast offline selection of different kinematic regions of the DIS process.

The trigger is built starting from the signal of several hodoscopes, made of scintillator plates read out via photomultipliers. The hodoscopes are used to detect the scattered muons at various angles, and are grouped according to the angular regions they cover. Depending on their scattered muon acceptance, they will correspond to different Q^2 and ν regions, where ν is the energy of the exchanged virtual photon. The available triggers, with their Q^2 acceptance, are:

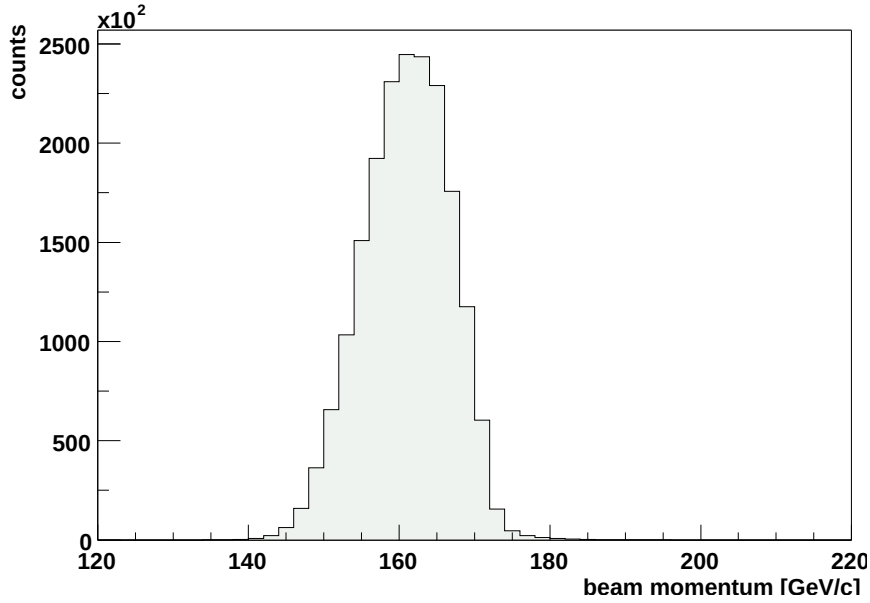

Figure 2.7: *Muon beam momentum measured with the BMS system. The plot is obtained by requiring 4 fired BMS planes. Nominal beam momentum is* ~ 160 *Gev/c.*

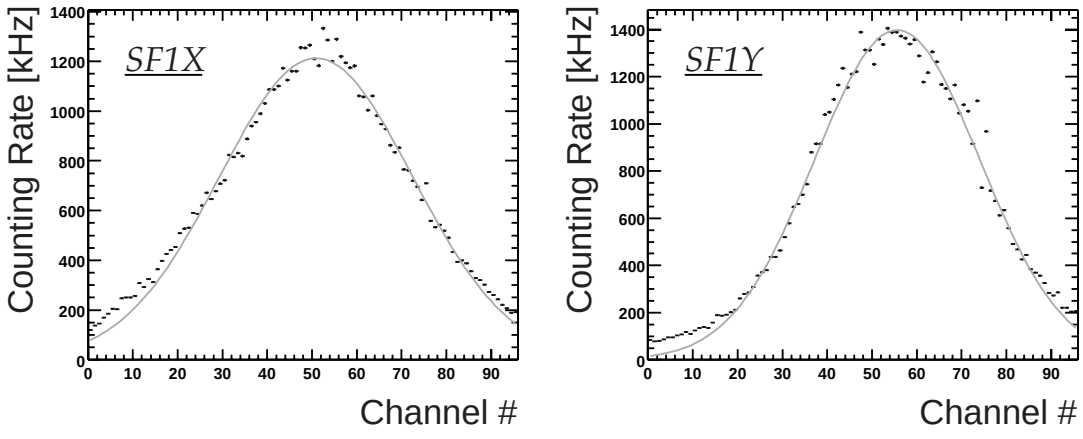

Figure 2.8: *Beam profiles in X and Y directions as recorded by the first SciFi station SF1.*

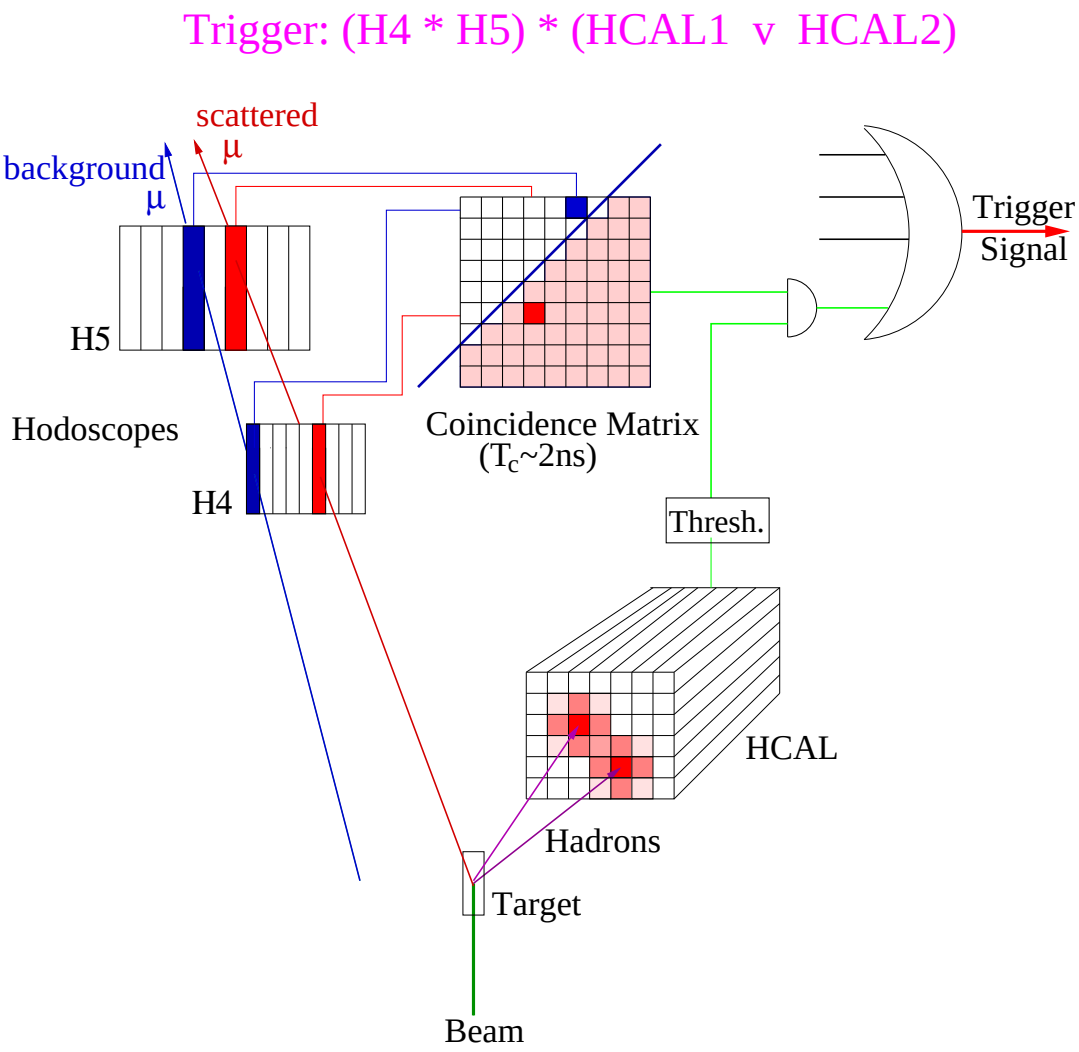

Figure 2.9: *Schematic view of the trigger logic used in COMPASS. A coincidence matrix allows to separate scattered and background muons.*

- Inner (Inclusive) Trigger (IT), $Q^2 < 1$ GeV^2, low ν
- Ladder Trigger (LT), $Q^2 < 3$ GeV^2, high ν
- Middle Trigger (MT), $0.1 < Q^2 < 10$ GeV^2
- Outer Trigger (OT), $Q^2 > 0.3$ GeV^2

A beam trigger signal also exists, defined by the logical OR of all the channels

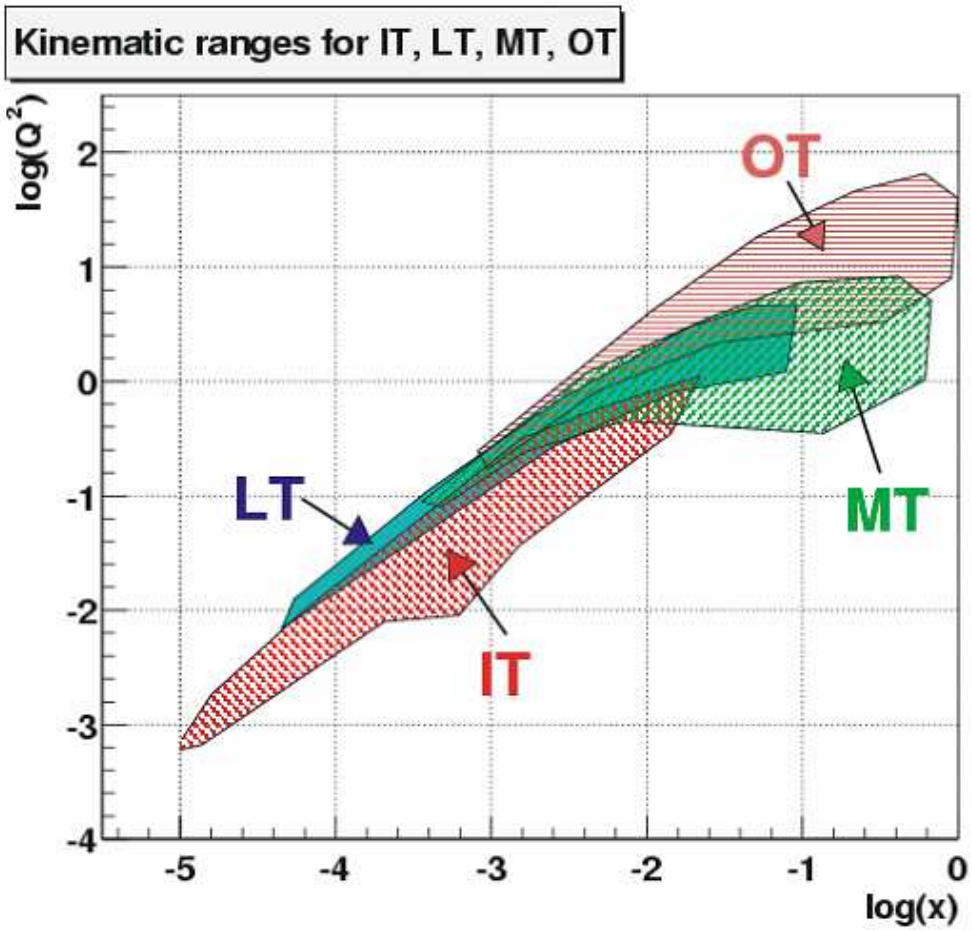

Figure 2.10: *Q^2 and x_{Bj} acceptances of the various trigger types.*

of the scintillating fiber station placed in front of the polarized target. A veto system, composed of scintillator hodoscopes placed upstream the target and around the beam spot, is used to identify and reject halo muons.

The Inner and Ladder systems are used to trigger on quasireal photoabsorption events, among which photon-gluon fusion events are specially interesting for the ΔG measurement. The Middle and Outer systems are on the other hand used to trigger on deep-inelastic events with $Q^2 > 1$ GeV^2. The regions of the (Q^2, x_{Bj}) plane covered by the various trigger types are shown in Fig. 2.10.

Each trigger system is composed of two scintillating detector stations placed at different distances from the target center. The digitized signal of the various scintillator plates in the two stations is fed to a coincidence matrix with adjustable delays for each row and column input, as schematically shown in Fig. 2.9. The hit correlation between the two stations allows to discriminate between muons scattered from the target and halo muons, with an efficiency determined by the cut applied on the coincidence matrix. The wider is the cut, the higher is the efficiency, but the purity, i.e. the percentage of "good" muons among the accepted events, decreases. A coincidence matrix with optimal cuts is defined for each type of trigger. The outputs of the various coincidence matrices are then prescaled to have an approximate balance among all the available triggers and obtain an overall trigger frequency of ~ 10 kHz.

The Inner and Ladder triggers are used for the detection of open charm production events, and require an additional information from the hadronic calorimeters, in order to reject radiative and μe scattering events as well as low energy halo tracks.

2.3.0.3 Calorimetry

The complete COMPASS setup is equipped with electromagnetic and hadronic calorimetry in both spectrometers. Table 2.2 summarizes the required calorimetry performances. In the 2002 setup only hadronic calorimeters have been fully installed and instrumented, while ECAL2 is partially installed with an old GAMS setup, and ECAL1 is still missing.

LAS

Hadronic (HCAL1)	$\frac{\sigma}{E} = \frac{80\%}{\sqrt{E}} \oplus 8\%$
Electromagnetic (ECAL1)	$\frac{\sigma}{E} = \frac{2.8\%}{\sqrt{E}} \oplus 0.5\%$

SAS

Hadronic (HCAL2)	$\frac{\sigma}{E} = \frac{60\%}{\sqrt{E}} \oplus 6\%$
Electromagnetic (ECAL2)	$\frac{\sigma}{E} = \frac{5.5\%}{\sqrt{E}} \oplus 1.5\%$

Table 2.2: *Required characteristics for the COMPASS calorimeters.*

2.3.0.4 Event reconstruction and particle identification

In the following the main characteristics of the various tracking detectors used in COMPASS are presented.

- **Scintillating Fibers**

  Beam tracks are detected using scintillating fiber detectors with a size of 50×50 mm, schematically shown in Fig. 2.11. They provide good spatial and time resolution with a very fast response which makes them also suitable as trigger detectors. Four stations are located around the polarized target, two upstream and two downstream. Time resolution of SciFi detectors can be measured by looking at the time difference of hits in two correlated planes, as SF1X&SF2X or SF1Y&SF2Y. The result is shown in Fig. 2.11-bottom for two different beam intensities and gives a measured time resolution of ~ 1.5 ns.

- **Silicon Detectors**

  The tracking system upstream the polarized target comprises two stations of Silicon detectors with four measured coordinates each. Silicon detectors provide a better spatial resolution if compared to scintillating fibers and

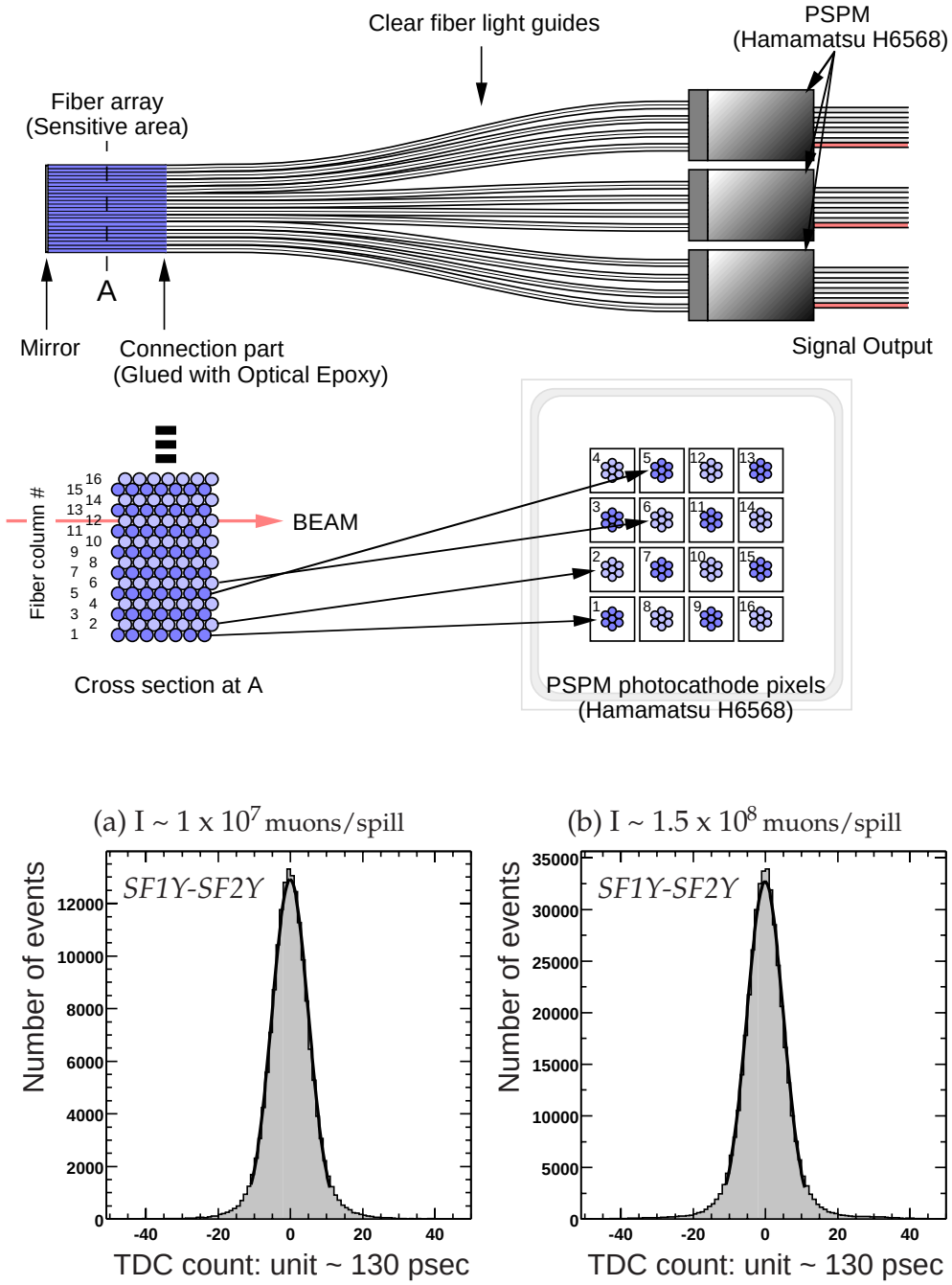

Figure 2.11: *SciFi detectors design. Upper figure shows the schematic view of one SciFi plane; each channel is made of seven scintillating fibers read out by the same photomultiplier, in order to achieve full efficiency. Bottom plots show the time resolution measured from time difference of hits belonging to two correlated planes, for (a) low intensity beam and (b) high intensity beam.*

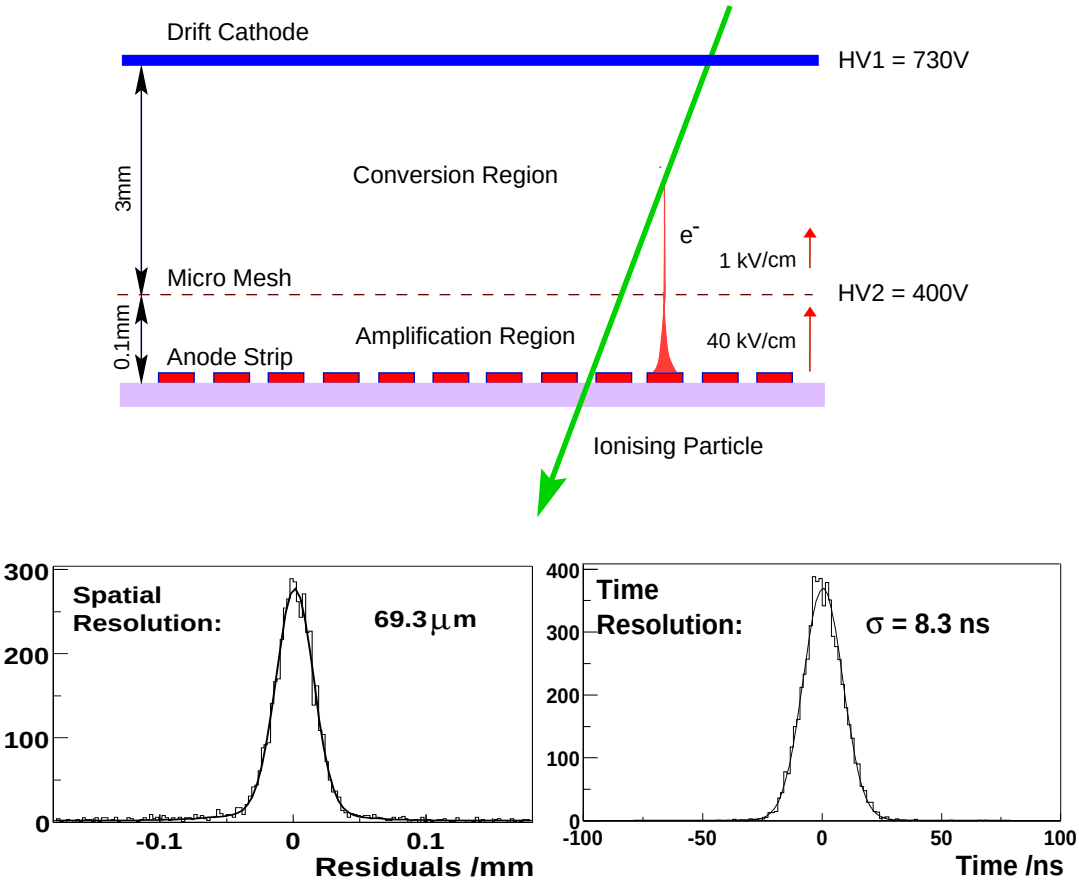

Figure 2.12: *Principle of operation and performances of Micromega gaseous detectors.*

are used to improve the tracking precision of beam muons. The SciFi-Silicons beam telescope provides an overall beam reconstruction efficiency of the order of 40%.

- **Micromegas**

  In this type of gaseous detectors the sensitive volume is divided into two regions by a Micromesh foil (see Fig. 2.12). The upper region in the picture (Conversion Region) occupies most of the sensitive volume and is characterized by a low electric field which make the electrons produced in it by ionization to drift toward the micromesh foil. This is a thin metallic grid which lets the electrons pass to the lower region, where the electric

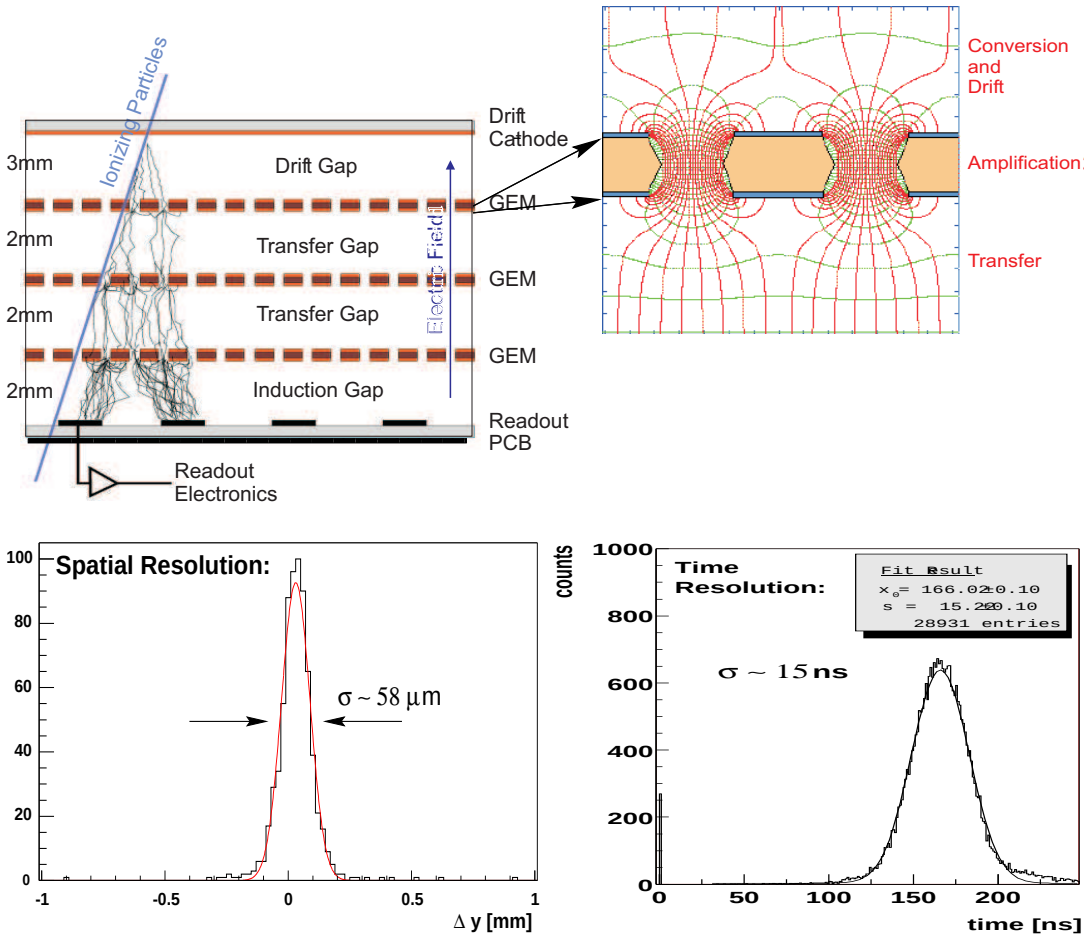

Figure 2.13: *Principle of operation and performances of GEM detectors.*

field is much more intense and multiplication occurs (Amplification Region). The electrons are collected by anode strips which are then read out and provide 1-D information on the localization of the charge avalanche.

- **GEM**

  GEM technology uses a different approach to produce charge multiplication. In this case high electric field are generated inside small holes created in a thin insulating mylar foil. The foil is coated on both sides with aluminum and a potential difference is applied. Electrons created by ionization in the conversion region above the first GEM foil (see Fig. 2.13) drift toward it and some of them enter the holes. Here the electric field is

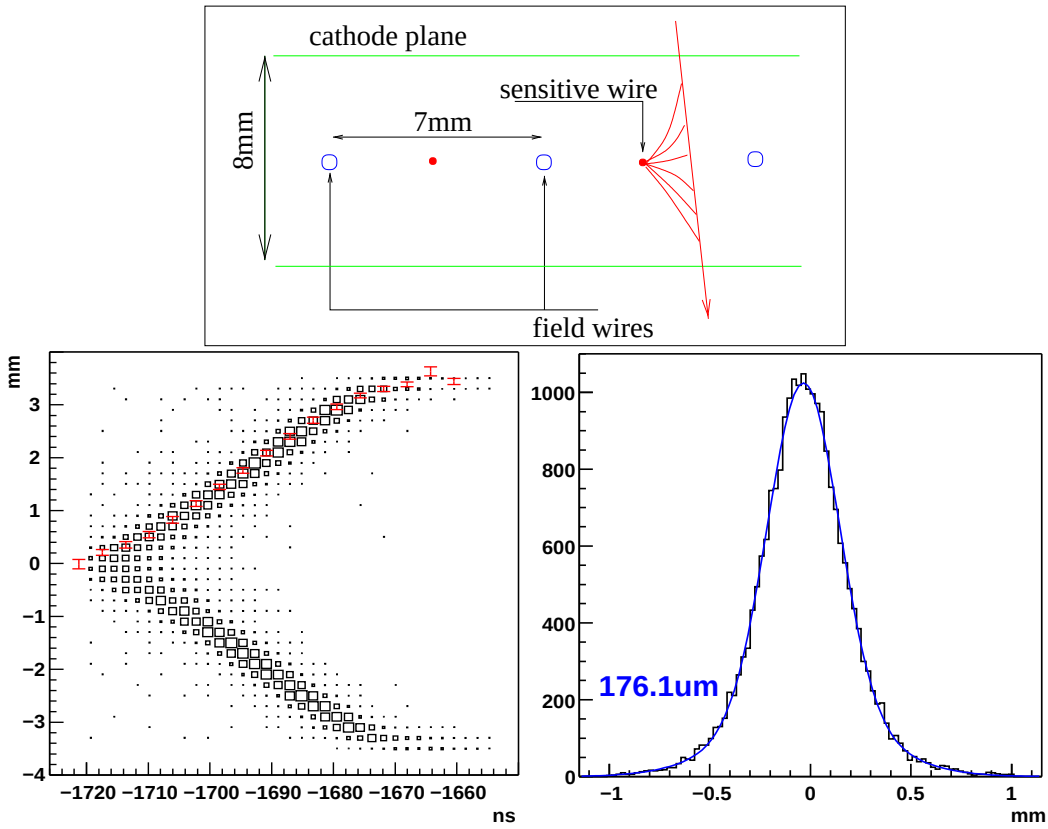

Figure 2.14: *Structure of the COMPASS drift chambers cell (above) and spatial resolution (below).*

high enough to produce charge avalanches and multiplication occurs. The newly produced electrons then start drifting in the transfer region below the GEM foil, while the ions are immediately collected by the bottom aluminized side of the GEM foil. This prevents space-charge effect to distort the electric field, except for the small gas volume inside the holes. One of the advantages of the GEM technology is that several foils can be stacked one over the other with a small transfer gap in between with a constant electric field. This allows to keep the amplification factor of each GEM foil low and to adjust the voltage drop at each foil in order to optimize both gain and detector stability. In COMPASS triple GEM technology is used, with gas gain of the order of 10^4.

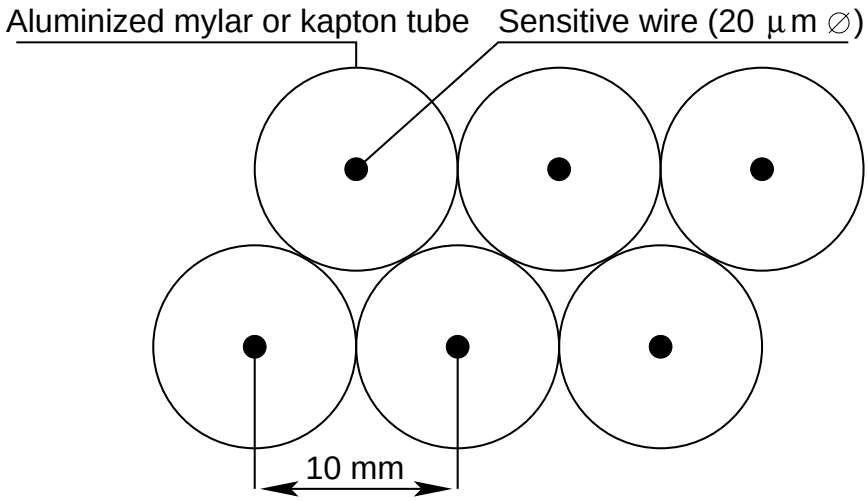

Figure 2.15: *Structure of a straw double layer with 10 mm diameter tubes.*

- **Drift Chambers and Straws**

  Large area tracking in the first spectrometer is performed using drift chambers and straw detectors. The COMPASS drift chambers are characterized by a 8 mm cathode/cathode gap and 7 mm cell size (see Fig. 2.14). The typical spatial resolution is ~ 180 μm, and the sensitive area size is 1.5×1.0 m^2.

  Straw detectors consist of thin drift tubes made of aluminized mylar or kapton with a sensitive wire stretched in the middle of the tube. Spacers placed inside the tube grant the accurate wire positioning along the whole tube length. The straw technology allows the construction of drift detectors with large surfaces without adding too much material on the particles flight path. COMPASS straw detectors have a size of 4×5 m^2.

- **W4/5 drift chambers**

  The tracking of scattered muons at large Q^2 is mainly based on the W4/5 drift detectors, located in front of the second hadron calorimeter. The W4/5 detectors are two large area drift chamber stations which have been previously used in the SMC experiment. The active area is 4×5 m^2, the drift cell is ~ 2 cm, and the spatial resolution is ~ 300 μm. Due to the

big size of the drift cell this chambers cannot sustain high particle fluxes, and the central region is deactivated by a circular dead zone of 50 cm of diameter, which is covered by MWPC stations.

- **MultiWire Proportional Chambers**
  MultiWire Proportional Chambers (MWPC) represent the backbone tracking system of the small angle spectrometer. They are characterized by an active area of 1780×1200 mm^2, wire spacing of 2 mm and spatial resolution of ~ 0.7 mm. In COMPASS three types of chambers are used: A-type chambers have three planes of sensitive wires, one vertical and two tilted by ± 10.14 degrees; A*-type is a modified A-type chamber with an additional horizontal plane; B-type have only two planes, one vertical and one either right or left tilted by 10.14 degrees. The dimensions of B-type chambers are reduced to 1780×800 mm^2. A circular area with diameter of ~ 20 cm around the beam crossing point is deactivated in order to prevent detector damage due to excessive particle flux. MWPC detectors are described in detail in chapter 3; all the main characteristics are summarized in Tab. 2.3.

- **Muon Wall 1**
  Muon identification in the first spectrometer is performed by means of the Muon Wall 1 detector. The detector consists of two large stations of Proportional Tubes, similar to the well-known plastic Iarocci tubes [references]. The stations are placed on both sides of a 0.6 m iron absorber which stops the hadrons (see Fig. 2.16). The detector is divided in submodules composed of a 600 μm thick aluminum profile with 8 cells, closed on the open side by a 150 μm stainless steel cover. A 50 μm gold plated anode wire is stretched in the center of each cell. The submodule is covered by a rectangular plastic profile which provides gas tightness.

- **Rich 1**
  Particle identification in the first spectrometer is based on a Ring Image

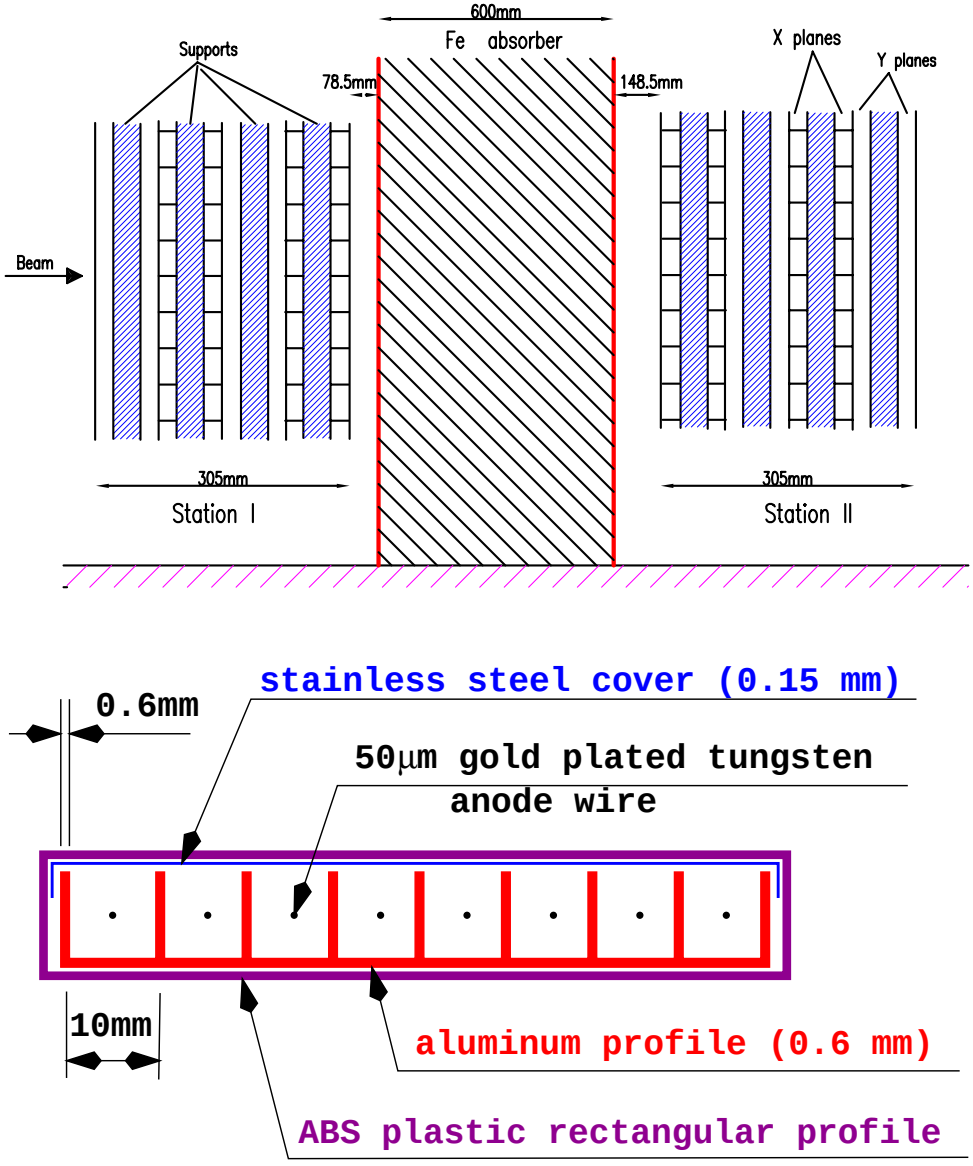

Figure 2.16: *Top figure: placement of the two stations of the MW1 detector, before and behind the first hadron absorber. Bottom figure: schematic view of one MW1 module.*

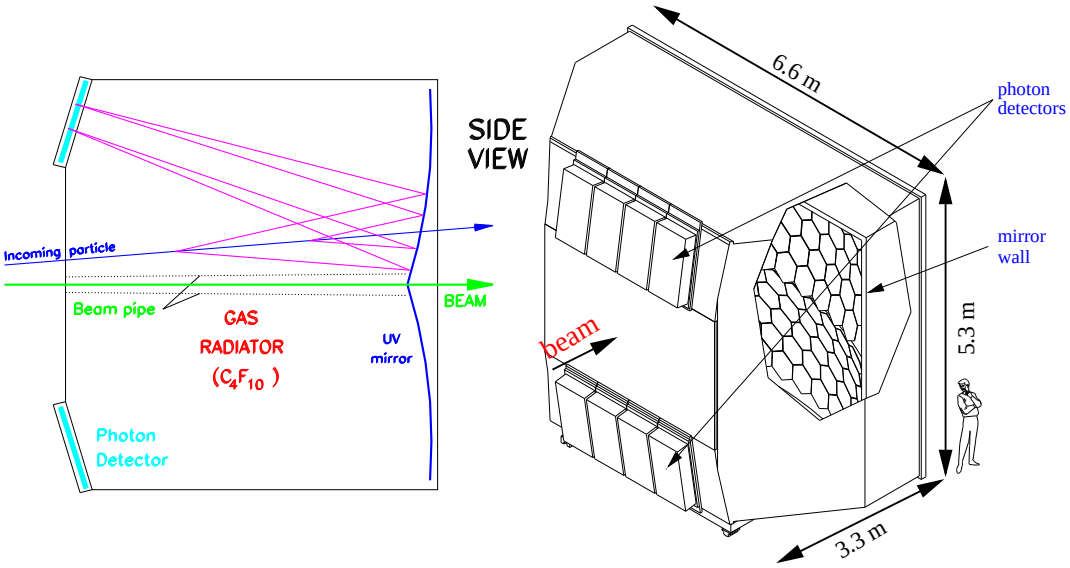

Figure 2.17: *Schematic view of Rich 1 detector and of the photon focusing optics.*

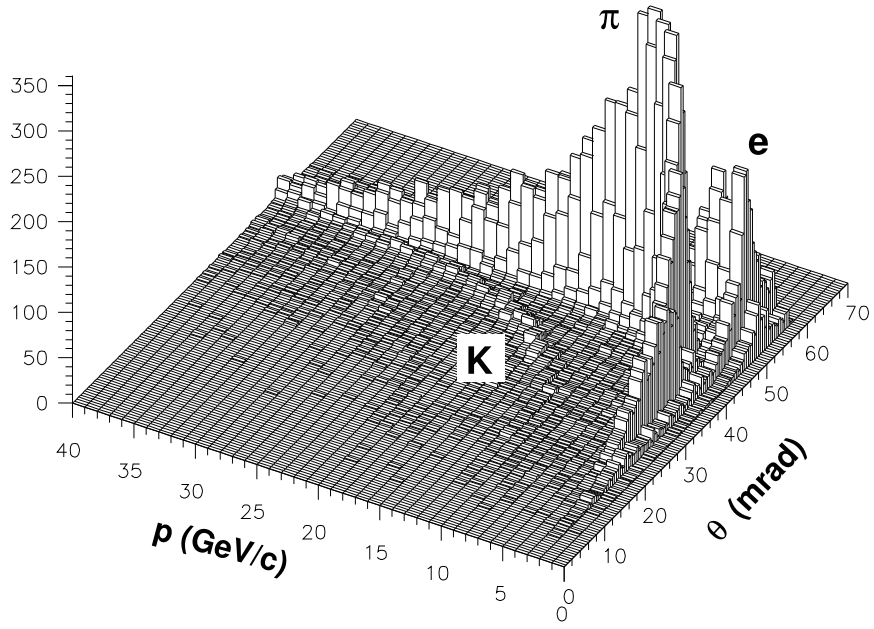

Figure 2.18: *Preliminary RICH results: particle momentum versus measured Cherenkov angle.*

	A-type	A*-type	B-type
available chambers:	7	1	6
external dimensions:	202x146 cm^2	202x146 cm^2	202x96 cm^2
active area:	178x120 cm^2	178x120 cm^2	178x80 cm^2
planes/chamber:	3	4	2
wire orientation(1):	1v, 2t	1v, 2t, 1h	1v, 1t
dead zone ⊘:	16 ÷ 20 mm	16 mm	22 mm
wire pitch:	2 mm		
anode/cathode gap:	8 mm		
wires/plane(1):	v,t: 752, h: 512		

(1): v = vertical, t = 10.14° w.r.t. v, h = horizontal

Table 2.3: *Characteristics of* Ω *MWPC.*

Cherenkov detector (RICH 1) designed mainly to separate kaons, pions and protons. Cherenkov photons emitted by relativistic particles above threshold in the 3.3 m long gas radiator are reflected by a mirror wall on two matrices of photon detectors placed above and below the entrance window and outside the spectrometer acceptance. Particles crossing the detector with positive angles with respect to the horizontal plane emit photons which are focused on the upper photon detectors. Photons emitted along the particle path at fixed Cherenkov angle are focused by the mirror wall and form ring images on the photon detectors plane. The ring radius is proportional to the Cherenkov emission angle and allows to calculate the particle speed, once the reflective index of the gas is known, from the well known formula:

$$\cos\theta_c = \frac{\beta}{n} \tag{2.3}$$

Preliminary results on particle identification with RICH1 are shown in Fig. 2.18.

2.4 Data Acquisition System

The COMPASS Data Acquisition System (DAQ) is designed to collect ~ 2 TeraByte of data per day, at a maximum trigger rate of 10^5 Hz. Such performances are achieved by performing data digitalization at the front-end level wherever possible and by using pipelines at various levels to reduce the readout dead time (see Fig. 2.19). Frontend data digitalization is performed mainly using dedicated TDC chips ($\mathcal{F}1$ TDC)[29] which convert wire address and hit time to a formatted 24-bits word which is transmitted to CATCH modules through a 40 Mbits/s serial connection. Local event building is performed in hardware by CATCH modules using FPGA technology and data are transmitted to the Global Event Builder machines through an high-speed fiber optics S-Link connection. Finally the full event is sent to the Central Data Recording at CERN IT division for permanent storage on tape.

The DAQ system allows to parasitically extract samples of the recorded events for monitoring purposes, without degrading the recording speed. This feature is used by the online monitoring software for controlling the overall performances of the various detectors through the graphical presentation of the characterizing detector parameters, as the hit profiles, hit time correlations, ADC spectra, etc. The graphical interface of the monitoring software in shown in Fig. 2.20

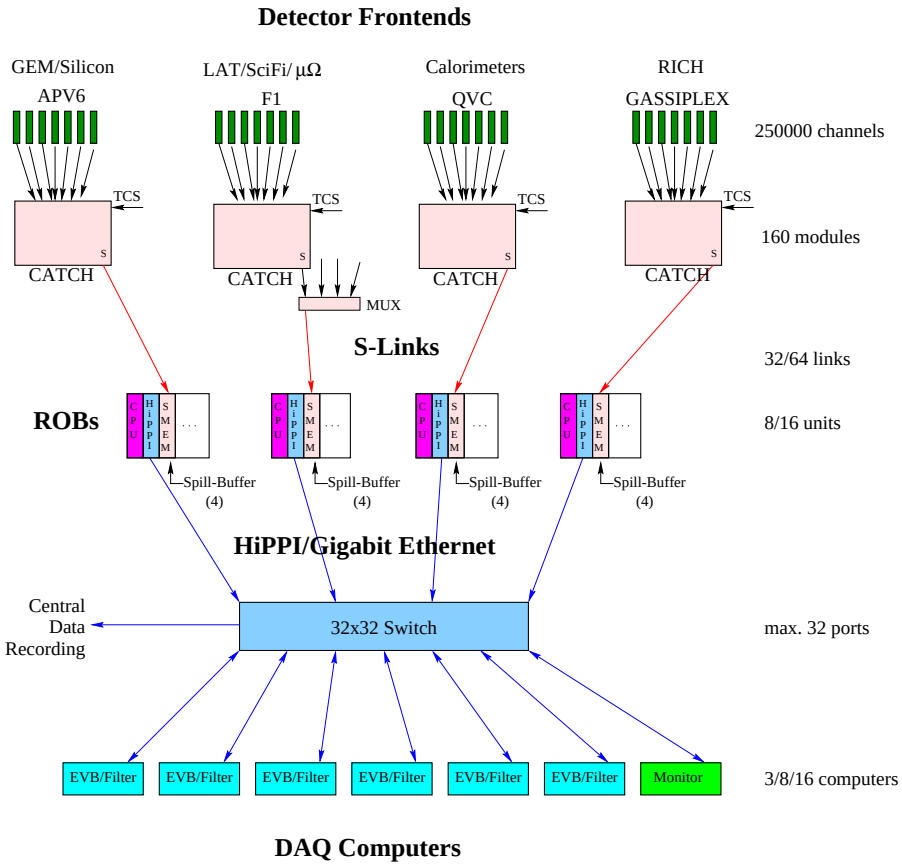

Figure 2.19: *Schematic view of the COMPASS DAQ. The frontend data is collected by the CATCH modules, which implement in hardware the task of local event builders. The data is then transmitted to the global event builders (EVB) through readout buffer machines (ROB). The ROBs are equipped with large memories, enough to store the data corresponding to one complete spill.*

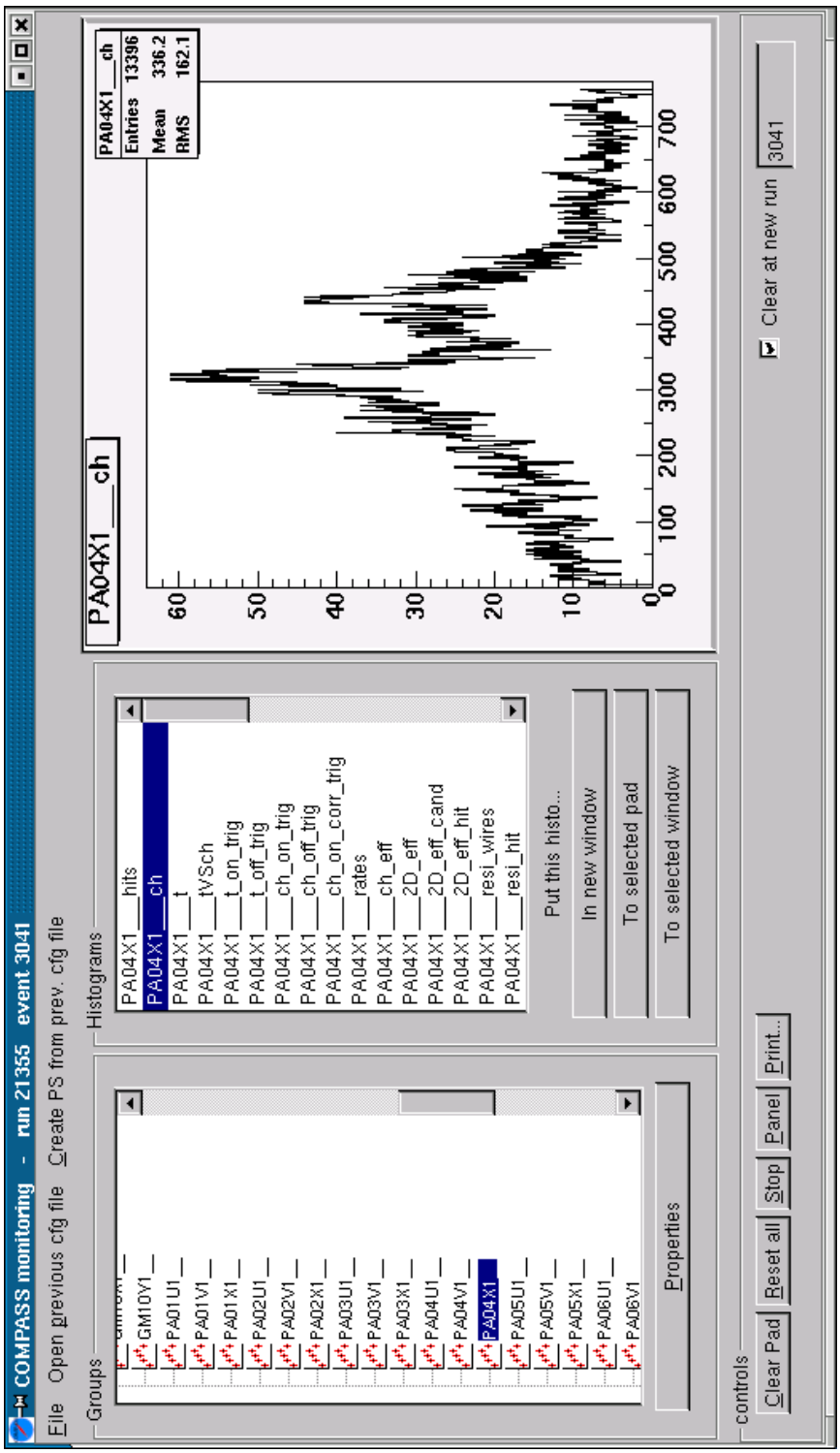

Figure 2.20: *The COMPASS online monitoring program (COOOL).*

Chapter 3

The COMPASS MWPC detector and electronics

3.1 Introduction

The COMPASS spectrometer is equipped with 11 stations of MWPC detectors organized in 34 planes. COMPASS MWPC have been previously used for the Ω spectrometer and have been opened and completely refurbished before installation in the COMPASS apparatus.

3.2 Principle of operation

3.2.0.5 Electrical field in a multiwire structure

The electrical field $E(x,y)$ and the potential $V(x,y)$ inside the sensitive volume of a multiwire structure can be approximately expressed with the following equations[19][20] (see Fig. 3.1 for the definition of the reference system):

$$V(x,y) = \frac{CV_0}{4\pi\epsilon_0}\left\{\frac{2\pi\ell}{s} - \ln\left[4\left(\sin^2\frac{\pi x}{s} + \sinh^2\frac{\pi y}{s}\right)\right]\right\}, \quad (3.1)$$

$$E(x,y) = \frac{CV_0}{2\epsilon_0 s}\left(1 + \mathrm{tg}^2\frac{\pi x}{s}\,\mathrm{tgh}^2\frac{\pi y}{s}\right)^{\frac{1}{2}}\left(\mathrm{tg}^2\frac{\pi x}{s} + \mathrm{tgh}^2\frac{\pi y}{s}\right)^{-\frac{1}{2}}, \quad (3.2)$$

where s represents the wire pitch, ℓ is the distance from the anode wire in the direction perpendicular to the wire plane, ϵ_0 is the vacuum dielectric constant, V_0 is the potential at the anode wire and $V_{cathode} = 0$. The capacity/unit of length is expressed by:

$$C = \frac{2\pi\epsilon_0}{(\pi\ell/s) - \ln(2\pi a/s)}. \tag{3.3}$$

where a is the anode wire diameter.

More significant expressions can be derived by considering the asymptotic

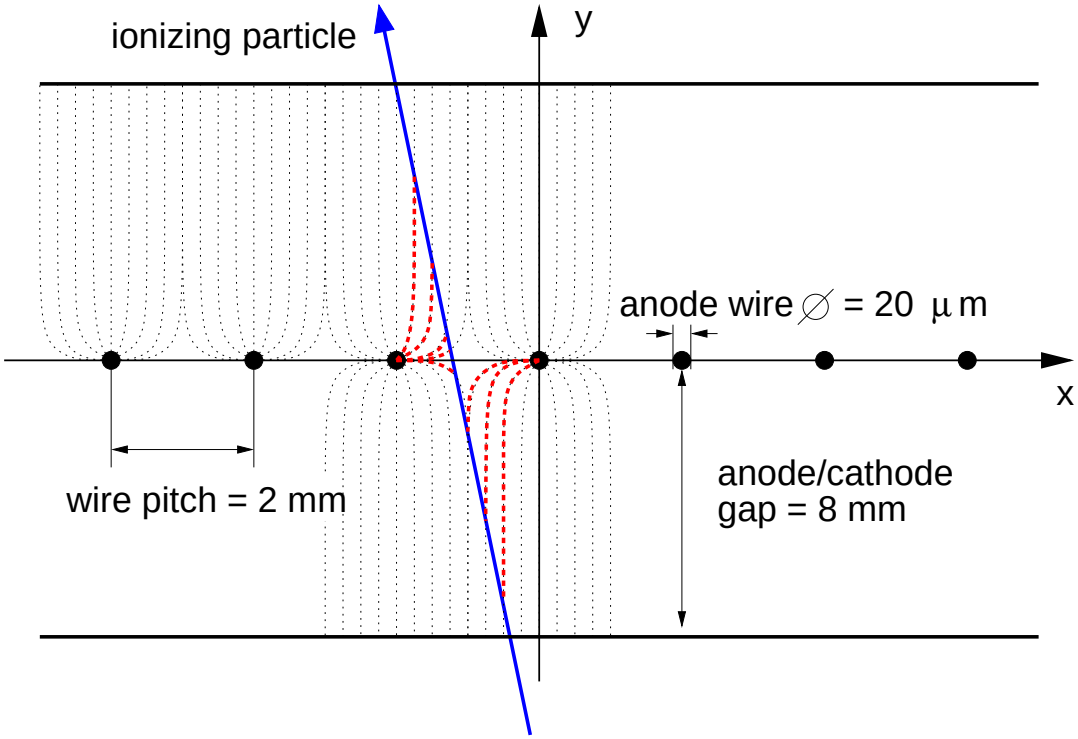

Figure 3.1: *Geometrical characteristics of one MWPC plane. The wire pitch is 2 mm, the anode/cathode gap is 8 mm and the wire diameter is 20 μm (not in scale). The figure shows also schematically the electric field lines inside the gas volume and the drift path of charge clusters formed by an ionizing particle. The maximum drift time depends on the maximum drift path and on the gas mixture used.*

behavior of eqs. 3.1–3.2. For $y \ll s$ we obtain:

$$E(x,y) \simeq \frac{CV_0}{2\pi\epsilon_0}\frac{1}{r}, \qquad r \simeq (x^2+y^2)^{1/2}; \tag{3.4}$$

which is the expression of the electric field inside a cylindrical condenser.
For $y \geq s$ we have:

$$\mathrm{cotgh}\frac{\pi y}{s} \simeq 1, \qquad E_y = E(0,y) = \frac{CV_0}{2\epsilon_0 s}\mathrm{cotgh}\frac{\pi y}{s} \simeq \frac{CV_0}{2\epsilon_0 s}, \tag{3.5}$$

which represents a constant electric field. A multiwire structure thus behaves as a cylindrical condenser, with a radius of few hundred microns, in the region close to the anode wire. This is the region where charge multiplication occurs (multiplication region), while in the rest of the sensitive volume electrons drift with approximately constant speed(drift region). The region where the two asymptotic expressions are not valid (transition region) is characterized by a non-constant drift velocity, but the electric field is not strong enough to start the charge multiplication.

3.3 Detector characteristics

In MultiWire Proportional Chamber detectors the choice of the geometrical parameters is constrained by the requirement of obtaining full detection efficiency in a E/p region where the drift velocity of electrons in the gas is high and the discharge probability is small. A comprehensive study of optimal geometrical parameters of multiwire structures can be found in the literature (see for example [19][21] and references therein). For wire lengths of $\sim$ 1 m, like for COMPASS MWPC, the optimal choices are a wire diameter of 20 μm, a wire pitch of 2 mm and an anode/cathode gap of 8 mm.

In COMPASS three different types of MWPC stations are used, named type-A, type-A* and type-B. Type-A chambers have three wire planes, one vertical and two tilted by $\pm 10.14^\circ$ w.r.t. the vertical axis, and an active area of 178×120 cm^2. Type-A* chambers are similar to type-A, with an additional horizontal plane. Type-B have a smaller active area (178×80 cm^2) and only

two wire planes, one vertical and one either left or right tilted by 10.14°. Type-B stations are composed of two chambers with inclined planed with opposite orientations, fixed together; only three planes, one vertical and two tilted, are read out. The detector characteristics are summarized in Tab. 2.3.

3.4 Choice of the gas mixture

In modern high energy experiments gas detectors can fulfill the experimental requirements of low dead time and high rate capabilities only if fast gas mixtures are used. CF_4-based gas mixture allow to reach electron drift velocities of the order of 10 ns/mm at values of the chamber potential which allow a stable operation of the detector. A detailed study of CF_4-based gas mixtures can be found for example in [23]. An additional advantage of CF_4 is that it is not explosive and does not lead to polymerization at the electrodes, thus reducing the effect of detector aging.

Electron drift velocity in pure argon does not exceed few mm/μs, which leads to a time jitter of the order of 1 μs for the COMPASS MWPC geometry. The process which allows to enhance of the electron drift velocity in argon-based gas mixtures is based on the behavior of the momentum exchange cross section between electrons and argon atoms, shown in Fig. 3.2. The minimum of the cross section corresponds to an electron energy much lower than the mean energy of electrons drifting in the chamber electric field. The addition of a polyatomic molecule with many rotational and vibrational excited states allows to lower the energy of drifting electrons by elastic scattering, until it coincides with the minimum of the argon cross-section. Fast gas mixtures with drift velocity up to $\sim$ 100 mm/μs have been obtained by adding $10 \div 20\%$ of CF_4, as shown in Fig. 3.3. For COMPASS MWPC, a mixture of Argon, CO_2 and CF_4 in proportions 74:6:20 has been used.

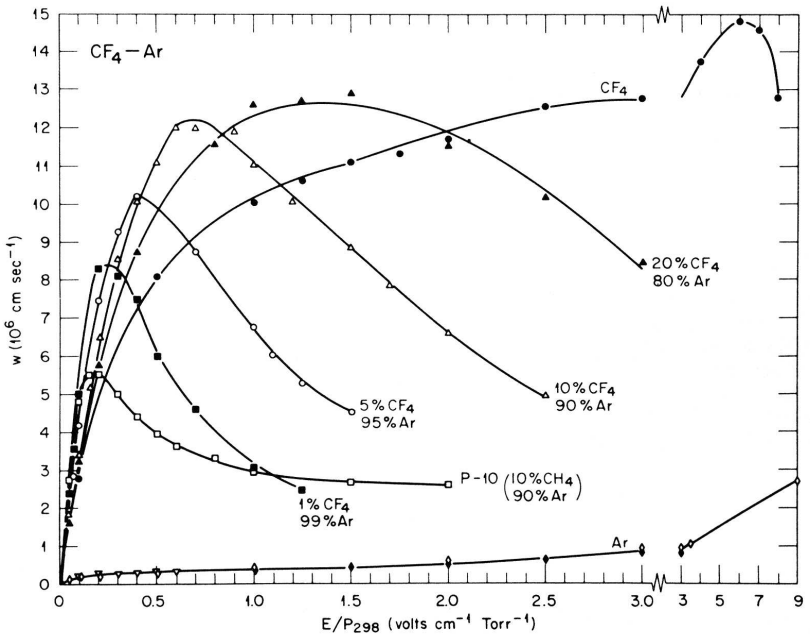

Figure 3.2: *Electron drift velocity as a function of E/P for pure CF_4 and various Ar-CF_4 mixtures.*

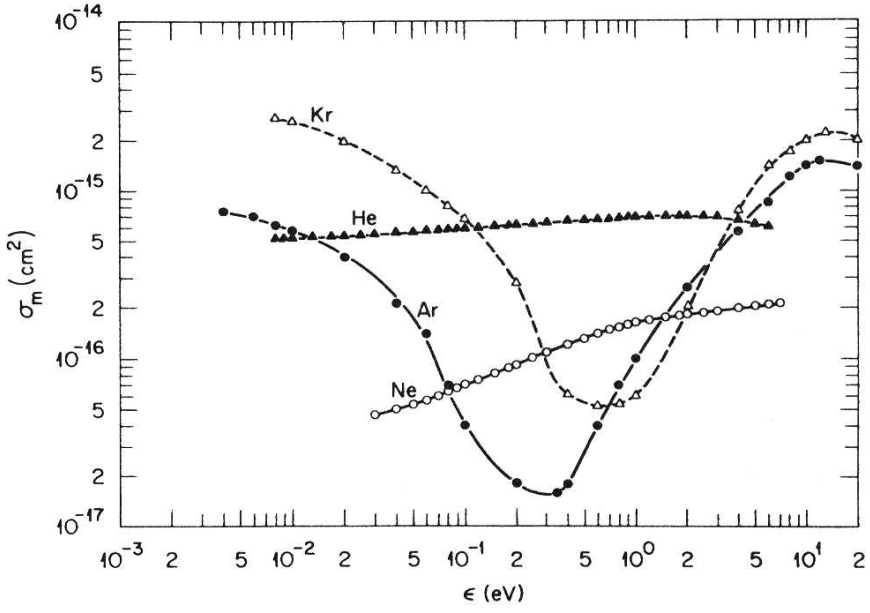

Figure 3.3: *Momentum transfer cross-section, σ_m, as a function of the electron energy ε for He, Ne, Ar and Kr.*

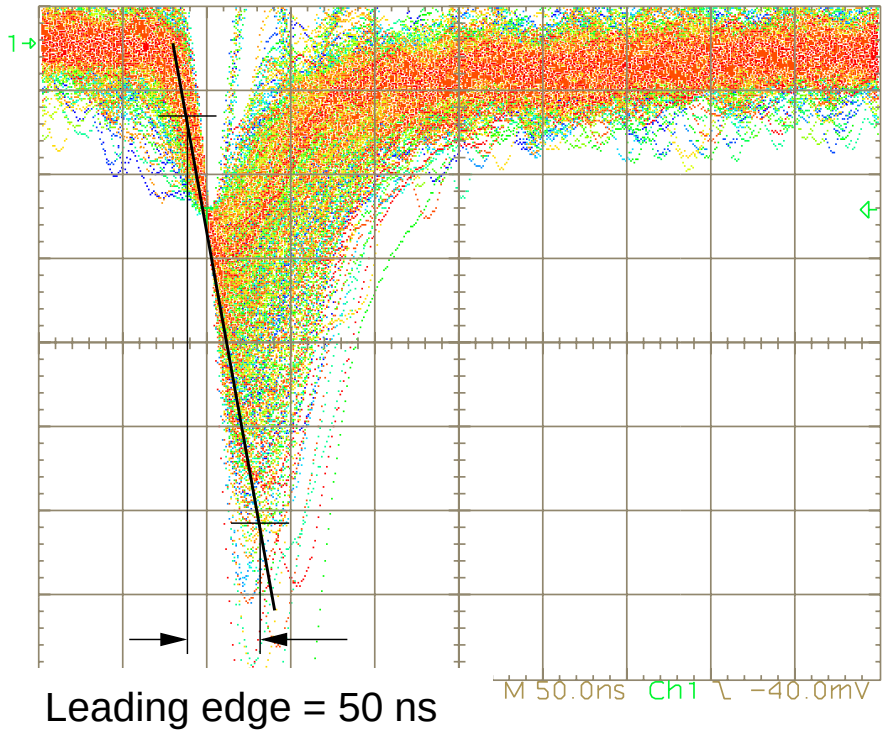

Figure 3.4: *Typical shape of the MWPC wire signal. Chamber potential is 5.4 kV.*

3.4.0.6 Characteristics of the wire signal

The signal produced by gas multiplication detectors has a typical shape, with a sharp leading edge and a longer tail after the signal peak. The amplitude of the peak depends on the number of charge clusters which start multiplication and on the gas gain; the typical signal produced by COMPASS MWPC detectors is shown in Fig. 3.4.

The particular shape of the electric field reflects on the time development of the wire signal. Charge clusters formed in the multiplication region have a short drift path and reach the anode wire in few nanoseconds. On the contrary clusters which are formed in the drift region have a long drift path to follow and will drift with constant speed for several nanosecond before starting multiplication

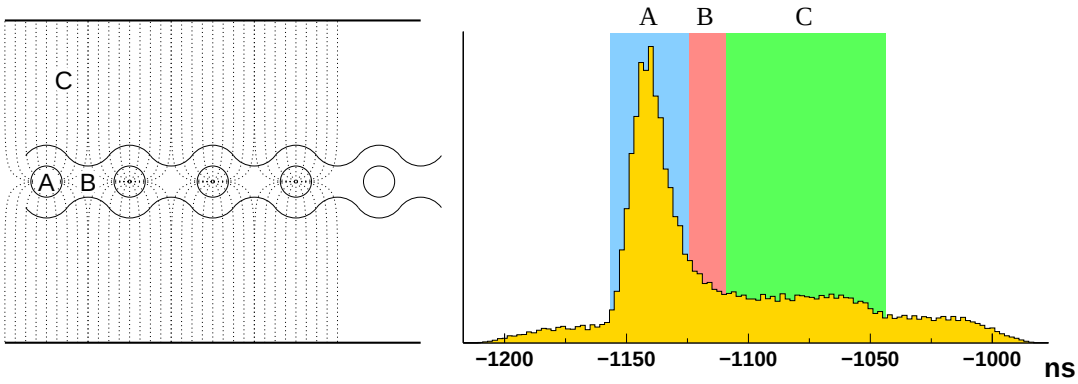

Figure 3.5: *The sensitive volume of an MWPC detector can be divided into three zones: A) multiplication region, B) transition region, C) drift region. Charge clusters generated in the different regions contribute differently to the wire signal timing.*

and being collected by the anode wire. The maximum drift time depends on the anode/cathode gap and the drift velocity; in the case of COMPASS MWPC it is of the order of 80 ns. Charge clusters formed in the multiplication region contribute to the peak of the hit time spectra, while those generated in the drift region contribute to the tail of the distribution (see Fig. 3.5); the length of the tail depends on the maximum allowed drift time.

Another consequence of the particular geometry of MWPC structure is the formation of wire clusters. As shown in Fig. 3.1 it is quite likely that electrons formed along the trajectory of a ionizing particle inside the gas volume drift toward more than one anode wire. In this case a signal will be generated from two or more adjacent wires. The probability of formation of wire clusters depends on the gas gain and the threshold of the front-end electronics discriminators; in typical operating conditions the fraction of wire clusters with size two or more is of the order of 30% (see Fig. 3.6).

A limiting aspect of the MWPC geometry is the space-charge effect due to ions formed in the ionization processes and which recombine at the cathode planes. In the most probable case of electron-ion pairs formed in the multipli-

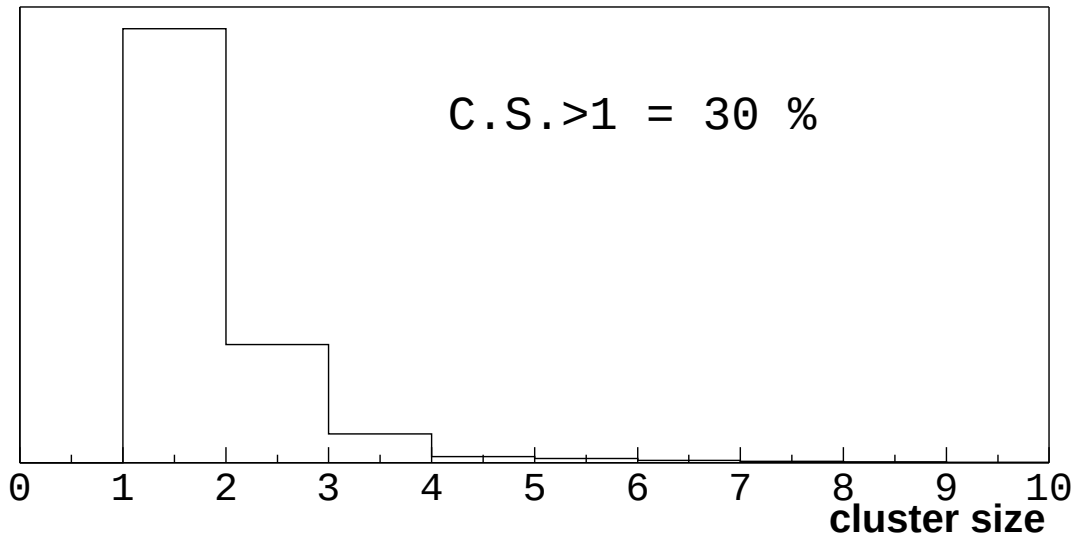

Figure 3.6: *Cluster size distribution for one MWPC plane. The probability of cluster size* > 1 *is around 30%.*

cation region, the ions have to drift for $\sim$ 10 mm before recombination. The presence of a positive charge in the sensitive volume has the effect of distorting the electric filed and reduce the gas gain and thus the amplitude of the signal at the anode wire. Since the drift velocity of ions in a gas is smaller than for electrons, the ions recombination rate at the cathodes defines the maximum allowed particle flux. If the ions production rate is higher than the recombination rate the space charge effect becomes strong enough to avoid electrons multiplication and the detector is "dead" until enough ions have been collected at the cathodes.

3.5 Readout electronics

The MWPC electronics development was one of the Torino responsibilities in the COMPASS experiment during the past years. The project has been completed in year 2001 with the definition of the final frontend electronics design and the installation of $\sim$ 24000 readout channels. The additional $\sim$ 2400 required for a

new MWPC station have been installed at the beginning of year 2002.

The low-noise, low-dead time readout electronics used in COMPASS is schematically shown in Fig. 3.7. The main components of the system are

1. the mother-board;
2. the front-end readout board;
3. the CATCH module.

The mother-board is a printed circuit board fixed to the chamber frame. It provides electrical and mechanical connection between sensitive wires and the front-end boards. It also provides the interface to a test system capable of injecting calibrated pulses simulating the signal of a minimum ionizing particle. The system allows the automatic test of the frontend channels and of the read-out chain, including the input connectors. A large surface ground connection exists between the chamber ground and the mother-board for better screening the wire signals and for electronics noise reduction.

The front-end cards are the read-out digitizer components. They house the preamplifier/discriminator chips, the $\mathcal{F}1$ TDC chips, the threshold DACs and the high speed parallel-to-serial converter chips for the data transmission. To reduce the costs the front-end boards are organized in triplets connected by a 40 MHz LVDS (Low Voltage Differential Signal) bus. The three boards share a common design and schematic, except for the data transmission section which is housed only on the central board and controls a total of 192 front-end channels.

The wire signal digitalization is performed by the preamplifier and discriminator ASISCs MAD4 [28], originally developed by the Padua I.N.F.N. laboratories for the CMS drift chambers. The chip logic is schematically shown in Fig. 3.8. The structure of each readout channel is the following: an input stage composed of a low-noise preamplifier followed by a shaper and a baseline restorer integrates and amplifies the first $\sim$ 5 ns of the wire signal, which is then compared to an externally supplied threshold voltage and a converted to a digital level. The digitized signal is then fed to the LVDS differential output driver.

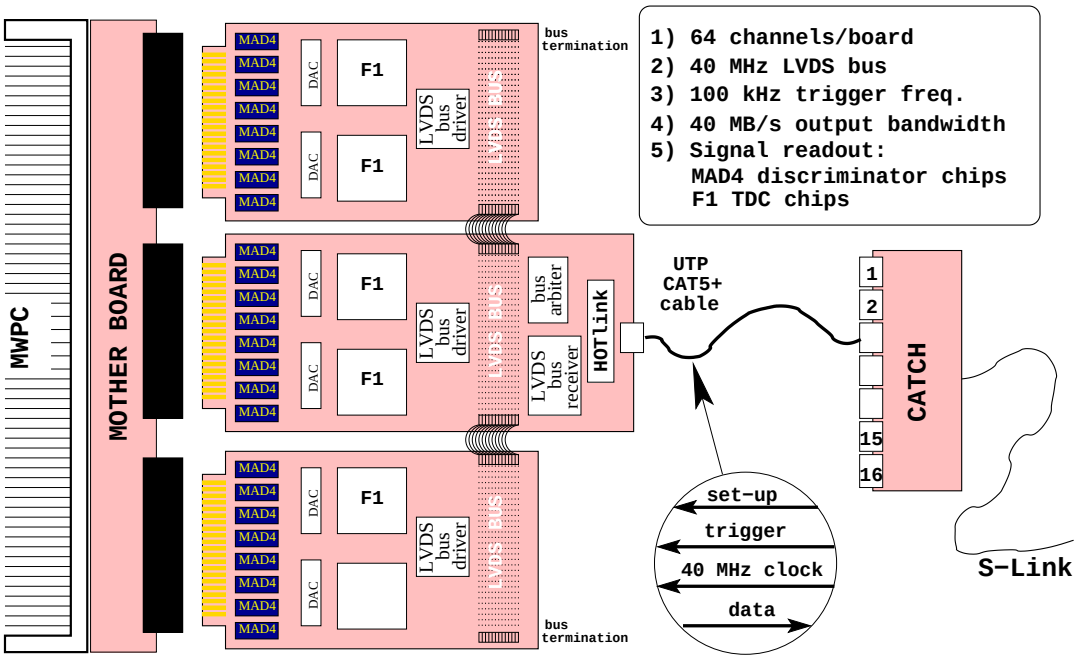

Figure 3.7: *Scheme of the front-end card housing the preamplifier/discriminators, digitizing electronics, and interfaces.*

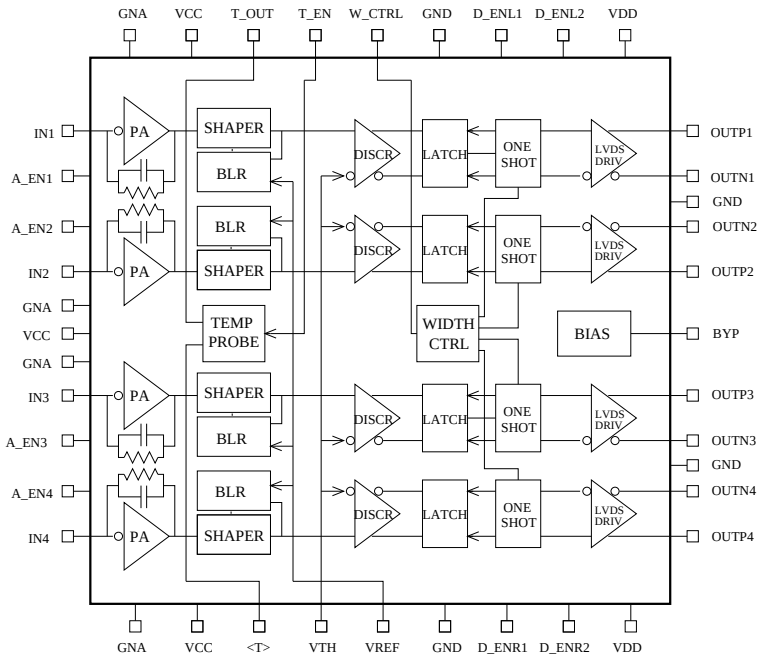

Figure 3.8: *Schematic view of the MAD4 chip logic.*

The wire signals discriminated by the MAD4 are digitized, i.e. converted into the logical address of the hit wire, by 6 $\mathcal{F}_1$ TDC chips[29] for each frontend triplet. This chips, developed by the University of Freiburg, are widely used by several detectors in COMPASS for hit time measurements. In the standard mode the $\mathcal{F}_1$ chip is an eight channel TDC with an uncertainty of 150 ps. In the high resolution operating mode, two adjacent channels can be grouped together, and the uncertainty is lowered to 75 ps. The maximum input rate is 6 MHz per channel, and the double pulse resolution is 22 ns. When precise timing measurement is not required but the cost of a single readout channel is a critical issue, 4 input channels can be read-out by the same TDC channel (latch mode), with a precision of 5.7 ns. This feature is used in the MWPC frontend electronics to limit the number of TDC chips required for each triplet; 6 TDC chips are used for 192 input channels. The $\mathcal{F}_1$ chips are also able to drive an eight-channel, serial-input, digital-to-analog converter AD8842, which is used in the frontend electronics for threshold control of the discriminator chips.

This chips perform the digitalization of the wire hit by generating 24-bits data words containing informations on the hit time and wire address. One data word is generated for each fired wire, and some additional header and trailer word are added to the data stream for synchronization and readout debugging purposes. The generation of the digitalized data words is synchronized to a trigger signal provided by the COMPASS Trigger Control System (TCS). Since the trigger signal is delayed with respect to the detector signal by ~ 1 μs, wire hits are internally buffered by the TDC and the trigger latency is added to their time stamp before performing the trigger matching.

The key features of the COMPASS MWPC frontends are fast detection and low readout dead-time. Fast detection is provided by the small integration time of the MAD4 chips. This chip provides a double-pulse resolution of 25 ns, corresponding to a maximum input rate of 40 MHz. The low dead-time of the wire signal discrimination/digitalization process is on the other hand provided by the pipelined structure of the $\mathcal{F}_1$ TDCs. The wire hit information is internally stored by the TDC inside buffers which provide enough memory to account for

the trigger latency, and no dead-time is introduced at the level of frontend readout.

3.5.1 Laboratory tests of front-end chips

At the time when the electronics was developed two preamplifier and discriminator chips specifically designed for gas detectors were available in the high energy physics community. The first one, designed at the University of Pennsylvania, was optimized for the straw tube detectors of the SSC experiment [25][26][27]. The chip, named ASD-8, contains 8 independent channels of preamplifier, discriminator and output driver on a single chip. The second one is the already mentioned MAD4. Detailed information can be found in [30][33]. Here I just want to recall some of the main features of the MAD4 and $\mathcal{F}1$ TDC ASICs.

The MAD4 chip operates with a single threshold voltage which is common to all the four channels. This could be a limiting feature in the case of big differences in the response of each channel. For this reason the threshold/input charge calibration curve has been carefully measured; the results are shown in Fig. 3.9. One of the interesting features of the MAD4 chip is the linearity of the threshold as a function of the input charge (calibration curve). Three points along the curve are enough to calculate the correct threshold voltage for any value of input charge in a very wide range. A slight deviation from linearity is visible only for small input charge values, where the measurement starts to be affected by the electronics noise.

The electronics noise can be measured indirectly from the counting rate as a function of threshold voltage, at fixed input signal amplitude. The ideal response is a step curve with a transition at the threshold voltage corresponding to the injected charge. Fluctuations of the signal amplitude at the discriminator stage have the effect of smoothing the response curve. The statistical distribution of the signal is directly measured from the derivative of the response curve; in the hypothesis of a normally distributed noise a fit with a gaussian curve provides an estimate of the overall electronics noise (see Fig. 3.10-left). The measured values are shown in Fig. 3.10-right and are consistent with the values

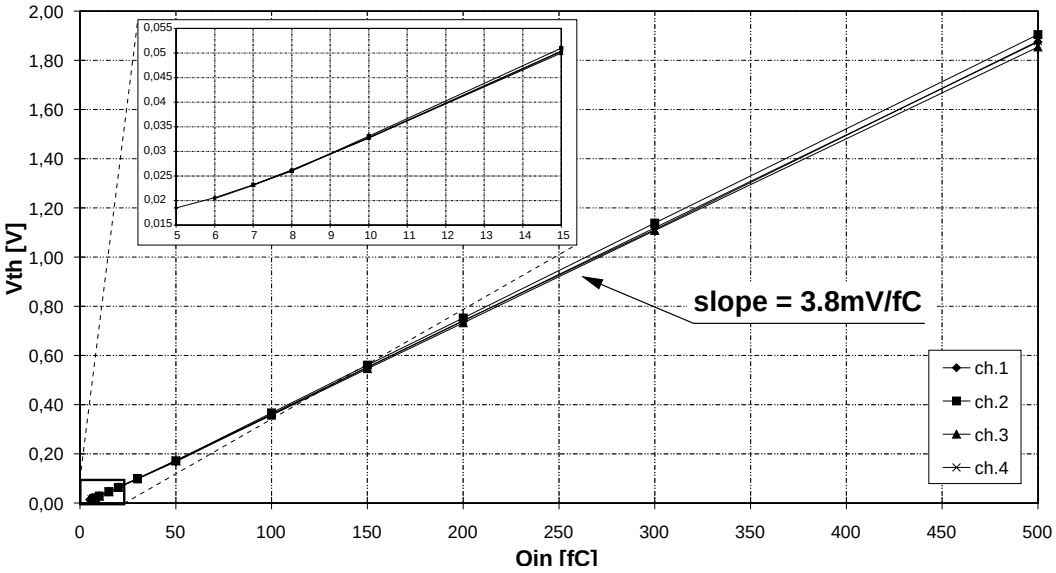

Figure 3.9: *Threshold/input charge calibration curve for one MAD4 chip.*

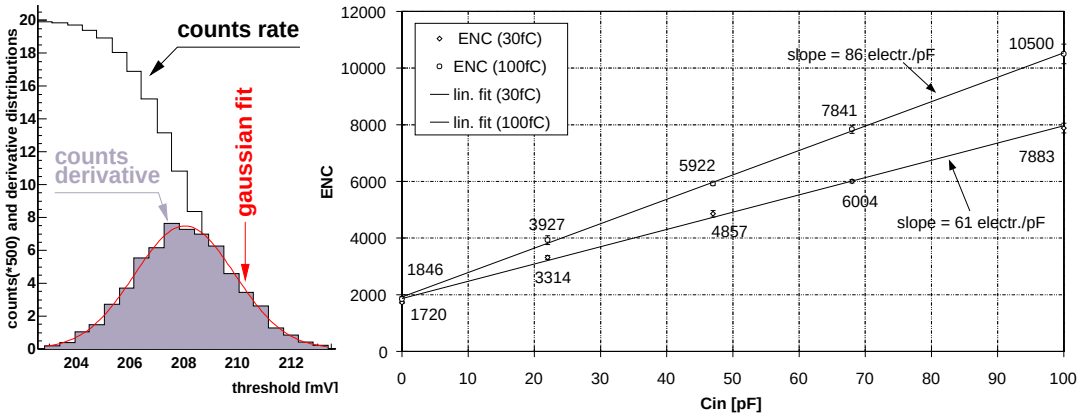

Figure 3.10: *Electronics noise (expressed in Equivalent Noise Charge) as a function of input signal amplitude and input capacity.*

quoted in the data-sheets.

The rate capabilities of the MAD4 chip have been investigated by measuring the threshold level at fixed input signal amplitude, for increasing values of the input frequency. The results are plotted in Fig. 3.11 for two different signal amplitudes , and show a stable response up to 4 MHz. The result is in agreement with the declared double pulse resolution of 25 ns.

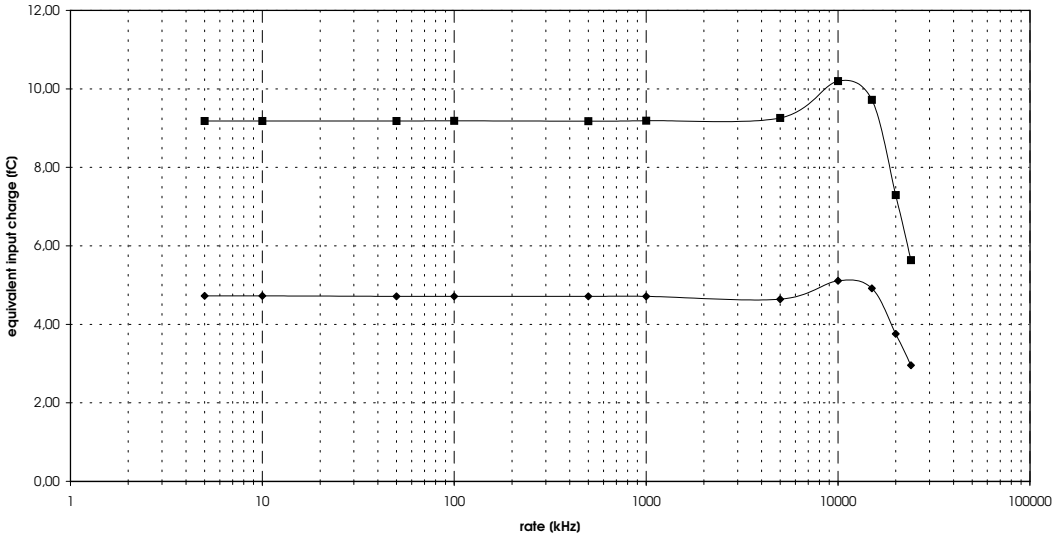

Figure 3.11: *Dependence of the MAD4 response on the input signal frequency. The threshold level at fixed signal amplitude is stable up to 4 MHz, corresponding to a double pulse resolution of 25 ns.*

3.5.2 Tests with small chamber prototipe

The properties of Ω chambers operated with pure CF_4 have been investigated using a small chamber prototipe [31][32]. Pure CF_4 (purity 99.995%) from Air Liquide has been used for the tests, with a flow of about 0.5 l/h. The chamber prototipe, with the same characteristics as the Ω chambers in terms of wire pitch, wire diameter, wire tension (50 g), and anode-cathode gap, has been made by the LNP Dubna group for the investigation of basic MWPC working parameters. The length of the 16 sensitive wires is 70 mm with a typical capacity of 11.6 pF. The cathode is made of 10 μm aluminized mylar film.

The chamber has been tested using the setup shown in Fig. 3.12. The minimum ionizing particles emitted by a collimated β^- ^{90}Sr source cross the sensitive volume of the chamber and are detected by 30×40 mm^2 scintillator read out by two photomultipliers in coincidence. The trigger setup allows to reject PM noise but not the cosmic rays, which are however educed to few counts per second by the small surface of the scintillator.

The DISTO DAQ system [24], based on the LeCroy PCOS III system, has

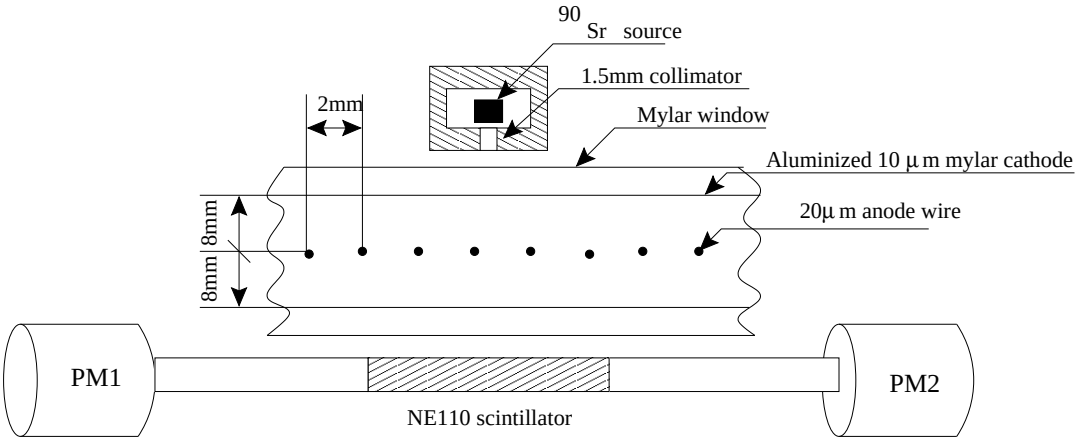

Figure 3.12: *The test system includes a small chamber prototipe, a collimated β^- source, and a double coincidence scintillator trigger.*

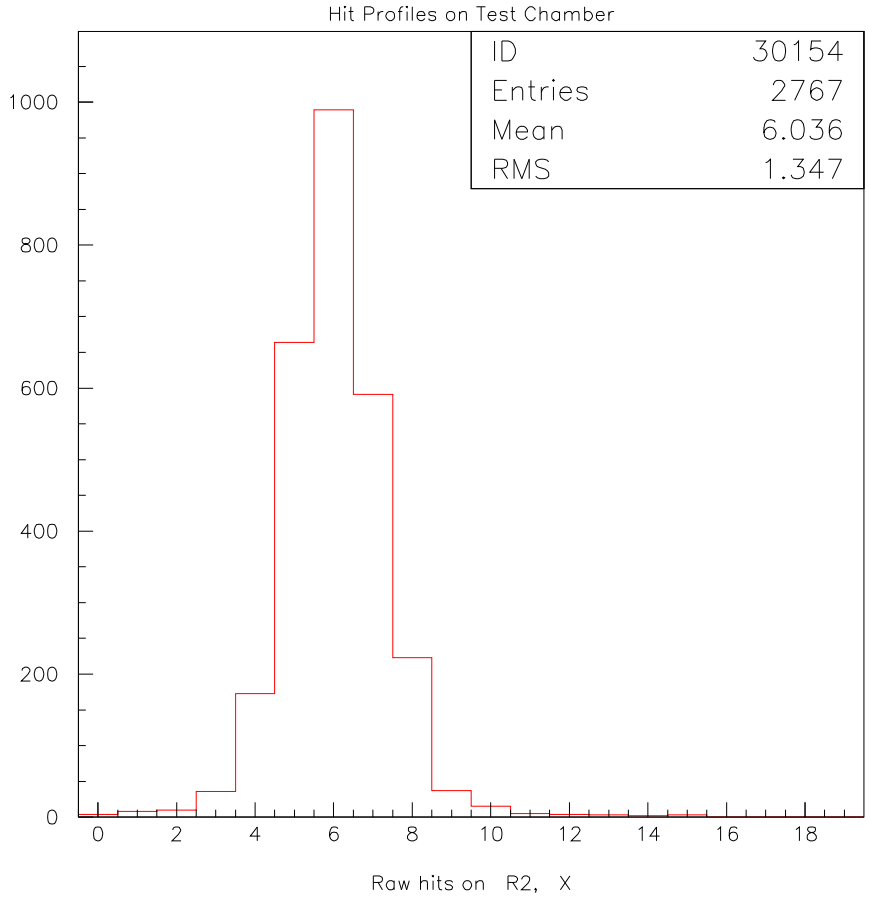

Figure 3.13: *Hit profile on the prototipe chamber. The β^- source is centered on the active area.*

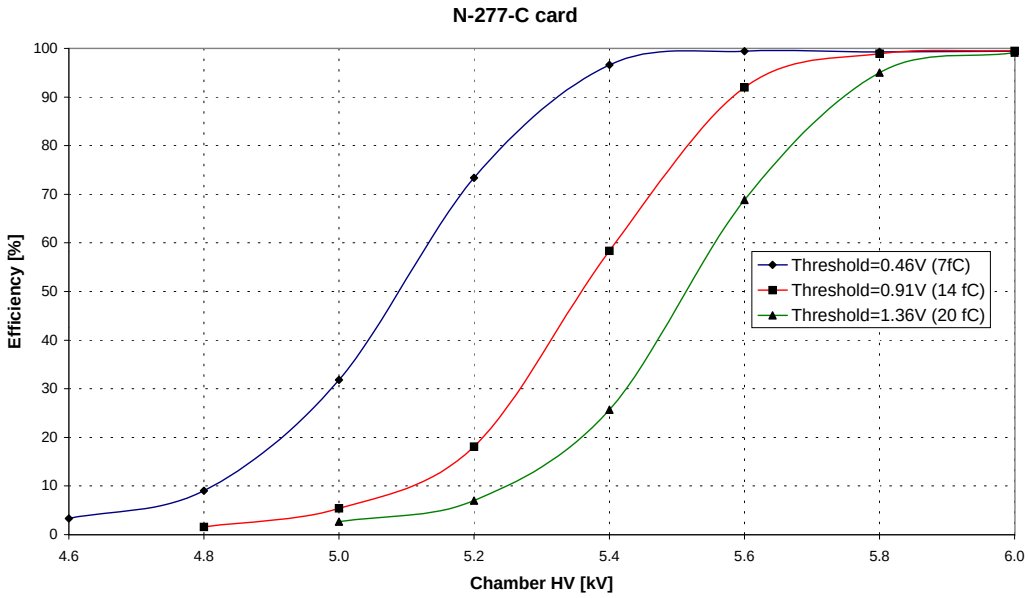

Figure 3.14: *Nanometrics card: efficiency vs. chamber potential for three different threshold settings (7, 14 and 20 fC), with pure CF_4 gas.*

been used for the readout. Hit time measurements have been performed using a commercial LeCroy 2228 TDC module. The start signal for the TDC measurement was the trigger signal itself, while the stop was given by the output of the peak channel in the hit profile of Fig. 3.13. The commercial Nanometrics N-277-C cards have been used for preliminary check of the setup assembly. This cards are the standards PCOS III frontend cards, extensively used in the DISTO experiment. The threshold for this cards was remotely set by the DAC included in the PCOS III latch module. Fig. 3.14 shows the measured efficiency as a function of chamber potential, for three different settings of frontend threshold. The efficiency behavior is typical of a well assembled test setup. The high values of chamber potential required to reach efficiency values $> 98\%$ are due to the use of pure CF_4.

The gas gain was measured using a Camac ADC and the Finuda experiment current amplifier. It consists of a twin linear, fast and low noise amplifier, mounted on a sole board. It can be used both as a differential amplifier or as two independent amplifiers. The twin Finuda preamplifiers have been modified

for the tests, in order to share the same input, connected to the OR of the 16 wires of the chamber prototipe. The linearity of the amplifier and ADC assembly has been checked before the measurements, and resulted to be good up to $\sim$ 120 fC of measured charge.

The charge spectra, measured for three different chamber potentials, are shown in Fig. 3.16, together with the ADC baseline measured using a random trigger.

After setup validation, several measurements have been performed using MAD4- and ASD-8-based prototipe readout boards, in order to compare chamber performances with the two frontend discriminator chips. In particular the two chips have been compared with respect to the achievable detection efficiency, the cluster size and the electronics noise. The efficiency as a function of the chamber potential is shown in Fig. 3.18 for the ASD-8 (top plot) and MAD4 (bottom plot) based prototipe boards, for several frontend threshold values. The minimum threshold value is 4.o fC for both chips. Below this limit continuous self-oscillations of the chip are triggered and the measured efficiency does not reach 0% even for low values of the chamber potential. By comparing the two plots of Fig. 3.18 we can deduce that the noise of MAD4 is significantly smaller than that of ASD-8.

The cluster size =1 probability as a function of the chamber potential is shown in Fig. 3.19 for the ASD-8 (top plot) and MAD4 (bottom plot) based prototipe boards, for several values of the frontend threshold. The probability of getting a single hit per event saturates at 50% for the ASD8 card, even at very large gas gain, while it continues to decrease down to 10% for the MAD4 card. This result was mainly due to the different ground layout of the ASD-8 and MAD4 prototipe cards. The intrinsic cross-talk measured for the two chips was comparable and of the order of 0.4% for the ASD-8 and 0.6% for the MAD4. The use of separate analog and digital grounds in the final frontend electronics design has solved the problem. A detailed study of the cluster size, cross-talk and MWPC spatial resolution is presented in the next chapter.

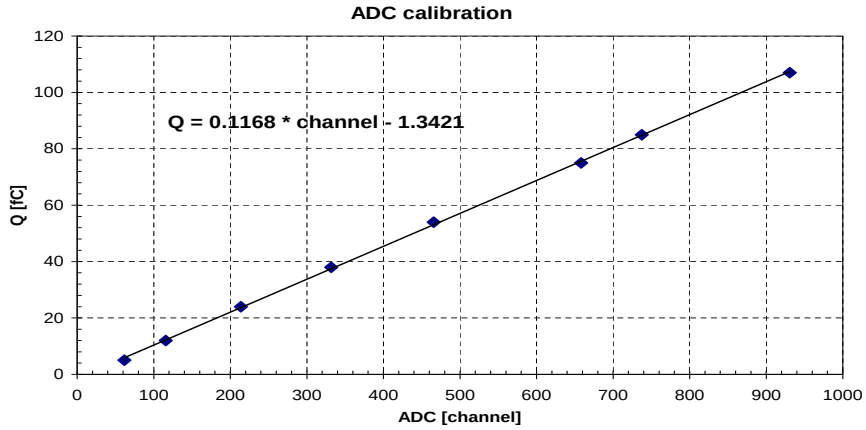

Figure 3.15: *Calibration of the Finuda amplifier and Camac ADC set-up.*

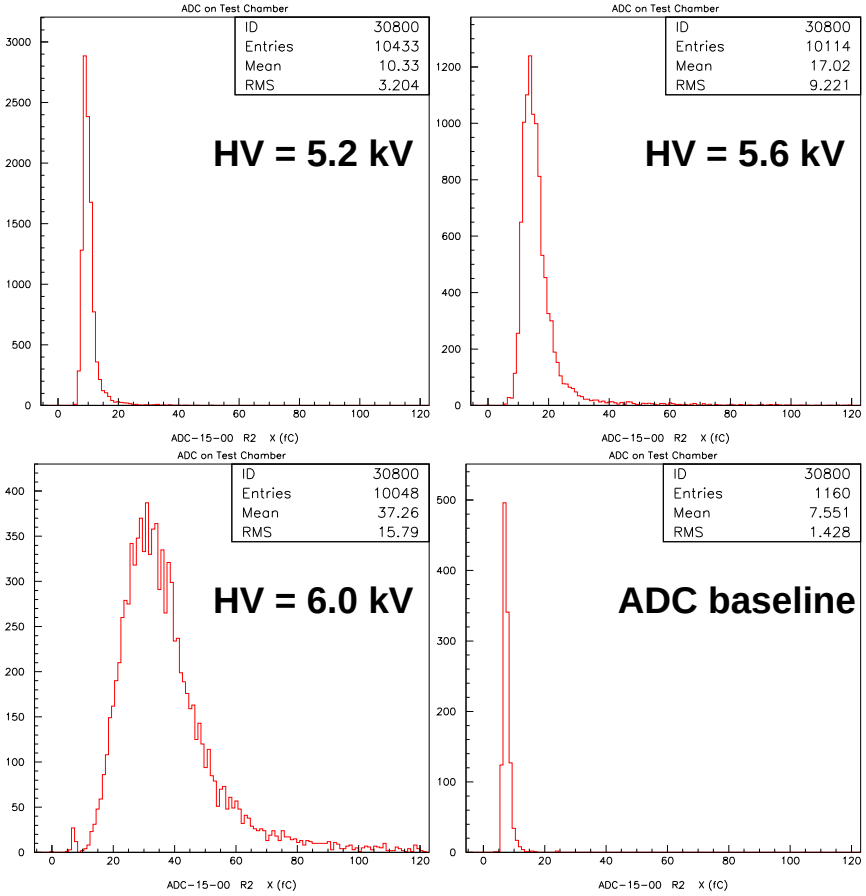

Figure 3.16: *Charge distribution for three different chamber potentials. ADC baseline is also shown in the bottom-right plot.*

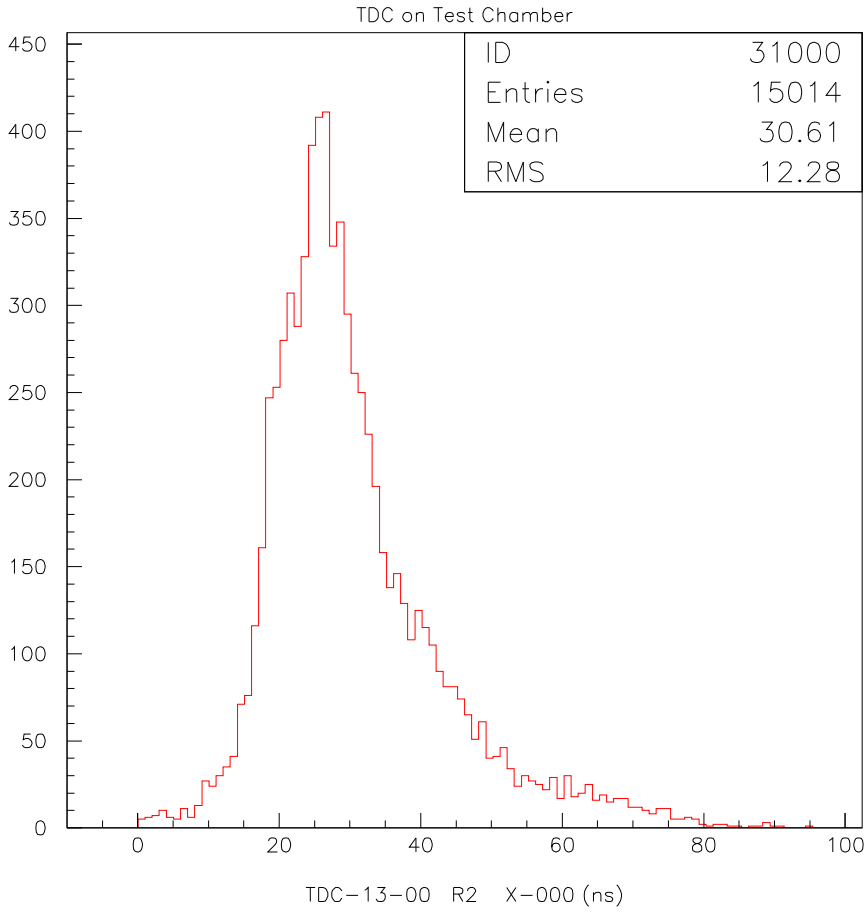

Figure 3.17: *Distribution of the wire hit time, measured at 5.6 kV of chamber potential and 6 fC. The total jitter is* ~ 70 *ns.*

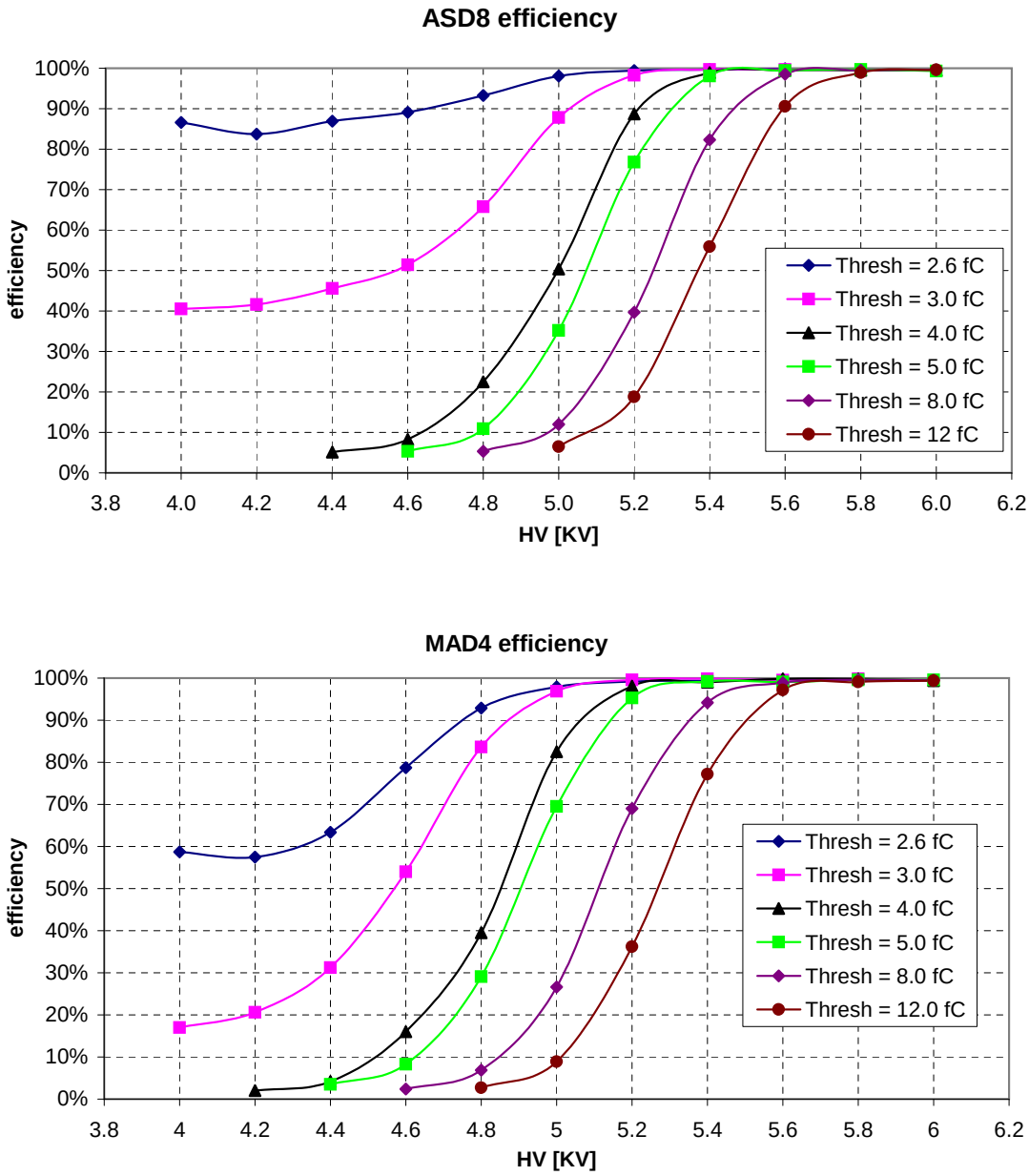

Figure 3.18: *Efficiency vs. chamber potential for various threshold settings, with pure CF_4 gas. Top plot is obtained with ASD-8 prototipe board, bottom with MAD4.*

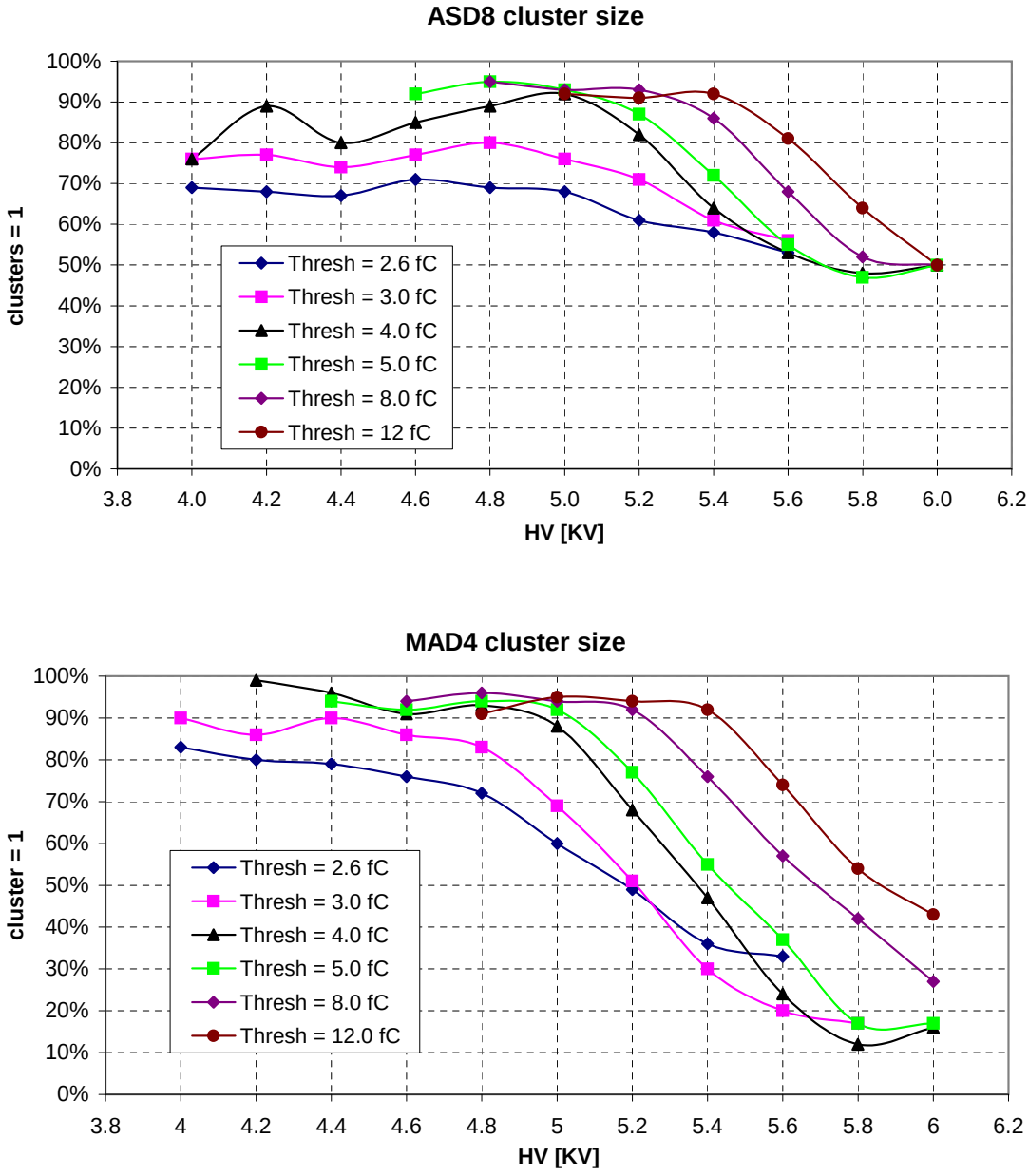

Figure 3.19: *Cluster size =1 probability vs. chamber potential for various different threshold settings. Top plot is obtained with ASD-8 prototipe board, bottom with MAD4.*

3.6 Online test system

The monitoring of 26000 channels of readout electronics is needed. This is a complex task that requires automatic online test facilities to maintain stable working conditions. Precise informations on the front-end electronics stability are acquired through an online test system studied and developed in the INFN laboratory of Torino. The system is designed to inject calibrated pulses similar to the signal of a minimum ionizing particle into each readout channel; it allows to test the complete readout chain including the input connectors. The system is composed of the two following parts:

- the pulser box, housing the programmable pulse generators and mechanically connected to the MWPC frame;
- the VME control board for programming the pulser boxes and performing automatic test cycles.

3.6.0.1 VME control board

The control board is a A24-D32 VME module which provides the interface to the pulser boxes mounted over each MWPC station. The board is able to individually address each pulser output, to set the pulse amplitude or generate a single test pulse. The controller board is designed to work in two different operating modes: hardware mode and software mode. In the first mode an hardware processor implemented in the board logic executes automatic test cycles with programmable pulse amplitudes. The number of outputs pulsed at the same time can be programmed as well. At each step a calibrated pulse is sent to a set of frontend channels in such a way that after a complete test cycle all 26000 channels have been tested. Up to 4 different pulse amplitudes can be programmed in order to check frontend channels response below and above threshold. The number of MWPC stations and frontend channels pulsed at each cycle step can be programmed as well. Each cycle step is synchronized to a special calibration trigger provided by the COMPASS DAQ, and test data are recorded on tape for further offline analysis. In software mode the test

procedures are completely controlled via VME commands. A certain number of VME registers allow to program each DAC channel individually, and a command is provided to generate a calibrated test pulse on the frontend electronics. This operating mode is used to periodically calibrate the readout channels without the need of dismounting the frontend electronics, as described in App. A.

3.6.0.2 Pulser box

The pulser box electronics is composed of a motherboard and up to 16 DAC boards housing two programmable DAC chips each. The pulser box is controlled through a 10 Mbit/s serial line, which is by the VME controller board to send the commands for setting the pulse amplitudes and generating the test pulses.

Each DAC output is connected to a test input on the frontend motherboards and injects the signal into 48 readout channels of the same frontend triplet, as shown schematically in Fig. 3.20. The connections between DAC outputs and test inputs are arranged in such a way that one readout channel over four can be injected independently and crosstalk measurements can be performed. With this configuration one MWPC plane (768 readout channels) requires 8 DAC channels (16 pulse outputs). The DAC chips used for the test pulses generatio allow to set the pulse amplitude from 0 up to ~ 30 fC, in steps of ~ 0.25 fC.

The schematic view of one MWPC station connected to the online test system is shown in Fig. 3.21.

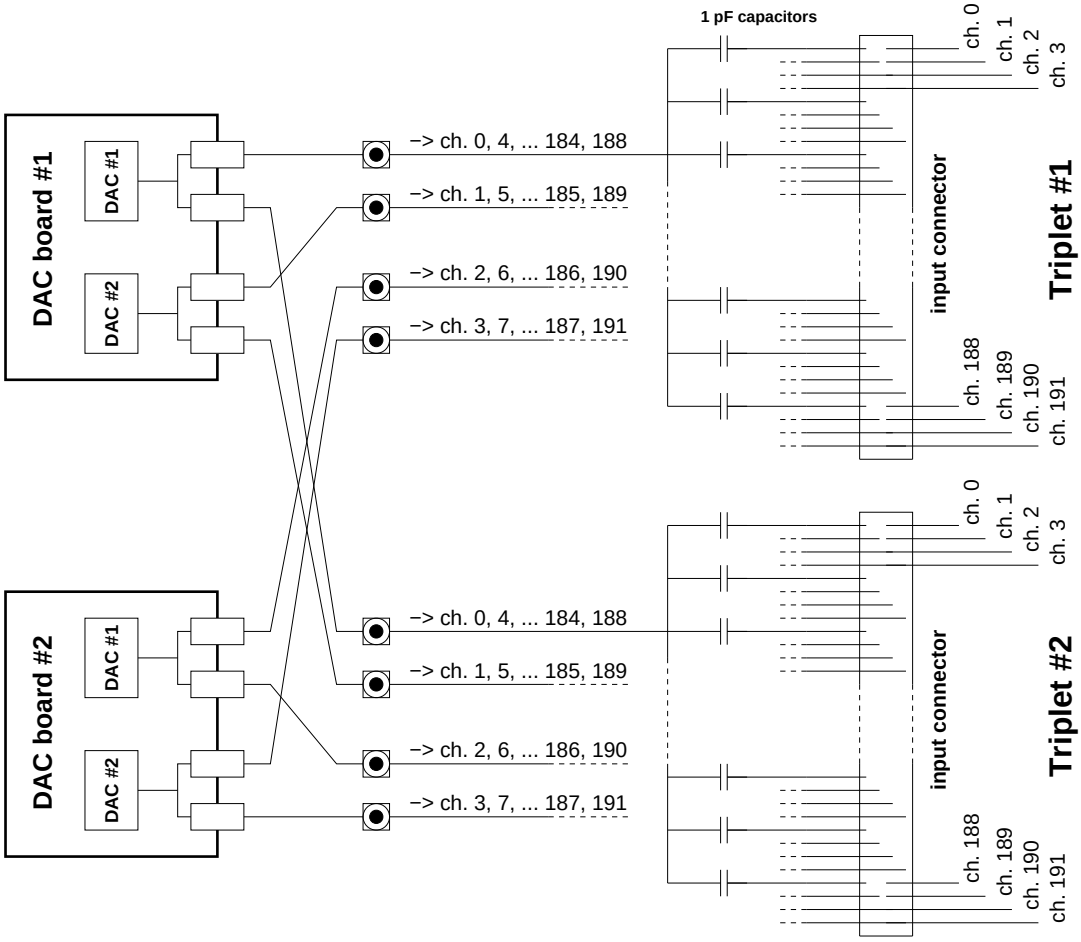

Figure 3.20: *Schematic view of the connections between the pulser box outputs and the frontend readout channels.*

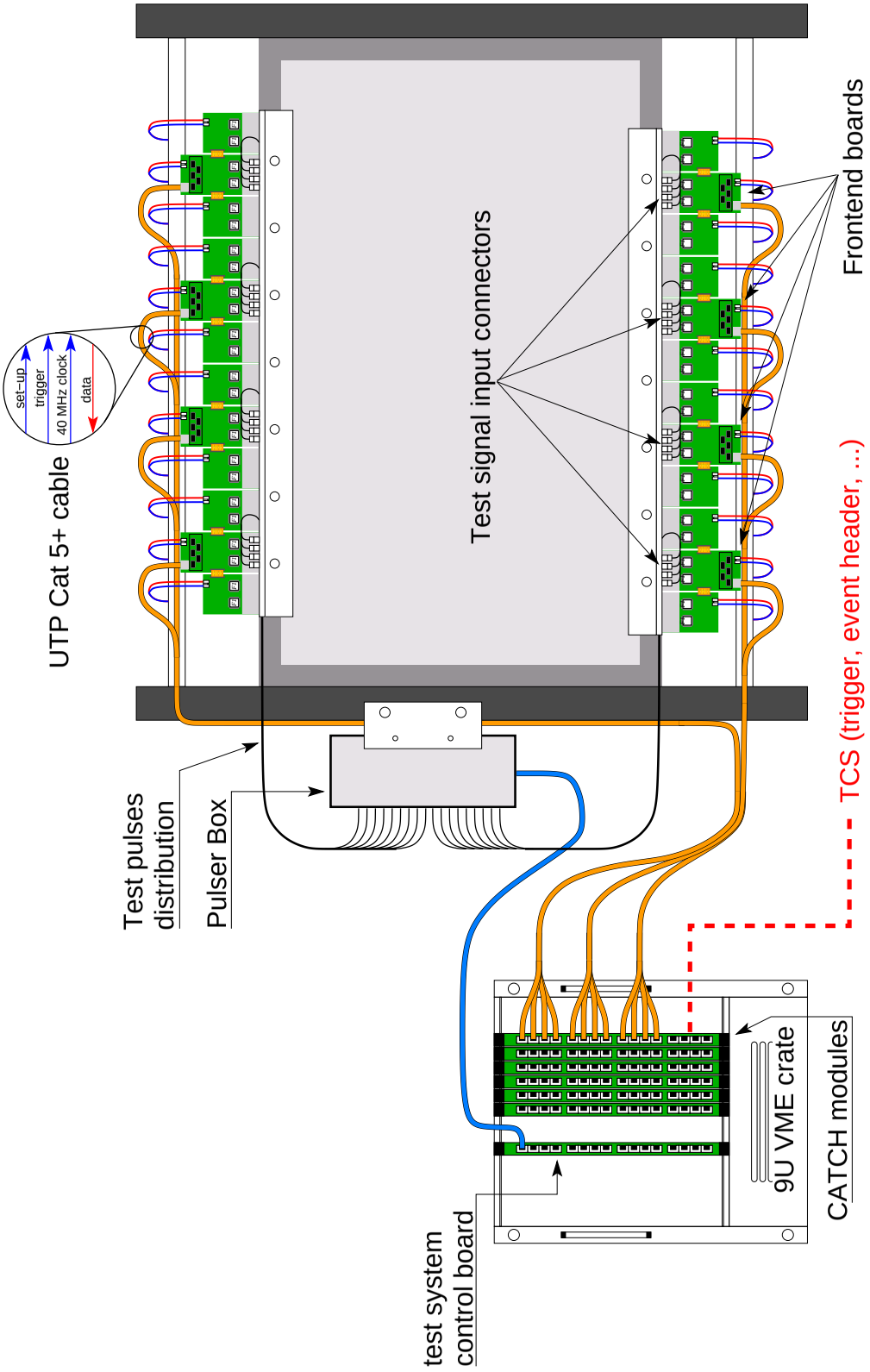

Figure 3.21: *Schematic view of one MWPC station connected to the online test system.*

Chapter 4

MWPC detector performances during 2001-2002 data taking

4.1 Introduction

The installation of 11 MWPC stations has been completed at the beginning of summer 2002. After installation the detectors have been operated for 3 months using a beam of 160 GeV muons with a typical intensity of $2 \cdot 10^8$ particles/spill. A certain number of special runs has also been taken for alignment purposes, with low intensity beam and magnets switched off. The same runs can be conveniently used to extract some intrinsic properties of the detector like hit timing properties and spatial resolution, since the pile-up contribution is negligible and tracking is simplified by the absence of magnetic field.

All MWPC stations are placed in the apparatus with their dead zone centered on the beam trajectory. The geometrical size of the circular dead zone depends on the distance from the target and consequently the size of the beam spot, in order to keep the particle flux in the active area low enough to avoid discharges and prevent detector aging. The typical hit rate per channel for one MWPC plane is shown in Fig. 4.1; the effect of the dead zone is visible in the plot as a reduction of the rate for the central channels.

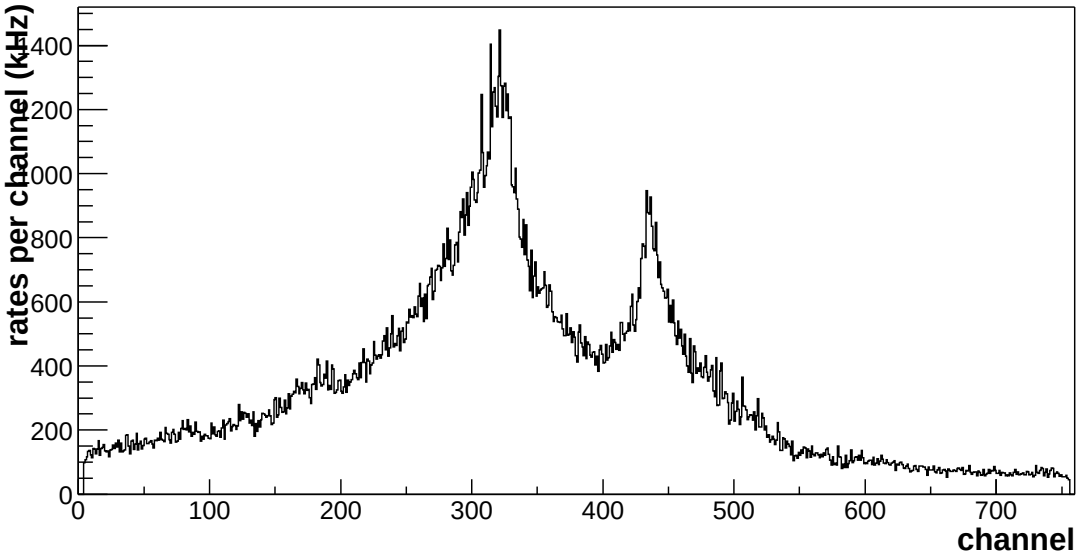

Figure 4.1: *Typical hit rates profile for one MWPC plane. The reduction in the center of the plot is due to the presence of a circular dead zone centered on the beam crossing point.*

4.2 Laboratory tests of MWPC detectors

All MWPC stations have been extensively tested in the laboratory before installation. Efficiency, noise performances, crosstalk and electronics channel calibration have been studied with the aid of the semiautomatic test system described in the previous chapter.

4.2.0.3 Noise performances

MWPC electronics noise performances have been studied in the laboratory and during detectors installation. Best results could only be achieved by calibrating each individual read-out channel separately. This is obtained by measuring the channel threshold for a given set of injected signal amplitudes, as described in App. A. This procedure allowed to produce a database of calibration parameters which are read during the front-end initialization and grant an uniform response of all channels.

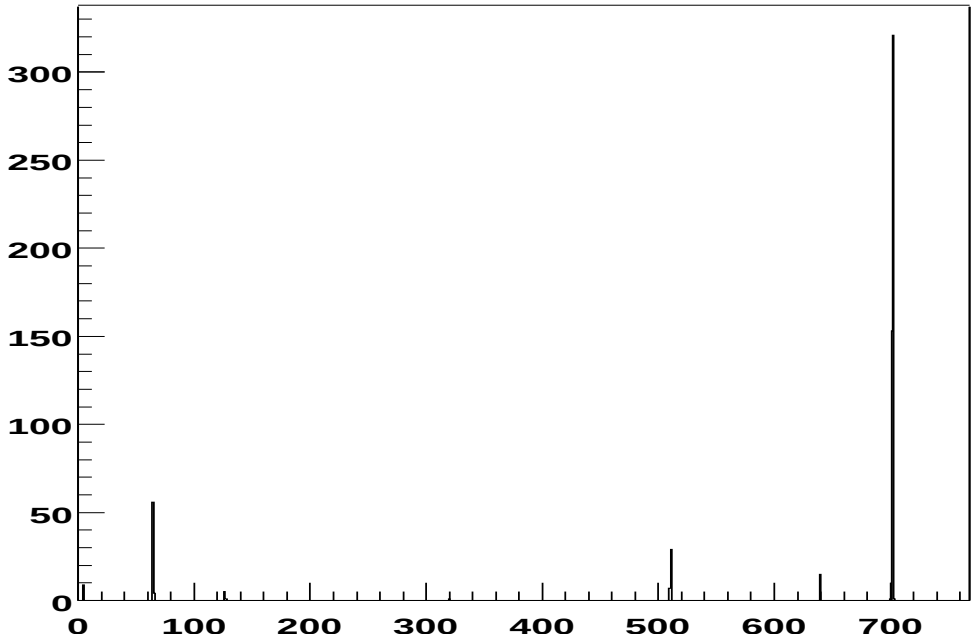

Figure 4.2: *Noise hits at 4 fC threshold; the total number of triggers recorded is 28500.*

The electronics noise has been studied by analyzing a fully equipped MWPC station in the laboratory. The random hits frequency has been measured by reading the front-end data at a trigger frequency of $\sim$ 100 Hz and no chamber high voltage. The typical behavior of one MWPC plane at 4 fC discriminators threshold is shown in fig. 4.2. The total number of random hits/plane for 28500 triggers is 603, corresponding to a noise level $\sim$ 2%. The maximum value of noise/channel is $\sim$ 1%.

4.2.0.4 Detector efficiency measurement

In order to obtain high detection efficiency in stable operation conditions and prevent aging, the high voltage and the thresholds of the readout electronics have to be carefully tuned.

The efficiency of a fully-equipped MWPC plane has been measured in the laboratory using a ^{90}Sr radioactive source. The experimental setup for the measurement, schematically shown in Fig. 4.3, was the following.

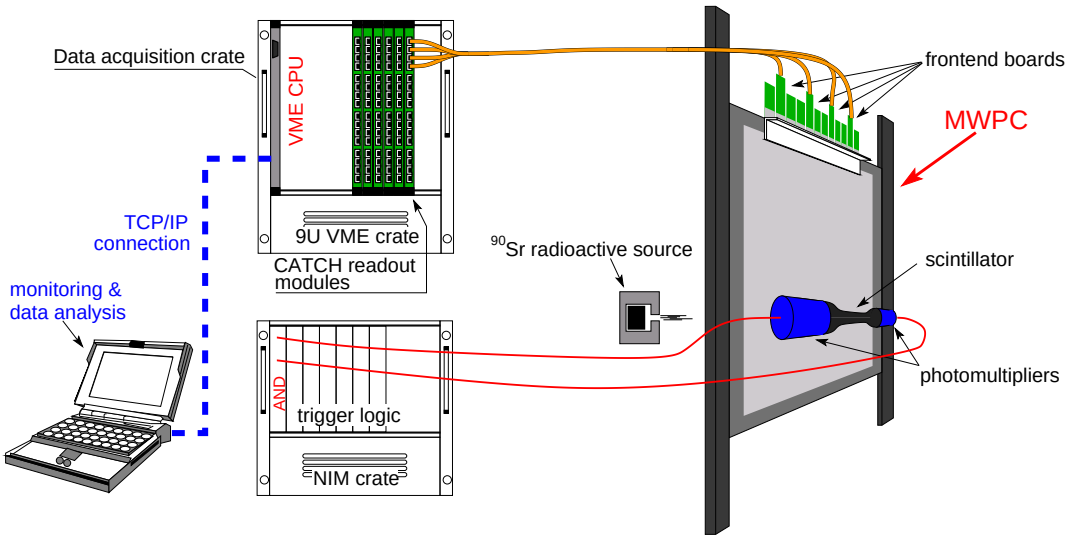

Figure 4.3: *Laboratory setup used for the measurement of the MWPC efficiency. A fully equipped MWPC plane is read out using standard COMPASS CATCH modules. The β^- particles emitted by a collimated ^{90}Sr source are detected by a double coincidence scintillator which provide the trigger signal for the readout system.*

A COMPASS MWPC detector with standard gas mixture has been equipped with four front-end triplets, covering a complete chamber plane. The β^- from the source were detected by the coincidence of two photomultipliers faced to the same small NE110 scintillator on the other side of the chamber. In order to scan the whole MWPC active area, both source and scintillator were mounted on horizontal slides.

Front-end electronics data were read out by a VME-based standalone acquisition system. A 6U version of the CATCH module, with four HOTLink inputs, was used to collect and format front-end electronics data, which were then read from the VME bus. The data were transmitted through TCP/IP to a PC running the monitoring and analysis software.

The plot of fig. 4.4 shows the measured efficiency for three different threshold values of 3, 4 and 5 fC and detector's high voltage from 3.5 kV to 4.4 kV.

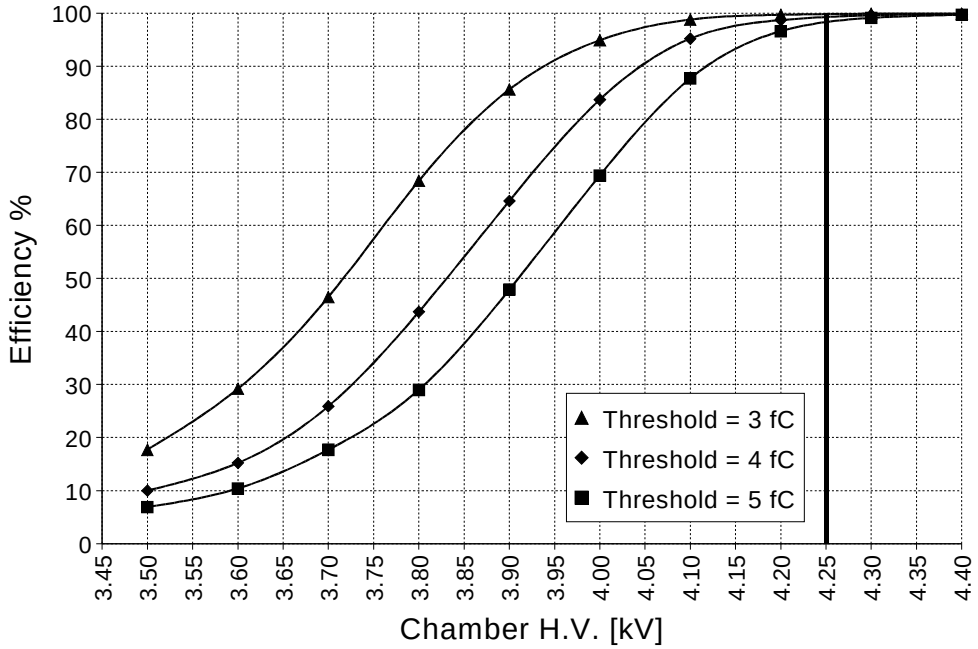

Figure 4.4: *Measured efficiency of a fully equipped MWPC plane for various high voltages and discriminator thresholds.*

Efficiency plateau is reached for all threshold values.

The working point has been chosen at 4.25 kV and 4 fC threshold, corresponding to a measured efficiency slightly less than 99%. The corresponding gas gain is $\sim 4 \cdot 10^4$ and the measured noise level at 4 fC threshold is of the order of 2%, as shown in the previous section.

4.2.0.5 Crosstalk measurement

We have measured the overall crosstalk of an equipped MWPC station by injecting charge signals of ~ 30 fC in a subset of sensitive wires, with a pattern of one fired wire each four, and measured the number of hits recorded with a threshold of 5 fC. The result is shown in fig. 4.5 and features a counting rate for the non-injected channels of the order of 10% at worse. This result should be compared with the measured cluster size distribution of the detector.

Wire clusters are created by grouping together adjacent fired wires and taking the barycenter of the wire group as the cluster position. MWPC detectors

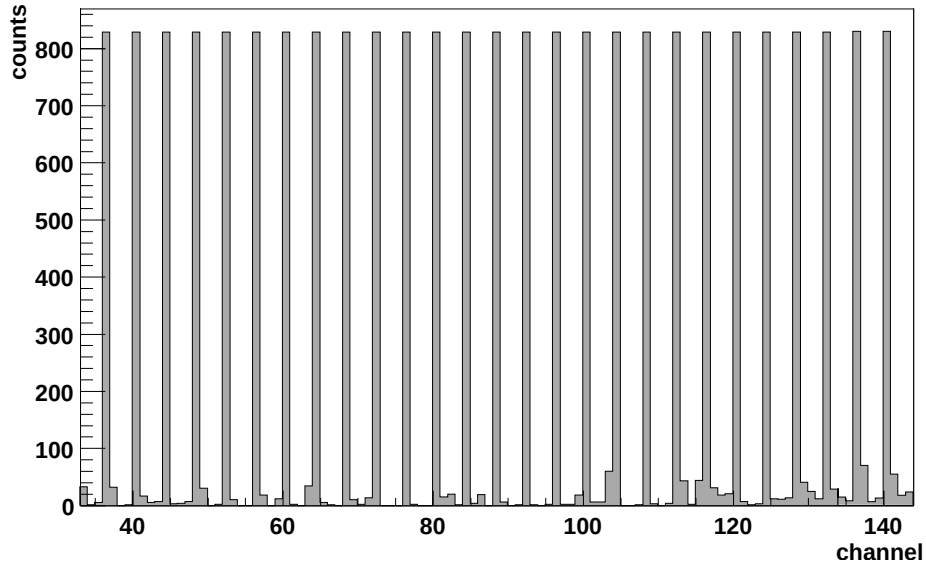

Figure 4.5: *Crosstalk measurement obtained by injecting a 30 fC signal into one channel over four. Electronic threshold is 5 fC.*

are characterized by a significant amount of clusters with more than one hit wire, as shown in fig. 4.6 where a typical cluster size distribution of one MWPC plane is shown. The measured contribution of clusters with more that one hit wire is ~ 30 %. Crosstalk analysis suggests that cluster sizes bigger than one are a consequence of the physics of the detector and therefore are not expected to degradate the achievable spatial resolution. I will discuss this point later in this chapter when I will show residual distributions obtained from low intensity runs.

4.3 Analysis of 2002 data

In this section I present a detailed study of detector performances during 2002 data taking period. Detector efficiency, spatial and time resolution, stability are analyzed using a custom tracking procedure which has the advantage to be fast and to disentangle the results from the overall spectrometer performances by considering MWPC as a standalone tracking system, which is described in

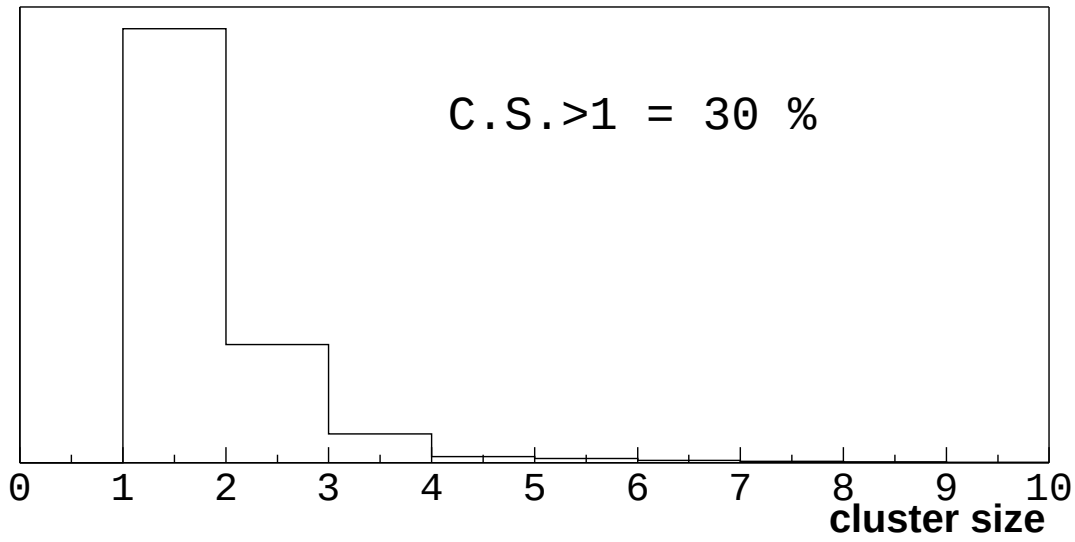

Figure 4.6: *Cluster size distribution for one MWPC plane. The probability of cluster size* > 1 *is around 30%.*

appendix B. The tracking procedure has been used to provide online efficiency measurement during data taking to monitor detector stability.

4.3.1 Efficiency measurement

The custom tracking software developed for MWPC analysis allows easy calculation of detector efficiency for each installed MWPC plane. The apparatus is divided in three zones, one between RICH1 and the second magnet SM2, one between SM2 and the second absorber absorber, and the last behind the second hadron absorber. Tracks in each zone are reconstructed from MWPC hits only and fitted using simple straight lines. Each reconstructed track is extrapolated to all planes in the corresponding zone, and the most probable hit wire is calculated. The plane is considered efficient if a cluster exists with a distance from the expected hit wire smaller that 2 wire pitches. With this method both the wire efficiency and the 2-D efficiency distributions are calculated, as show in Fig. 4.7 and Fig. 4.8.

The fast tracking procedure described has been not only developed for of-

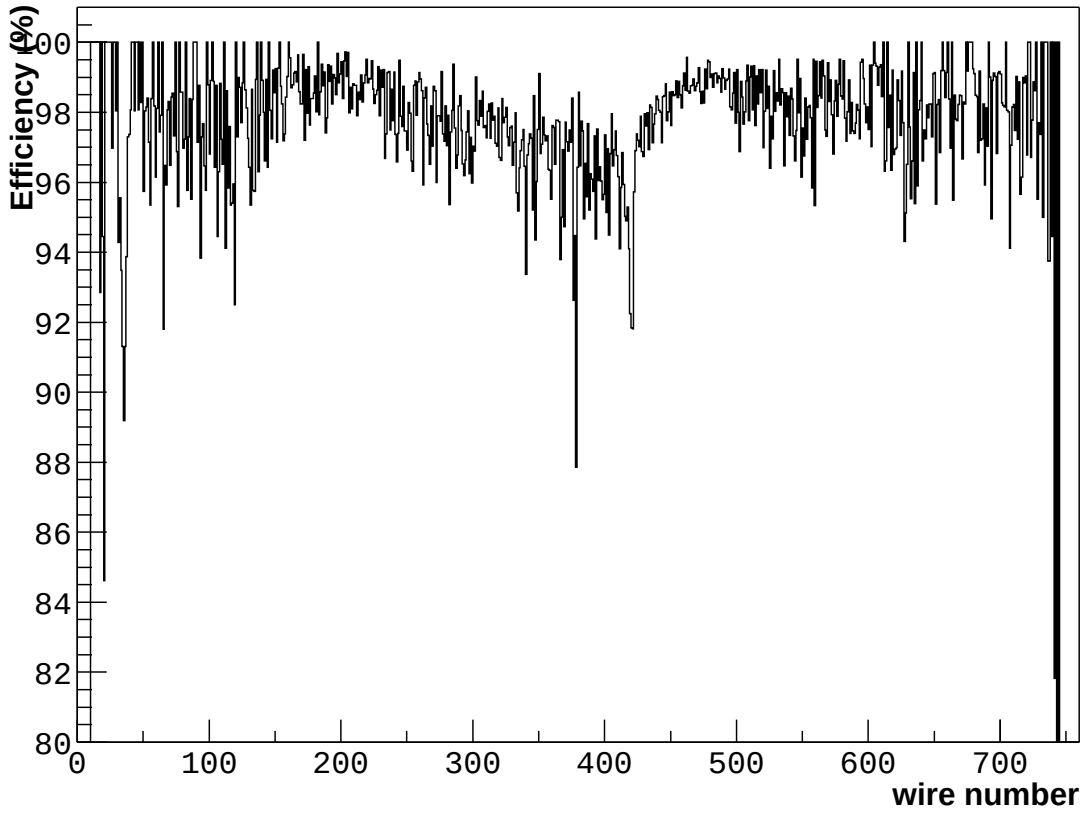

Figure 4.7: *Wire efficiency plot for one MWPC plane. The result of the fit with a constant polynomial is shown on the figure.*

fline analysis of detector characteristics, but also for online track reconstruction and detector efficiency monitoring. The main idea is to use planes efficiencies as a characterizing parameter for monitoring detector performances and stability during the whole data taking period. For this purpose a special tool has been developed to process events from the online data stream delivered by the COMPASS DAQ and to measure wire efficiencies. At the end of each run the overall plane efficiency value is calculated applying a linear fit to the wire efficiency distribution, and the resulting value is stored into a general database for long term availability. A web interface to the database allows to plot the measured efficiency for a given set of planes as a function of the run number, simplifying the data quality check task and allowing a continuous monitoring

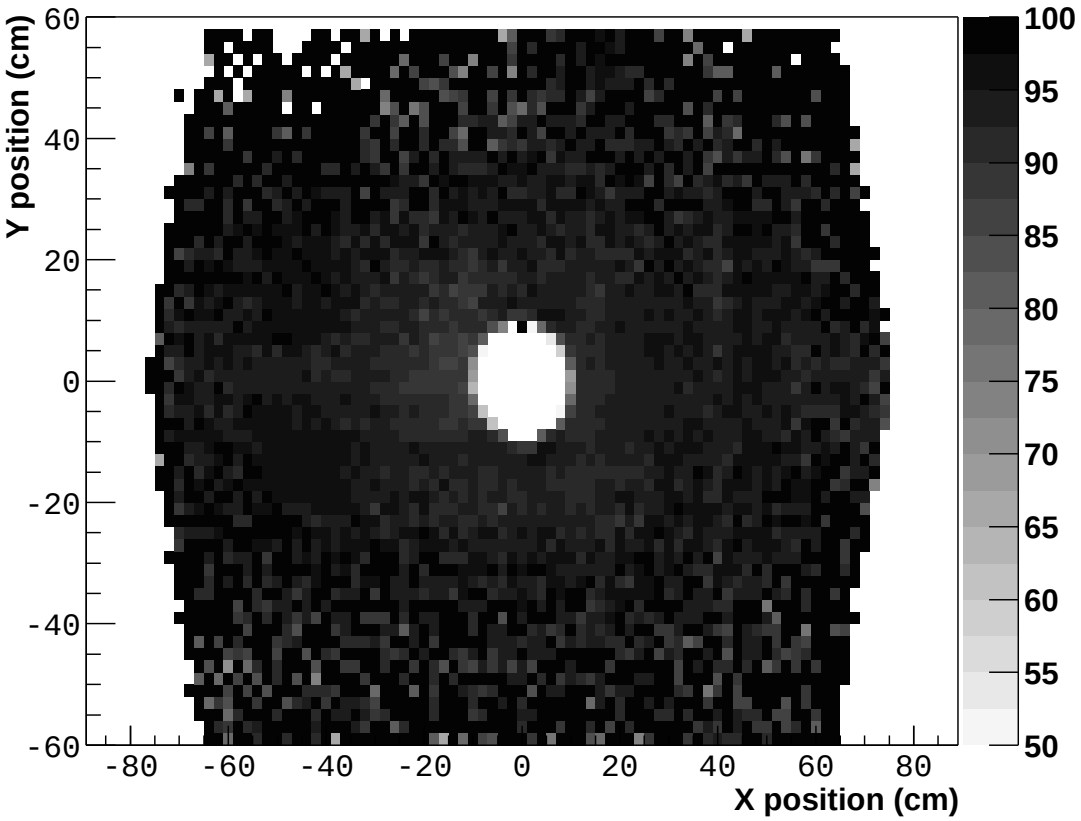

Figure 4.8: *2-D efficiency plot for one MWPC plane. Plane shows very good uniformity; the drop in efficiency due to dead zone is clearly visible in the center of the plot.*

of MWPC stability. An example of such a plot is shown in Fig. 4.9.

4.3.2 Spatial resolution

The spatial resolution of the detector has been evaluated using a sample of data collected with low-intensity beam and magnets off for better track extrapolation. A telescope consisting of 7 GEM planes, with a resolution of $\approx 60\mu$m each, has been used for track reconstruction and fitting. Spatial resolution is measured by plotting the distance between the track extrapolation point and the closest hit cluster.

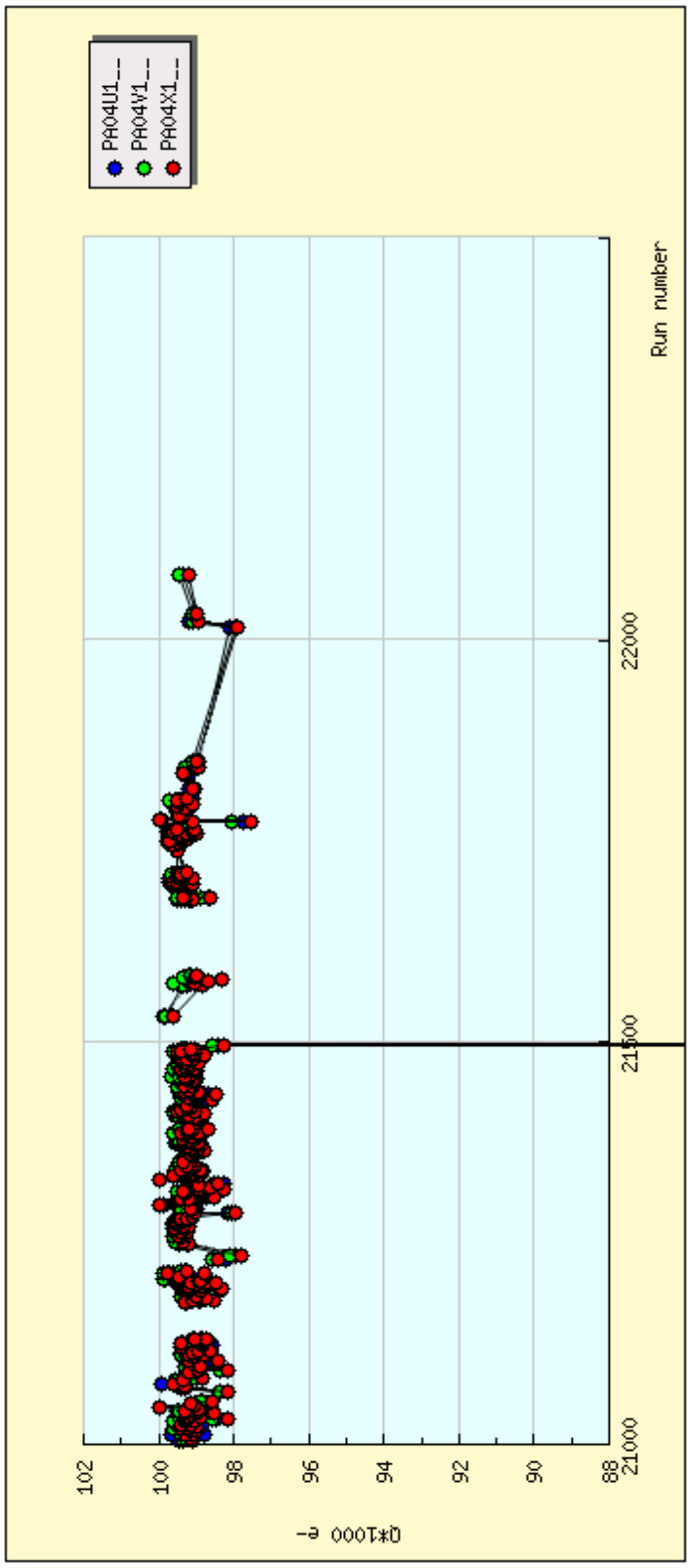

Figure 4.9: *Efficiency as a function of the run number, for one MWPC station. The plot is obtained from the informations stored in the online database.*

The theoretical residual distribution, assuming a uniform efficiency between two sensitive wires, is a rectangular distribution with a width equal to the cell size of the detector (2 mm in our case) and $\sigma = 2/\sqrt{(12)} = 0.6$ mm. In the real world the distribution is smeared by many effects, like crosstalk, track extrapolation, noise, inefficiency. For this reason I have chosen a "smoothed" rectangular function with equation

$$p_0 \left(\frac{1}{\exp^{(p_1-p_2-x)/p_3}+1} + \frac{1}{\exp^{(x-p_1-p_2)/p_3}+1} - 1 \right) + p_4 \qquad (4.1)$$

to fit the measured residual distributions and extract the spatial resolution. In eq. 4.1 p_i are the parameters used in the fit procedure. In particular $2 \cdot p_2$ represents the Full Width Half Maximum (FWHM) of the distribution.

First of all let's consider what happens when no hit clusterization is applied. The fit with our theoretical function leads to a calculated FWHM of ~ 2 mm (see Fig. 4.10). Nevertheless I have already shown that the fraction of multi-hit clusters is significant, and I will demonstrate that clusterization can effectively reduce the width of the residuals distribution. To show this it is convenient to separate the contribution of 1, 2, 3 and 4-hit clusters and analyze each residual distribution independently, as shown in Fig. 4.11. The white plots in the figure represent the distance between the track extrapolation point and each hit of the cluster, the grey ones the distance form the closest hit wire, and black

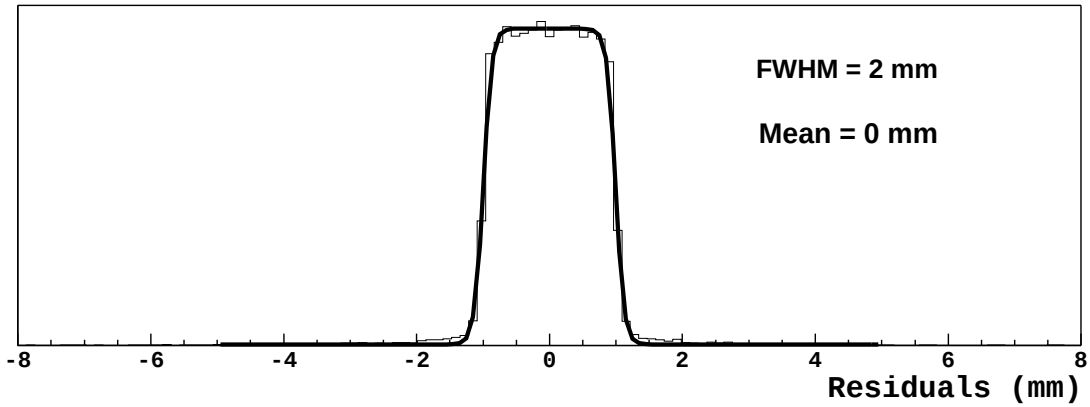

Figure 4.10: *Residual distribution obtained without clusterization of wire hits.*

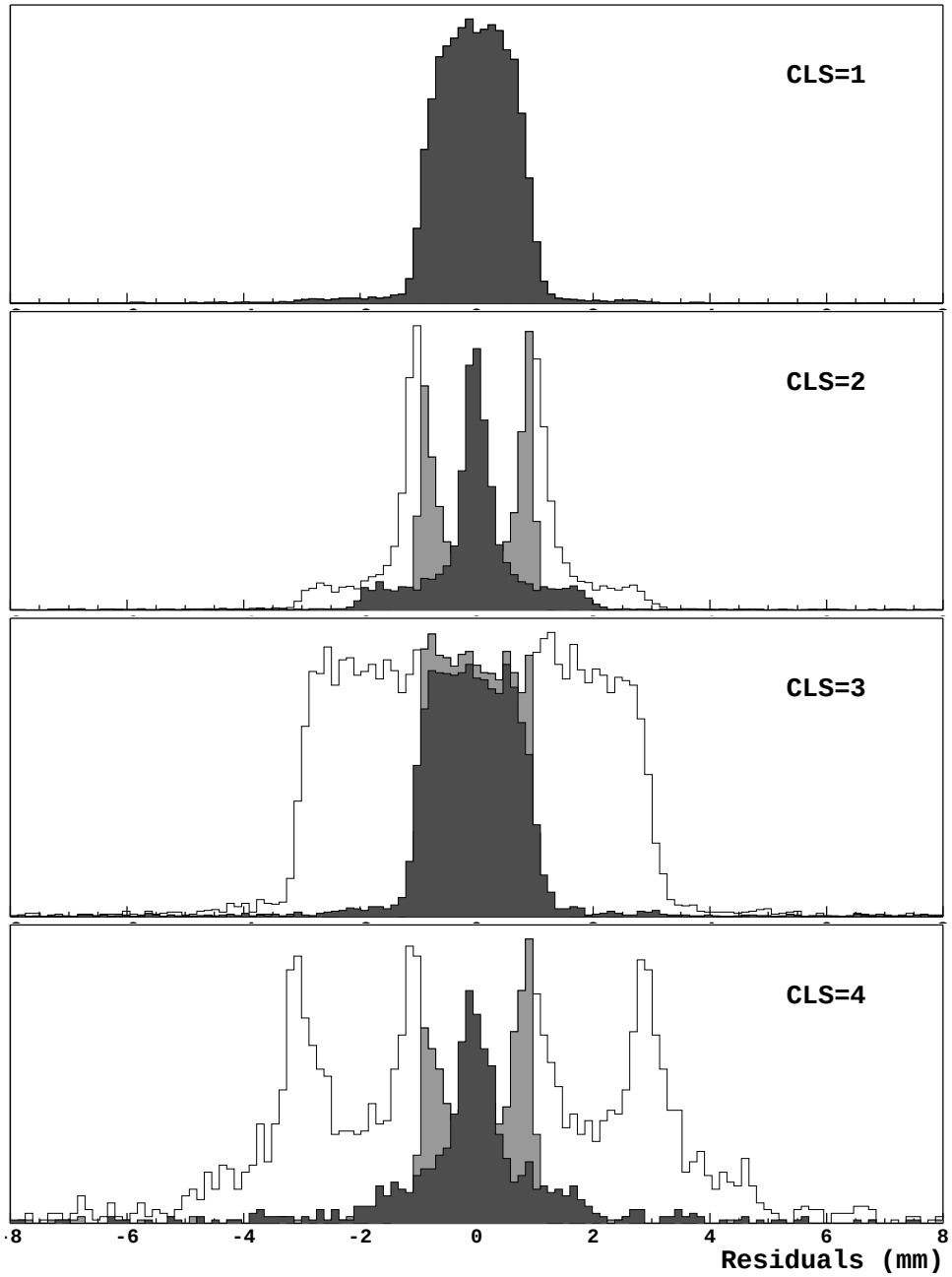

Figure 4.11: *Cluster size dependent residual distributions.*

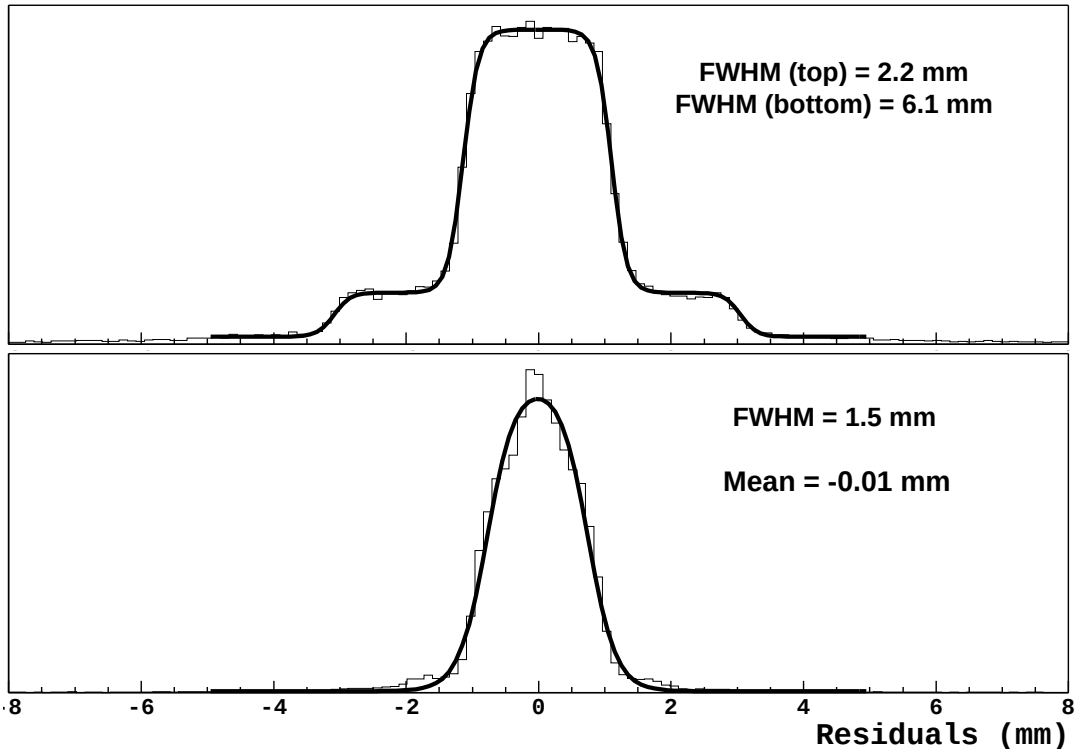

Figure 4.12: *Residual distribution obtained applying a clusterization procedure on the wire hits. The top plot shows the residual distribution for wire hits, the bottom shows the residual distribution of wire clusters. The cluster position is calculated as the barycenter of the wire cluster.*

ones the distance from the cluster barycenter. While there is obviously no difference for single hit clusters, the other plots show a clear enhancement of the spatial resolution when clusterization is applied. Moreover this is a further demonstration that hit clusters are an intrinsic property of the detector and do not originate from crosstalk. The results are summarized in Fig. 4.12 where the overall distributions of hit residuals (top plot) and cluster residuals (bottom plot) are shown. The enhancement in the spatial resolution, if compared to the result of Fig. 4.10, is of the order of 10%.

4.3.3 Hit timing analysis

The wire signal digitized at the frontend level has an associated time stamp which is measured by the TDC chips. The correlation between the hit and the particle crossing time is obtained by subtracting the trigger time provided by the Trigger Control System (TCS), which is common to all the experiment. The hit time spectra is then corrected for the position of the correlation peak, which depends on the distance of the wire plane from the target, i.e. on the particle's time of flight. The resulting distribution represents quite precisely the drift time properties in a multiwire structure.

The signal produced by the MWPC detector has special timing properties which are due to the non-uniform electric field inside the sensitive volume. Most of the wire signals are produced by charge clusters generated in the multiplication region. In this case the drift path of the electrons is short and the response of the detector is fast. A non-negligible fraction of the charge clusters are nevertheless generated in the drift region where the electric field is constant. In this case the drift path is as long as the anode/cathode gap of the detector and the wire signal will appear a certain amount of time later after the passage of

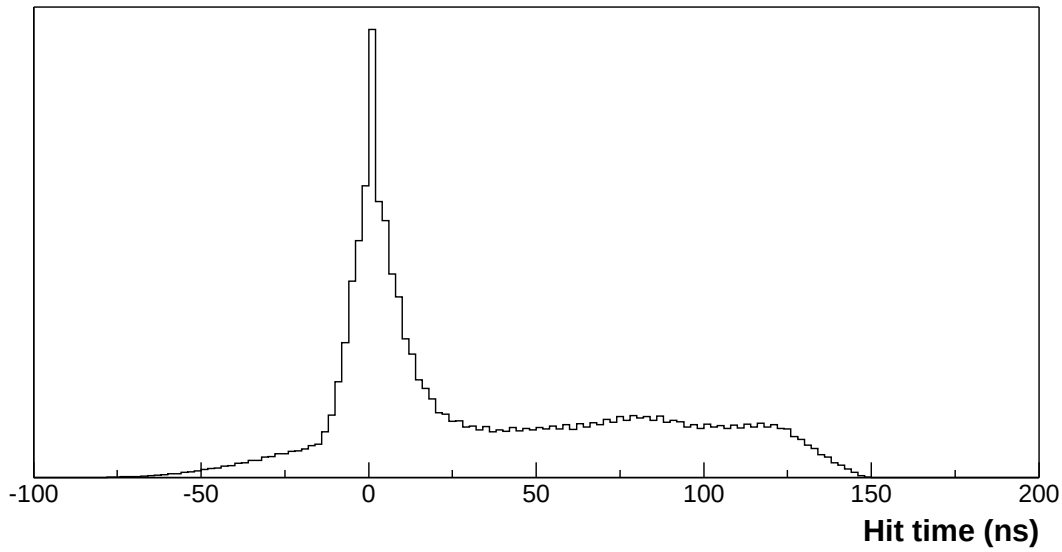

Figure 4.13: *Typical hit time distribution of the COMPASS MWPC detector.*

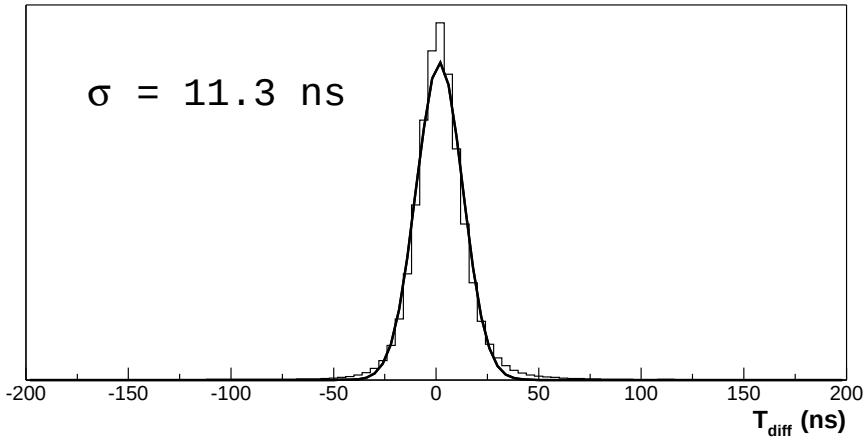

Figure 4.14: *MWPC timing resolution measured using hits along reconstructed tracks.*

the ionizing particle, depending on the gas mixture used and the electric field strength. For this reason the timing spectra of the wire signal are characterized by a peak in the short time region, followed by a tail with a length depending on the geometry of the detector and which defines the maximum time jitter of the signal. In the case of COMPASS MWPC the anode/cathode gap is 8 mm and the drift velocity for the CF_4-based gas mixture used is approximately 10 ns/mm, which leads to a time jitter ≈80 ns. A typical hit time spectrum is shown in fig. 4.13. The length of the tail is consistent with the calculated drift velocity and time jitter.

4.3.3.1 Track time and MWPC timing resolution measurement

When hits belonging to the same track are considered, a certain time correlation between them is expected. In the ideal case, the differences between the time stamps of the hits should give approximately the time of flight of the particle between the two corresponding planes. In the real case those differences are affected by the time jitter of the wire signal, but still this method can be used to estimate the time resolution of the detector. The hit time stamp has first of all to be corrected for the position of the time correlation peak of the corresponding

detector plane. This is somehow equivalent to correcting for the time of flight of the particle, from the target to the plane position. After this correction has been applied, the differences between the corrected time of the hits along a certain track should be centered in zero, and the sigma of the resulting distribution gives the time resolution of the detector. In Fig. 4.14 the measured distribution is shown and fitted with a gaussian distribution; the sigma of the fit is ~ 11 ns and gives the estimation of the achieved time resolution with the COMPASS MWPC. The mean value of the hits time along a certain track can be therefore taken as the "track time", with a precision of ~ 11 ns.

Interesting results can be extracted by considering the timing properties of wire clusters with different sizes. The most simple case to consider are single hit clusters, which are more probably originated by charge clusters generated close to the sensitive wire. In this case the expected drift times are short and most of the hits should contribute to the peak of the time distribution. The hit time distribution for single-wire clusters is shown in Fig. 4.15, before (top) and after (bottom) track time subtraction. From the two plots it is evident that the tail visible in the uncorrected distribution is due to pile-up tracks, i.e. tracks which are not correlated with the trigger and thus lead to wire hits with time stamp far from the time correlation peak.

Hit timing is a good parameter to evaluate the crosstalk contribution to wire clusters. When a wire cluster originates from crosstalk one expects all corresponding hits to have approximately the same time stamps. For example a clear correlation should be visible for 2-wire clusters when plotting the time stamp of one wire versus the other; a significant contribution to the diagonal of the plot would lead to the conclusion that 2-wire clusters are artificially generated by induced charge in the channels close to the fired wire and no correction could be applied to refine the cluster position.

The result obtained from detector data excludes such a hypothesis (see Fig. 4.16) and confirms the small crosstalk contribution measured in the laboratory. The analysis of 3-wire clusters lead to similar conclusions. In this case

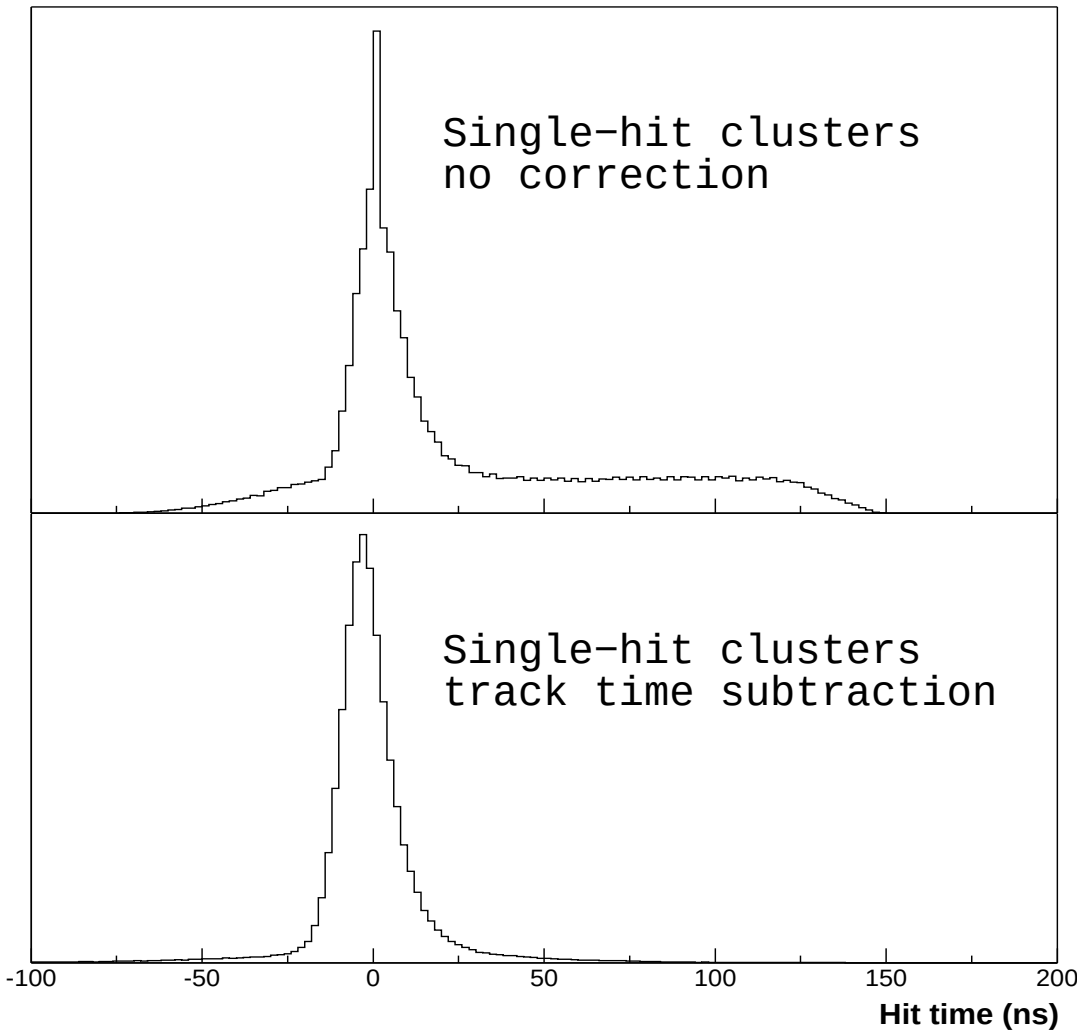

Figure 4.15: *Single-hit clusters timing, before (top) and after (bottom) track time subtraction.*

the expected time pattern is a central hit with short drift time and two side hits belonging to the tail of the timing distribution. The results are summarized in Fig. 4.17. The two plots in the figure show the hit time correlation between central and side hits (left) and the two side hits (right) which is in agreement with the expected result.

4.3.3.2 Time-based cluster rejection

The analysis of MWPC hit timing properties performed so far suggests the possibility of rejecting clusters not correlated with the trigger. Cluster selection can facilitate and speed-up the tracking procedure by reducing the total number of clusters involved, but care must be taken over the rejection criteria. I will show in this paragraph that a simple criteria based on hit time and not taking into account the hit cluster composition will lead to a reduction in the spatial

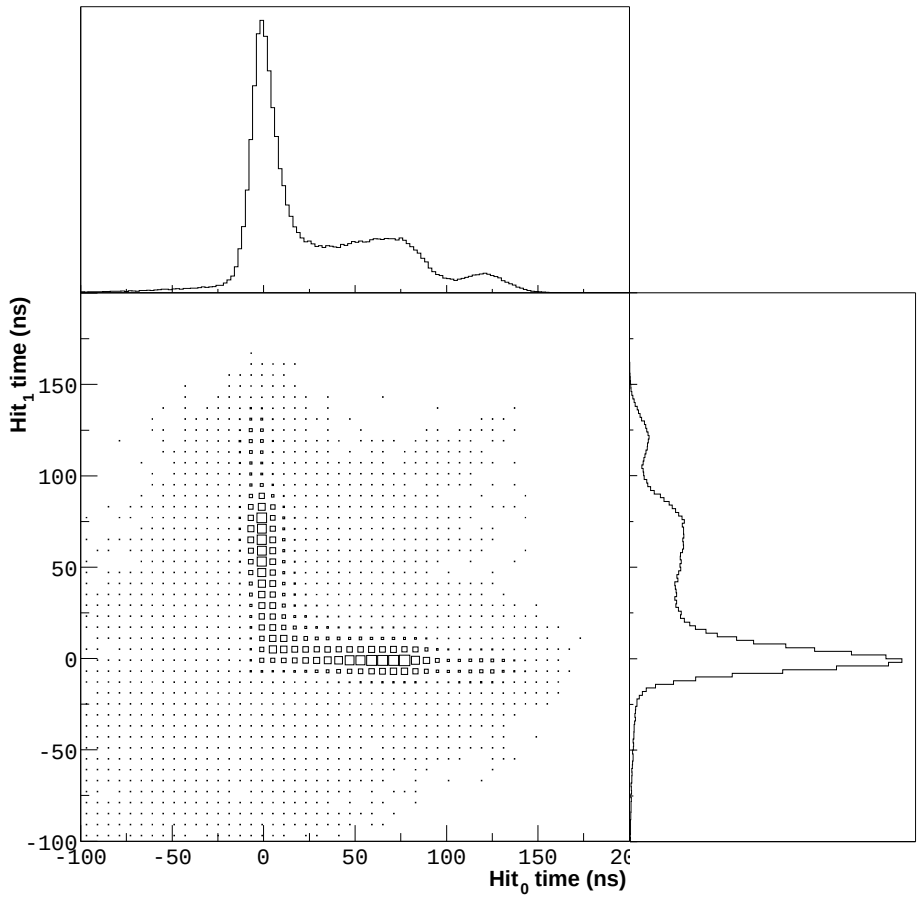

Figure 4.16: *Timing properties of double-hit clusters. The plot shows the timing correlation between the two hits of the cluster, and their separate time distributions. Double hits due to cross-talk effects are expected to contribute to the diagonal of the correlation plot.*

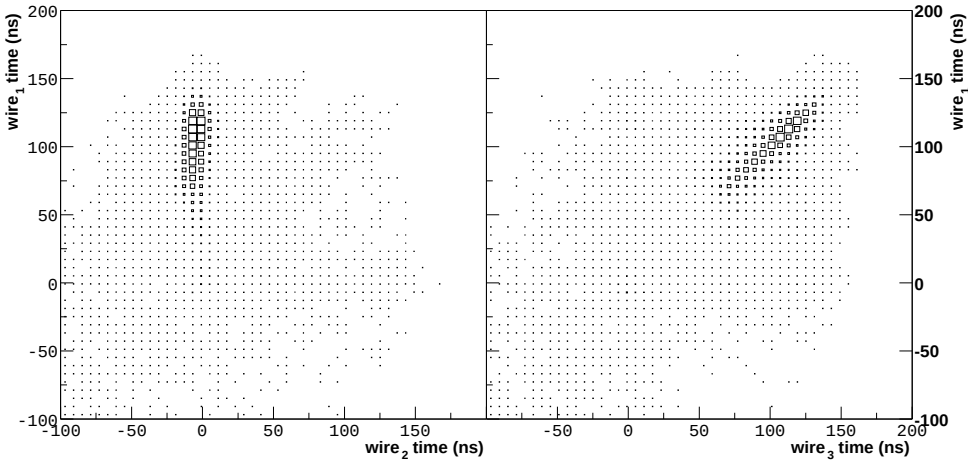

Figure 4.17: *Timing properties of three-hit clusters. The plots show the timing correlation between the central hit and one of the side hits (left plot), and between the two side hits (right plot).*

resolution of the order of 25%.

In order to show the effect of time-based clusters rejection in standard data tacking conditions, I have measured the residual distributions for an high intensity run, using a GEM telescope formed by 3 GEM stations located after SM2 magnet. The reason why it is not possible in this case to use the complete GEM telescope described in Sec. 4.3.2 is the magnetic field of SM2, which does not allow simple straight line tracking. The results are anyway compatible with the other measurements, as shown in Fig. 4.18. The typical mean cluster multiplicity when no time cut is applied is ~ 3.

The simplest selection criteria is to put a strict window around the hit time correlation peak. Unfortunately this leads to a deterioration of the spatial resolution, which is of the order of 35% when $-12 < t_h < 25$ ns is required, where t_h represents the hit time stamp (see Fig. 4.19). The applied cut has the effect of destroying the information about real cluster size, since many hits belonging to multiwire-clusters are rejected and the corresponding clusters are transformed into single hits.

A much better criteria is to first of all define a cluster time as the smallest

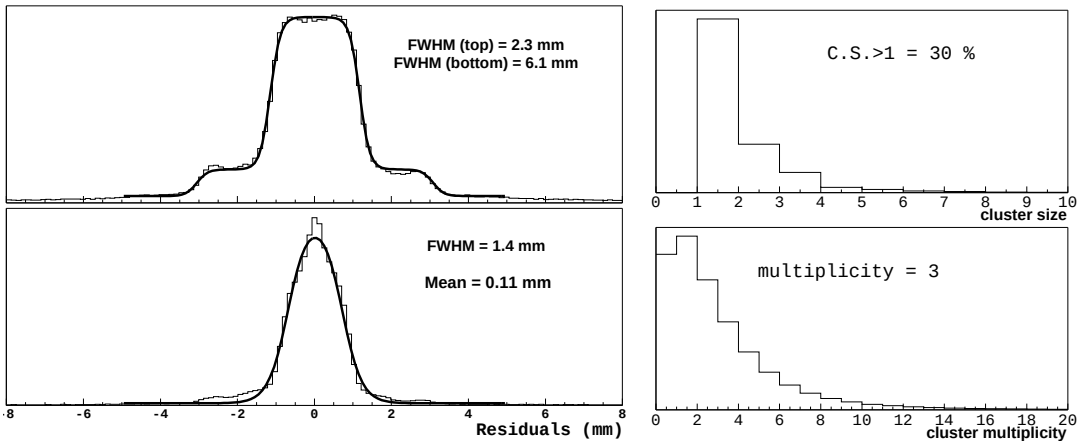

Figure 4.18: *Clusters residual, clusters size and clusters multiplicity distributions obtained form a standard, high-intensity run, without any time cut.*

hit time in the cluster, and then apply the time cut on it. The result of a requirement of $-12 < t_c < 25$ ns, where t_c represents the cluster time, is shown in Fig. 4.20. The spatial resolution is in this case compatible with the normal result of Fig. 4.18, while the cluster multiplicity is similar to the one of Fig. 4.19.

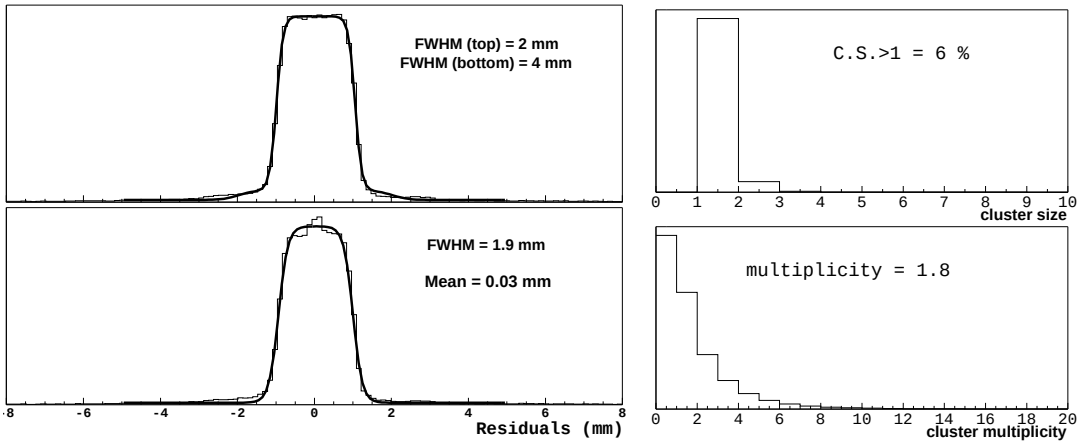

Figure 4.19: *Clusters residual, clusters size and clusters multiplicity distributions obtained applying a* $-12 < t_h < 25$ *ns cut on the hit time.*

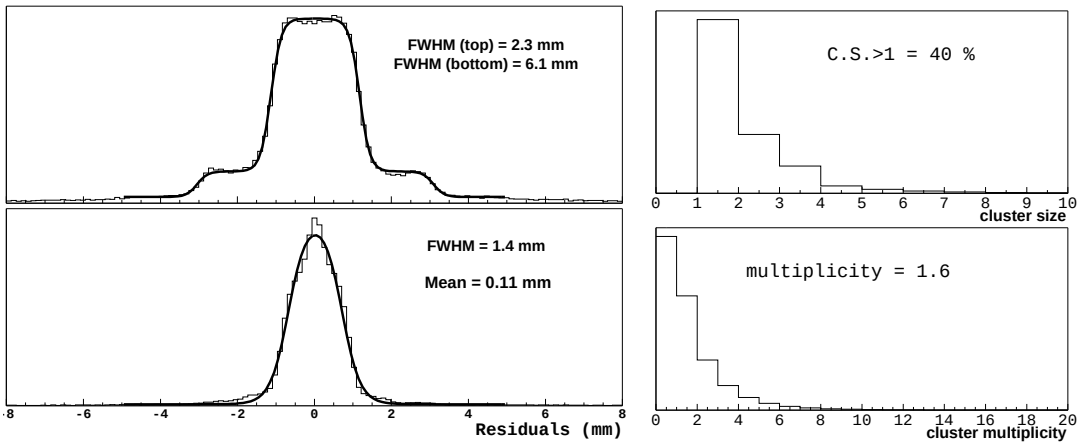

Figure 4.20: *Clusters residual, clusters size and clusters multiplicity distributions obtained applying a* $-12 < t_c < 25$ *ns cut on the cluster time.*

Chapter 5

Analysis of 2002 data set with transverse target spin

During summer 2002 a data taking period has been devoted to the study of DIS with transverse target polarization. In the middle of the period the spin direction of the two target cells has been reversed, and two similar sets of runs have been recorded, one for each target spin configuration, for a total of 216 good runs. The two data sets are denoted, following the COMPASS convention, as **P2B** and **P2C**. The target spin configurations for the two data sets are shown in Fig. 5.1.

In this chapter the preliminary results on the analysis of the analyzing power of the Λ^0 production in polarized SIDIS with a transversely polarized target are presented. The conventions used in the chapter for the orientation of the reference system are the following: the z axis coincides with the beam direction at the target, the y axis is directed vertically, from bottom to top, and the x axis is defined so that it forms a right-handed system with the other two axes.

5.1 The analyzing power

The dependence of the Λ production cross-section on the target spin orientation can be measured from the single-spin asymmetry

$$A_Y = \frac{d\sigma^{S_T=\uparrow} - d\sigma^{S_T=\downarrow}}{d\sigma^{S_T=\uparrow} + d\sigma^{S_T=\downarrow}}, \tag{5.1}$$

where $S_T = \uparrow (\downarrow)$ denotes target spin directed along (opposite) to the dipole magnetic field. The corresponding experimental asymmetry is given by

$$A_Y^{EXP} = \frac{1}{f \cdot P_T} \left(\frac{N^{P_T=\uparrow} - N^{P_T=\downarrow}}{N^{P_T=\uparrow} + N^{P_T=\downarrow}} \right), \tag{5.2}$$

where $P_T = \uparrow (\downarrow)$ denotes the target *polarization* direction, P_T is the mean polarization value and f is the target dilution factor, which is assumed to be

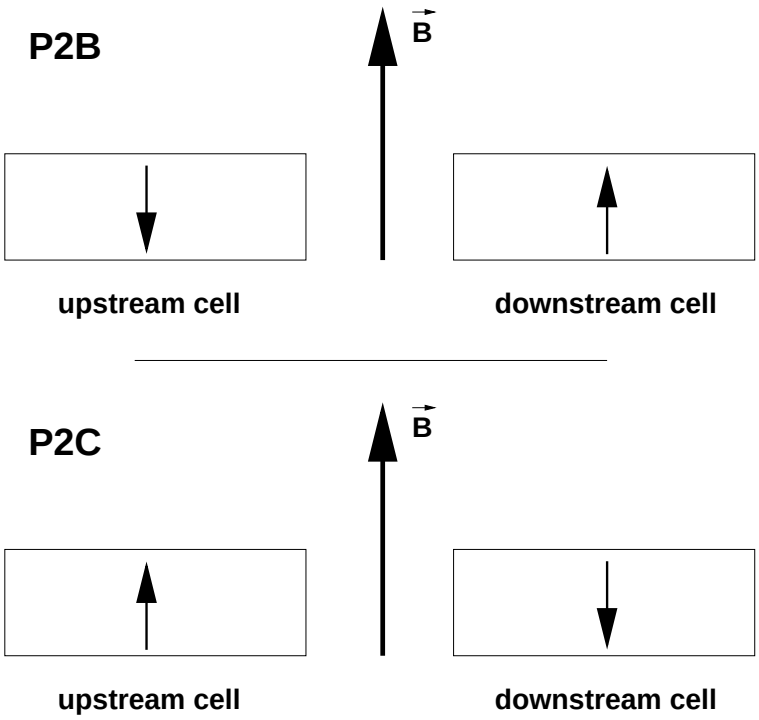

Figure 5.1: *Configurations of the target cells polarizations for the P2B (top) and P2C (bottom) data sets. The $\vec{B}$ arrow represents the target dipole magnetic field direction.*

0.5 for the ^{6}LiD target.

5.2 Useful symmetries

The A_Y measurement involves the comparison of Λ production yields with opposite target polarizations. Moreover, the two measurements $N^{P_T=\uparrow}$ and $N^{P_T=\downarrow}$ have to be referred to the same incoming particle flux, so that the denominator of eq. 5.2 is proportional to the unpolarized cross-section. The normalization to the incident particle flux is straightforwardly obtained if the measurement is performed at the same time on two target cells with opposite polarizations. In this case the particle flux can be considered equal for the two cells, but other problems arise.

In the COMPASS case the angular acceptance of the polarized target is not equal for the two cells, as shown in Fig. 5.2. For this reason, a comparison of the production yields from the two target cells is strongly affected by false asymmetries arising from differences in the apparatus acceptance. A way to eliminate this false asymmetry is to perform two measurements with opposite target cells spin configurations, and then to mediate the two independent results. A detailed description of this correction is given in appendix C.

The rotation invariance properties of the SIDIS process can be used to correct for the apparatus acceptance even in the case of a single measurement. The Λ production process, in the hypothesis of photon exchange, involves electromagnetic and strong interactions which are invariant under a π rad rotation along the beam axis. For this reason a Λ produced with momentum components p_x^Λ and p_y^Λ from a target cell polarized upward is equivalent to a Λ with momentum components $-p_x^\Lambda$ and $-p_y^\Lambda$ coming from a downward-polarized target cell (see Fig. 5.3). Provided that the apparatus acceptance is symmetric with respect to the plane defined by the y and z axes, the left and right-produced samples play a role analogous to the opposite target cell orientations.

For the same reason the left and right samples have to be evaluated sepa-

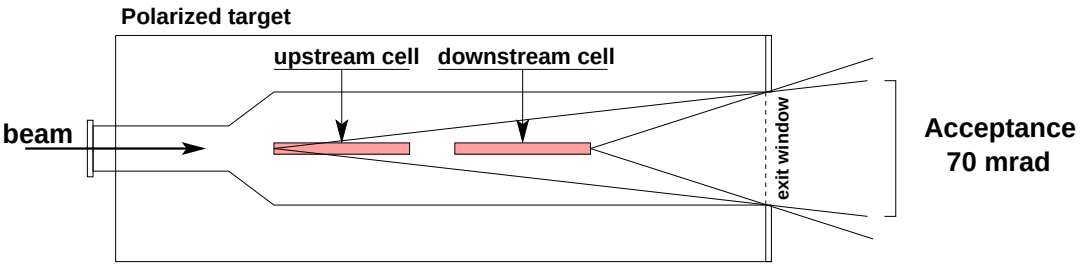

Figure 5.2: *The apparatus acceptance for the two cells of the polarized target is constrained by the size of the target exit window. The minimum acceptance is 70 mrad.*

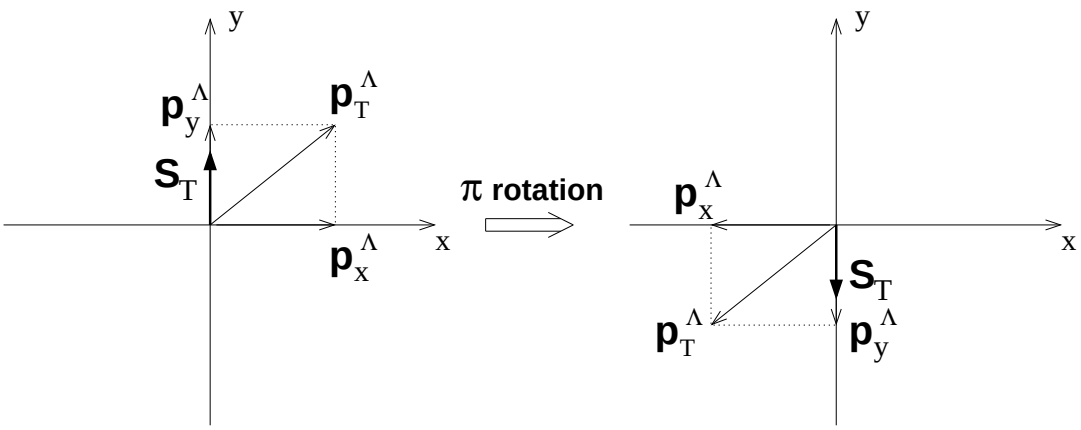

Figure 5.3: *Invariance of the Λ production cross-section for a rotation of π radians around the beam axis. S_T is the direction of the target spin, p_T^Λ is the Λ transverse momentum, and p_x^Λ and p_y^Λ are the x and y components of the Λ momentum.*

rately. We therefore define a *Left* A_Y and a *Right* A_Y as

$$A_Y^{L(R)} = \frac{1}{f \cdot |P_T|} \left(\frac{N_{L(R)}^{P_T=\uparrow} - N_{L(R)}^{P_T=\downarrow}}{N_{L(R)}^{P_T=\uparrow} + N_{L(R)}^{P_T=\downarrow}} \right). \tag{5.3}$$

The rotational invariance of the Λ production cross-section allows to calculate the A_Y from the measurement of a single cell. In fact we can write the following equivalences

$$A_Y^L = \frac{1}{f \cdot |P_T|} \left(\frac{N_L^{P_T=\uparrow} - N_L^{P_T=\downarrow}}{N_L^{P_T=\uparrow} + N_L^{P_T=\downarrow}} \right) \equiv \frac{1}{f \cdot |P_T|} \left(\frac{N_L^{P_T=\uparrow} - N_R^{P_T=\uparrow}}{N_L^{P_T=\uparrow} + N_R^{P_T=\uparrow}} \right) = A_Y^{\uparrow} \tag{5.4}$$

$$A_Y^R = \frac{1}{f \cdot |P_T|} \left(\frac{N_R^{P_T=\uparrow} - N_R^{P_T=\downarrow}}{N_R^{P_T=\uparrow} + N_R^{P_T=\downarrow}} \right) \equiv \frac{1}{f \cdot |P_T|} \left(\frac{N_L^{P_T=\downarrow} - N_R^{P_T=\downarrow}}{N_L^{P_T=\downarrow} + N_R^{P_T=\downarrow}} \right) = A_Y^{\downarrow}, \tag{5.5}$$

where $A_Y^{\uparrow(\downarrow)}$ represents the left/right asymmetry for the target cell with the spin oriented parallel (anti-parallel) to the dipole magnetic field. One of the advantages of this alternative approach is that the differences $N_L^{P_T=\uparrow} - N_R^{P_T=\uparrow}$ and $N_L^{P_T=\downarrow} - N_R^{P_T=\downarrow}$ are calculated for the same target cell, and thus refer to the same beam flux and polarization value.

5.3 MonteCarlo simulations

The behavior of the COMPASS apparatus with respect to Λ hyperons reconstruction has been studied using the available MonteCarlo tools. Different sets of MonteCarlo simulations have been done in order to investigate various aspects of the experimental apparatus and of the Λ reconstruction efficiency.

One of the key points of the transverse target spin configuration is the presence of a 0.5 Tesla dipole magnetic field in the polarized target. The field is directed along the y axis, perpendicular to the direction of the muon beam. The dipole field has the effect of bending the beam by an angle which is 3 mrad in average. To account for this deviation, the beam line has to be adjusted in such a way that the beam enters the polarized target with an angle, so that in average the beam muons are directed along the z axis at the target center.

The dipole field deviates the scattered muons and the charged particles produced in the DIS as well. An asymmetry with respect to the beam axis is therefore expected, since the dipole field deviates the charged particles systematically in the same direction. The effect on the scattered muons is expected to be small, at least for small Q^2 values. On the contrary the effect can be significant for low-momenta hadrons, which can be stopped by the outer structure of the polarized target.

The Λ hyperons are detected from the $\Lambda \rightarrow p\pi^-$ decay products. The momentum of the decay pion strongly depends on the angular distribution of the decay process: pions emitted collinear to the Λ flight path and backward in the Λ center of mass frame can have very low momenta, and many out of them do not pass through the target exit window. Moreover, π^- are systematically deviated on the left with respect to the beam axis, so that a left/right asymmetry on the Λ reconstruction efficiency is expected.

The situation is different in the case of longitudinal target polarization. The solenoid field, although intense (~ 2 Tesla), is with good approximation directed along the beam axis, and almost collinear with all the charged particles created in the interaction with the target. For this reason the deviation due to the solenoid field is small, and symmetric with respect to the beam axis.

In order to investigate the importance of these effects, some MonteCarlo simulations have been performed both with the longitudinal configuration and with the transversal one.

The Λ events have been produced using the Lepto DIS generator. To increase the Λ statistics the data set has been "artificially enriched" by keeping only events with at least one Λ hyperon in the final state. This includes both directly produced and secondary Λ. The simulated DIS process does not include polarization effects and allows the study of experimental apparatus contributions to the measured spin observables. The number of generated events is 10^6, out of which $6 \cdot 10^3$ have been reconstructed, with an overall efficiency of 6%.

The generated events have been propagated through the experimental apparatus using the COMGEANT package, based on GEANT 3.21[34] and con-

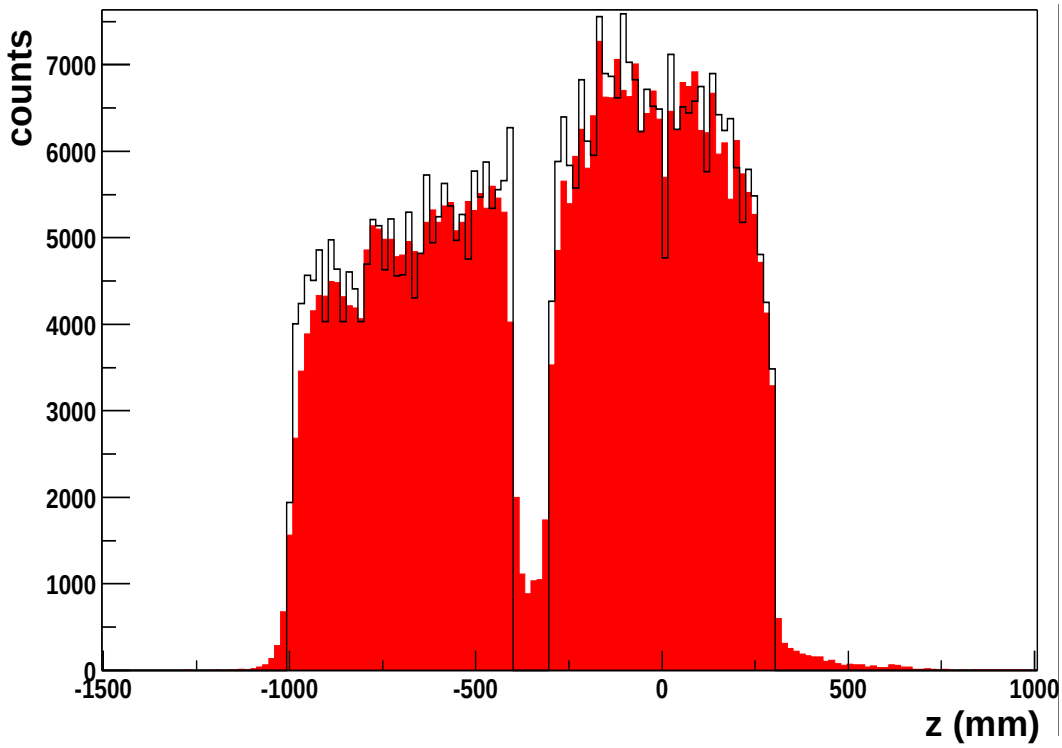

Figure 5.4: *Generated and reconstructed primary vertex z distribution in the MonteCarlo analysis with transverse spin configuration. The filled area corresponds to the reconstructed vertices.*

taining the description of all the existing COMPASS spectrometer elements (trackers, target, magnets, hadron absorbers, RICH1 and calorimeters) available in 2002. The last step of the simulation chain has been the processing with the COMPASS reconstruction package, named CORAL [35]. The result is a file containing all the informations about the generated and reconstructed vertices and tracks, which are the inputs of the analysis code. In Fig. 5.4 the distribution of the z coordinate for reconstructed (filled area) and generated primary vertices is shown.

5.4 Λ vertex selection

In our analysis Λ particles are identified from their weak decay $\Lambda \rightarrow p\pi^-$, which results in a "$V^0$"-like vertex. The incoming neutral particle is not detected, and appears only when it decays in two particles with opposite charges, which are deviated in opposite direction by the spectrometer magnets.

The sample of events used in the analysis is obtained by requiring the presence of a completely reconstructed primary vertex (beam muon and scattered muon with associated momenta), plus at least one secondary V^0 vertex. Such sample contains a small fraction of Λ vertices, and some additional cuts are required in order to reject the background sources and clean the Λ signal.

The Λ hyperons are not the only neutral particles decaying with a V^0 vertex, and not the most probable. K^0_S mesons have a larger production cross-section, and decay in $K^0_S \rightarrow \pi^+\pi^-$ with a branching ratio of $\sim 68\%$. K^0_S mesons, if not indentified and rejected, contribute to the background of the Λ invariant mass distribution. The most effective way to discriminate between K^0_S and Λ decays would be to identify the positive decay particle using RICH information on the particle mass. Unfortunately during the transversity data taking period the RICH information was not available due to an accident which provoked the contamination of the radiator gas.

K^0_S and Λ can also be separated using their different lifetimes. The $c\tau$ constant is 2.6762 cm for K^0_S and 7.89 cm for Λ, and the distribution of the distance between the production and decay vertices is different in the two cases. In our analysis a cut of 40 cm minimum has been applied.

Other V^0 vertices are originated by e^+e^- pairs from photon conversion. The two electrons have in this case a small transverse momentum, and the sum of their momenta has a small polar angle. This events can be effectively rejected with a cut of $p_T > 20$ MeV/c on the positive particle momentum.

Some other vertices are rejected by applying a cut of $\theta > 0.01$ rad on the positive particle polar angle. Those vertices, if not rejected, would lead to reconstructed lambdas with too high momentum.

Another source of background is the presence of fake V^0 vertices. The

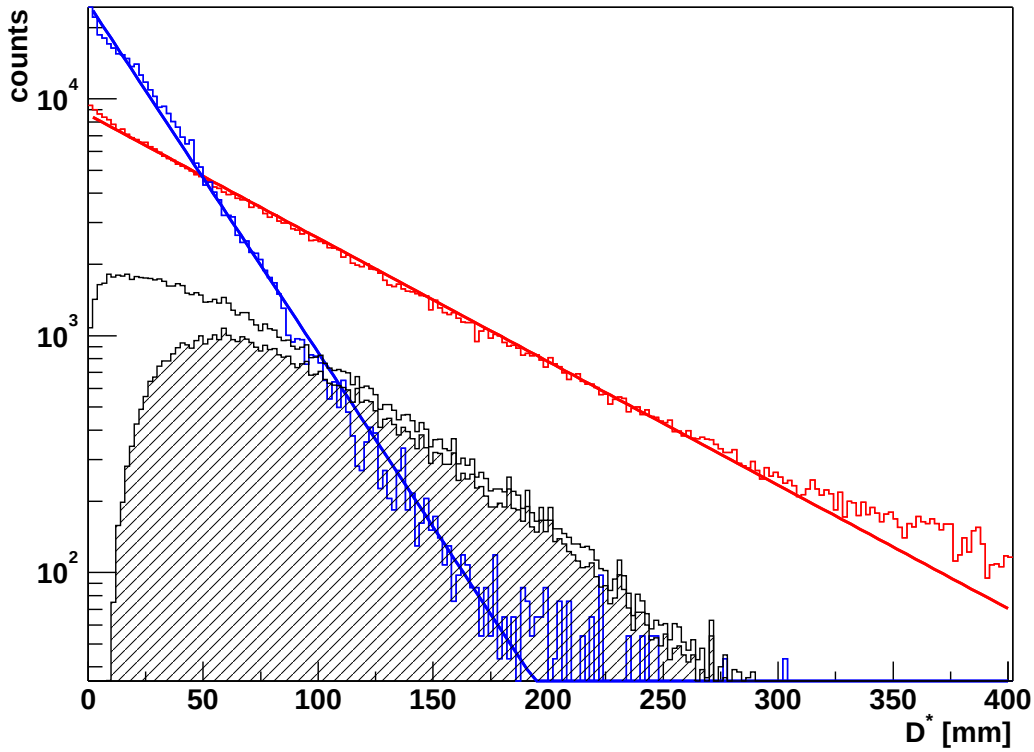

Figure 5.5: *Distance between primary and secondary vertices, for generated kaons, generated lambdas, reconstructed lambdas and accepted lambdas after all the applied cuts. On the horizontal axis it is reported the $D^* = D/\gamma$, where D is the distance between the primary and secondary vertices and $\gamma = 1/\sqrt{1-\beta^2}$ is the relativistic γ of the decaying particle.*

vertex reconstruction package of the COMPASS event reconstruction program does not apply a selection on fitted vertices: any combination of tracks which leads to fitted vertex with good χ^2 is kept. However, only some combinations correspond to real vertices, while many of them are only due to combinatorial background. The rejection of fake vertices is mainly based on the request that the reconstructed neutral particle points to the primary vertex. This is done by calculating the angle between the particle direction and the line connecting the two vertices. Events are accepted only if the cosine of this angle is higher than 0.9999. All vertices surviving the cuts are then selected on a χ^2 basis.

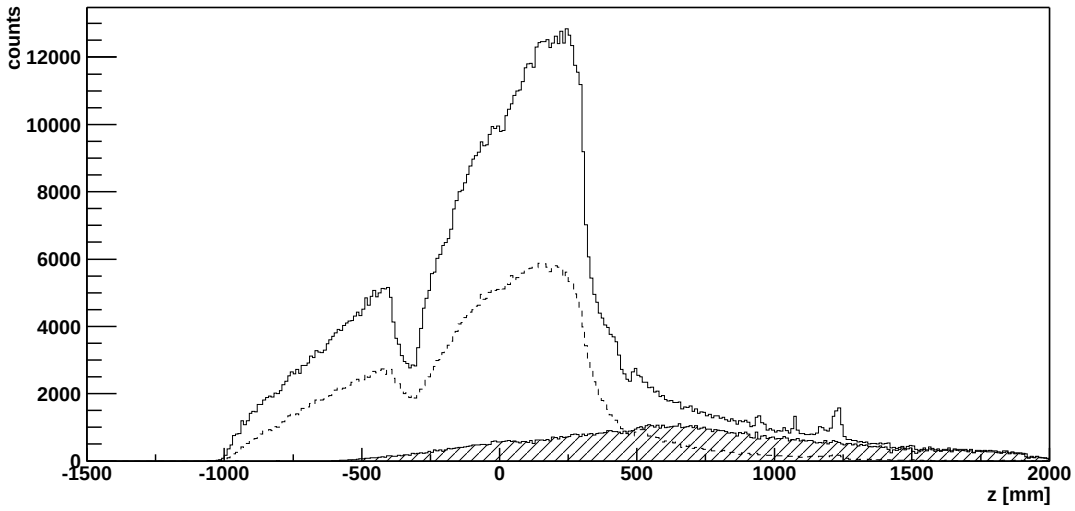

Figure 5.6: *Reconstructed secondary vertex z distribution in the MonteCarlo analysis with transverse spin configuration. The solid line corresponds to all the reconstructed V^0 vertices, the dashed line corresponds to fake vertices, and the hatched area to accepted vertices after Λ selection cuts.*

The Λ vertex selection criteria have been checked in the MonteCarlo simulations to get numerical estimates of the rejection efficiencies. In Fig. 5.6 the distribution of the z coordinate for all the reconstructed V^0 vertices in the MonteCarlo analysis is shown. The MonteCarlo information allows to discriminate between "real" and "fake" secondary vertices, and to evaluate the contamination due to combinatorial background. Reconstructed vertices which cannot be associated to the generated ones are considered fake and correspond to the dashed plot in Fig. 5.6, while the solid line corresponds to all the reconstructed vertices and the hatched area to the vertices selected by the described cuts. The effect of all the cuts is to suppress 86% of the reconstructed V^0 vertices, but only 58% of the "good" vertices, i.e. those corresponding to generated particles. On the contrary, 97% of the fake vertices are rejected. The same criteria, validated with the MonteCarlo analysis, have been applied to real data.

The overall Λ invariant mass distribution for the two samples available for the analysis is shown in Fig. 5.7. The distribution has been fitted with a gaus-

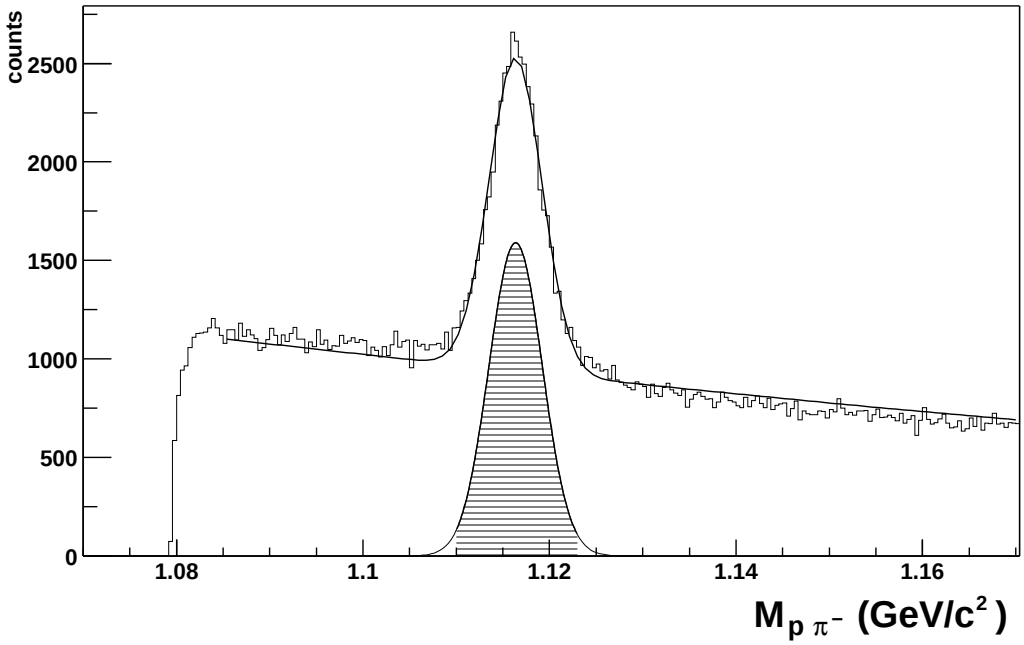

Figure 5.7: *Invariant mass distribution of the selected V^0 vertices, in the hypothesis of $\Lambda \rightarrow p\pi^-$ decay. The distribution, obtained by summing both P2B and P2C data sets, has been fitted with a gaussian curve plus a 3rd degree polynomial background. The estimated number of Λ, corresponding to the hatched area in the plot, is ~ 26000.*

sian curve plus a 3rd degree polynomial for the background. The number of Λ hyperons resulting after background subtraction is ~ 26000. In Fig. 5.8 the Armenteros plot for the same statistics is shown. The plot is a graphical representation of the neutral particle decay kinematics, and allows to distinguish Λ, $\bar{\Lambda}$ and K_0 particles according to the value of the Armenteros variable α, defined as

$$\alpha = \frac{p_L^{h^+} - p_L^{h^-}}{p_L^{h^+} + p_L^{h^-}}, \tag{5.6}$$

where $p_L^{h^{+(-)}}$ is the component of the positive (negative) decay particle momentum along the direction of the neutral decaying particle. When the transverse momentum of the positive decay hadron $p_T^{h^+}$ is plotted against α, the signature

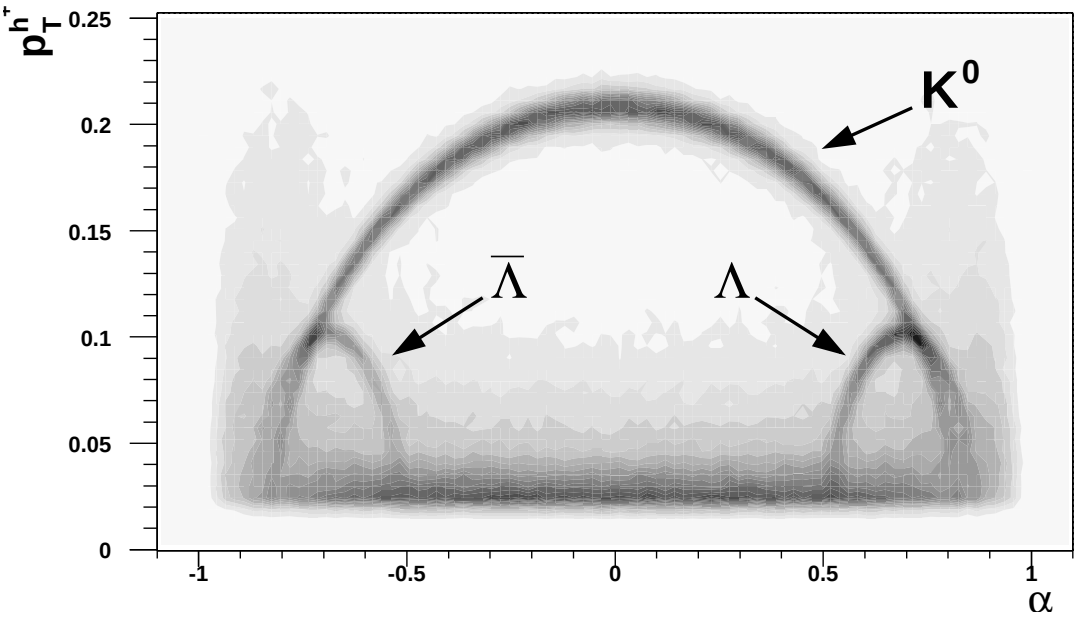

Figure 5.8: *Armenteros plot. The K^0, Λ and $\bar{\Lambda}$ decays are represented by semi-ellipses in the $(p_T^{h^+}, \alpha)$ plane, where $p_T^{h^+}$ is the transverse momentum of the positive decay product with respect to the decaying neutral particle direction, and α is the Armenteros variable.*

of neutral decaying particles are semi-ellipses in the $(\alpha, p_T^{h^+})$ plane.

5.5 MonteCarlo analysis of apparatus asymmetries

The COMPASS apparatus is not intrinsically left/right symmetric. The tracking detectors are centered with respect to the beam trajectory, so they have an acceptance which is larger for positive than for negative particles. Moreover, the configuration for the transversity measurement introduces an additional dipole magnetic field in the target region, with a bending direction opposite to the one of SM1 and SM2. The magnitude of the left/right asymmetry introduced by the apparatus can only be estimated from MonteCarlo simulations, by measuring

the production yields in the two halves of the apparatus defined by the $y-z$ plane. We have measured the counting rate asymmetry

$$\delta_{L/R}^{u(d)} = \frac{N_L^{u(d)} - N_R^{u(d)}}{N_L^{u(d)} + N_R^{u(d)}}, \tag{5.7}$$

where the superscript $u(d)$ denotes the upstream (downstream) cell, and $N_{L(R)}$ denotes the number of Λ produced with positive (negative) x-component of the momentum, for various bins of the Λ x_F and p_T (transverse momentum) variables. The results are shown in Fig. 5.9 and Fig. 5.10, where filled marks correspond to the asymmetry measured for primary vertices belonging to the upstream cell, while empty marks correspond to the downstream cell. The plots show an higher asymmetry value for the upstream cell, which is probably due to the longer path, compared to the downstream cell, that charged particles have to follow inside the target dipole magnetic field.

5.6 Measurement of $A_Y^{\uparrow(\downarrow)}$ in real data

The $A_Y^{\uparrow(\downarrow)}$ has been measured with the P2B and P2C data sets. The asymmetry calculation from two data sets with opposite spin configurations allows to correct for apparatus asymmetries, as discussed in App. C.

The available statistics has been divided into geometrical and kinematical bins for the analysis of the experimental asymmetries as a function of x_F and p_T. The reconstructed Λ candidates have been divided on the basis of the primary vertex position, the sign of the Λ momentum x-component (to separate left and right samples) and the x_F and p_T values. For each bin the V^0 invariant mass distribution has been stored.

The target cell selection is based on the position of the reconstructed primary vertex z coordinate, shown in Fig. 5.11. The upstream cell corresponds to vertex z coordinate $-1000 < z < -400$ mm, while the downstream cell corresponds to $-300 < z < 300$ mm. The two selected regions are shown in Fig. 5.11 with hatched areas. The x_F and p_T distributions for accepted Λ candidates are shown in Fig. 5.12. The full x_F range, from -1 to 1, has been divided into 10 bins; in the

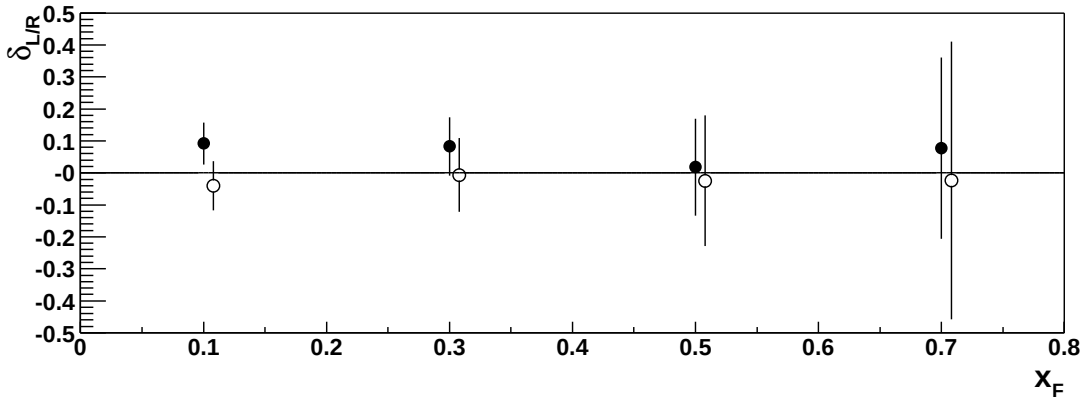

Figure 5.9: *Left/right MonteCarlo asymmetry, transverse configuration, x_F dependence. Filled points correspond to the upstream cell, empty ones to the downstream cell.*

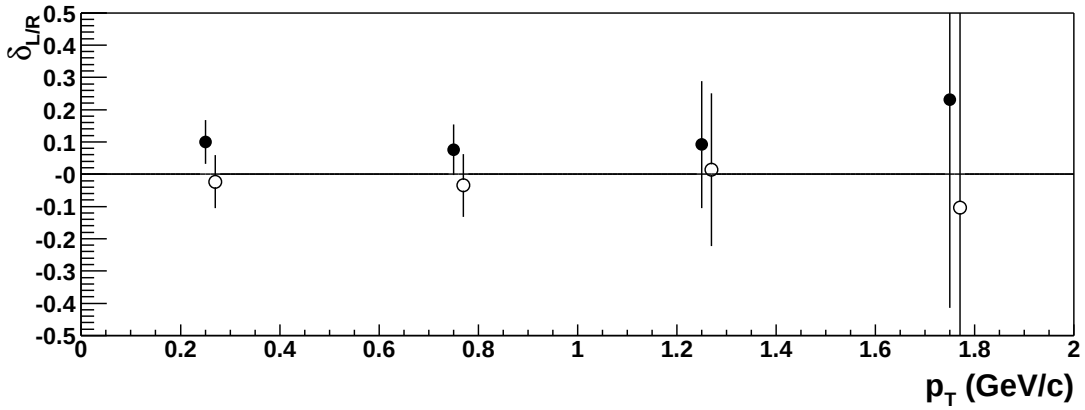

Figure 5.10: *Left/right MonteCarlo asymmetry, transverse configuration, p_T dependence. Filled points correspond to the upstream cell, empty ones to the downstream cell.*

analysis presented in this thesis only the positive values of x_F (corresponding to the current fragmentation region) are however considered. The p_T range from 0 GeV/c to 2.5 GeV/c has been divided into 5 bins.

For each bin the number of Λ candidates is measured for three regions of the invariant mass spectra, as shown in Fig. 5.13. Let's therefore introduce some notation to denote the counting rate asymmetry δ for the three regions:

$$\delta^{u(d)}_{A(B,C)} = \frac{N^{u(d)}_{A(B,C),L} - N^{u(d)}_{A(B,C),R}}{N^{u(d)}_{A(B,C),L} + N^{u(d)}_{A(B,C),R}}, \tag{5.8}$$

The corrected counting rate asymmetry $\delta^{u(d)}$ is then calculated as

$$\delta^{u(d)} = \delta^{u(d)}_B - \frac{\delta^{u(d)}_A + \delta^{u(d)}_C}{2}. \tag{5.9}$$

The quantities $\delta^{u(d)}$ are calculated as a function either of the x_F or the p_T variables. In both cases, an integration on the non-considered variable is performed. When considering the x_F dependence, an integration on the full p_T range is performed. In the case of the p_T dependence, the integration on x_F is performed in the interval $0 < x_F < 1$.

The quantities $\delta^{u(d)}$ are calculated independently for the two data sets P2B and P2C, and then divided by the measured target polarizations $P_T^{u(d)}$ and the

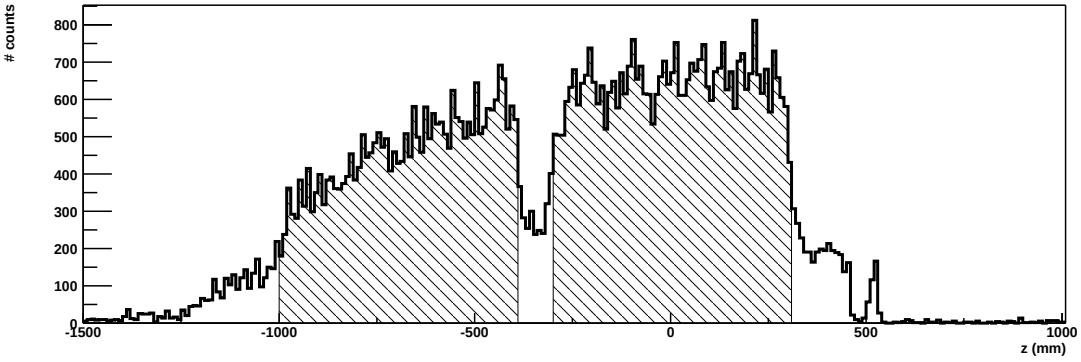

Figure 5.11: *Reconstructed z coordinate of primary vertices. The hatched areas show the cuts applied for the selection of the target cell.*

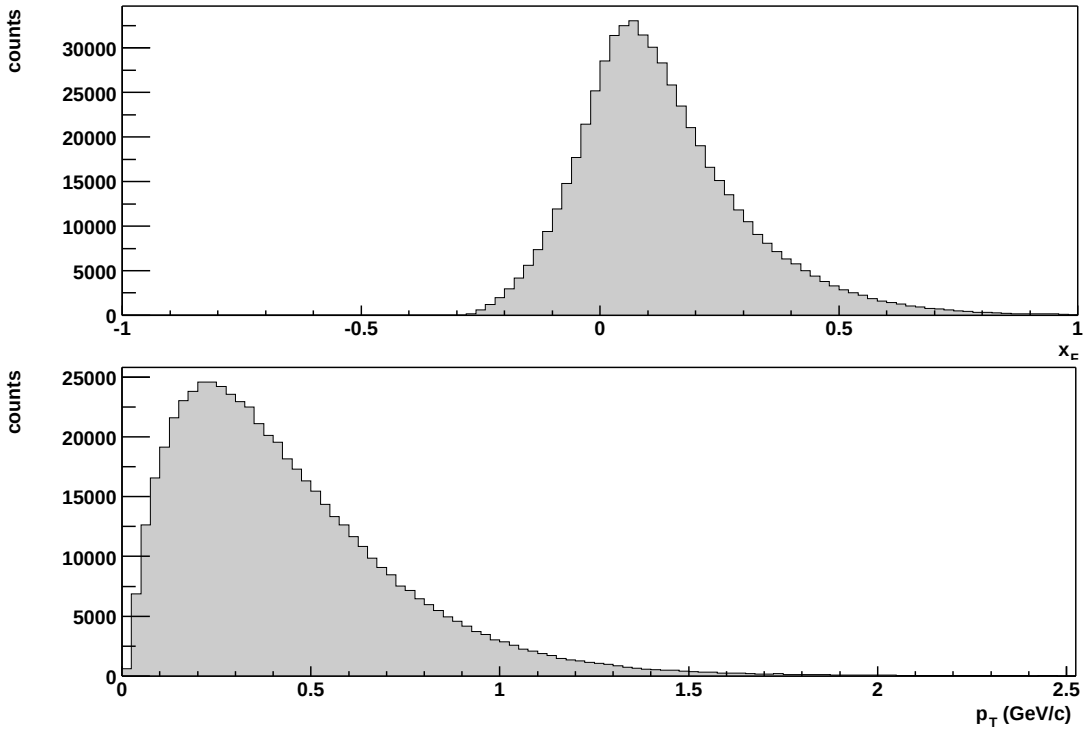

Figure 5.12: *Distributions of the reconstructed x_F (top plot) and p_T (bottom plot) variables for the selected Λ candidates.*

dilution factor $f = 0.5$. At this point four quantities are derived:

$$(A_Y^u)_{P2B} = \frac{\delta^u_{P2B}}{f(P_T^u)_{P2B}} \tag{5.10}$$

$$(A_Y^d)_{P2B} = \frac{\delta^d_{P2B}}{f(P_T^d)_{P2B}} \tag{5.11}$$

$$(A_Y^u)_{P2C} = \frac{\delta^u_{P2C}}{f(P_T^u)_{P2C}} \tag{5.12}$$

$$(A_Y^d)_{P2C} = \frac{\delta^d_{P2C}}{f(P_T^d)_{P2C}}. \tag{5.13}$$

	upstream cell	downstream cell
P2B	$(P_T^u)_{P2B}$ = -0.438	$(P_T^d)_{P2B} = 0.467$
P2C	$(P_T^u)_{P2C} = 0.468$	$(P_T^d)_{P2C} = -0.427$

Table 5.1: *Measured values of the upstream and downstream target cell polarizations for the two data sets analyzed.*

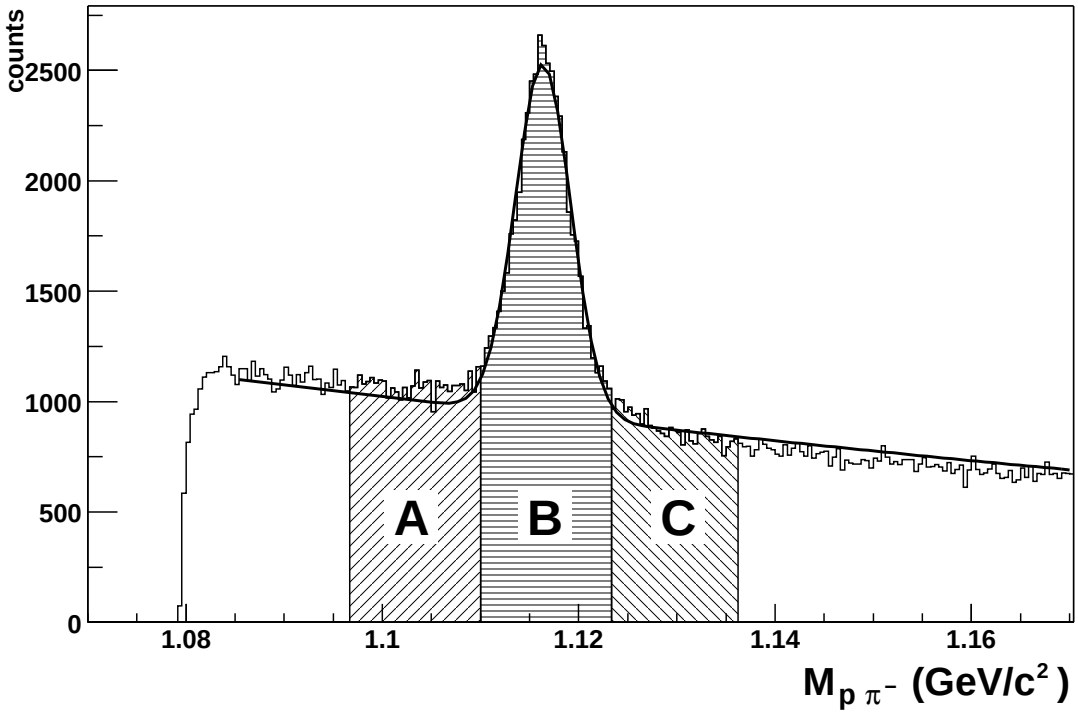

Figure 5.13: *Invariant mass distribution regions for evaluation of* Λ *signal and background contributions.*

The final result is obtained from the arithmetical mean of the P2B and P2C asymmetries, in order to correct for differences in the left and right apparatus acceptances, as discussed in App. C. At this point we are left with two asymmetries, one for the upstream (u) and one for the downstream (d) cell:

$$A_Y^u = \frac{(A_Y^u)_{P2B} + (A_Y^u)_{P2C}}{2} \tag{5.14}$$

$$A_Y^d = \frac{(A_Y^d)_{P2B} + (A_Y^d)_{P2C}}{2}. \tag{5.15}$$

The same calculation has been performed for the background contribution, starting from the counting rate asymmetries

$$\delta_{bgd}^{u(d)} = \frac{\delta_A^{u(d)} + \delta_C^{u(d)}}{2}. \tag{5.16}$$

The calculated values of $A_Y^{u(d)}$ as a function of x_F and p_T are shown in Figs. 5.14–5.17 (solid marks), together with the background contribution (empty

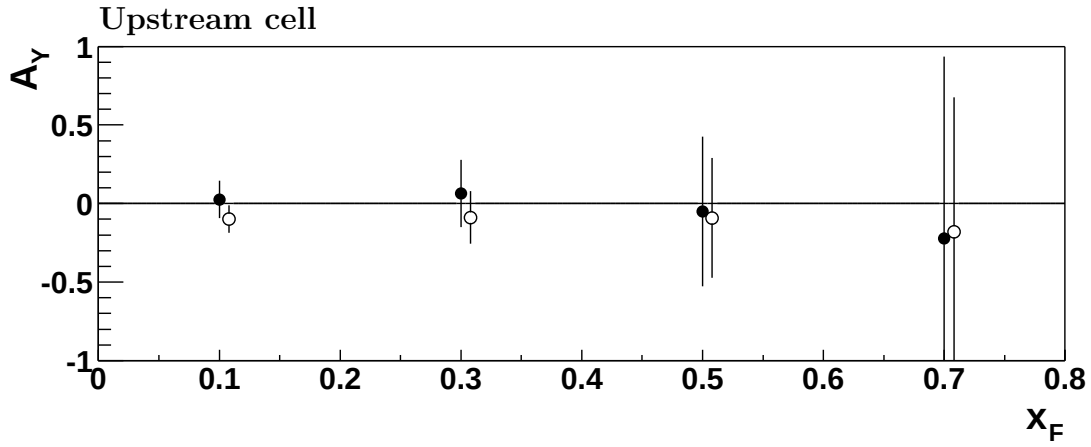

Figure 5.14: *Lambda sample: A_Y plotted as a function of x_F; upstream cell. Empty marks correspond to background contribution.*

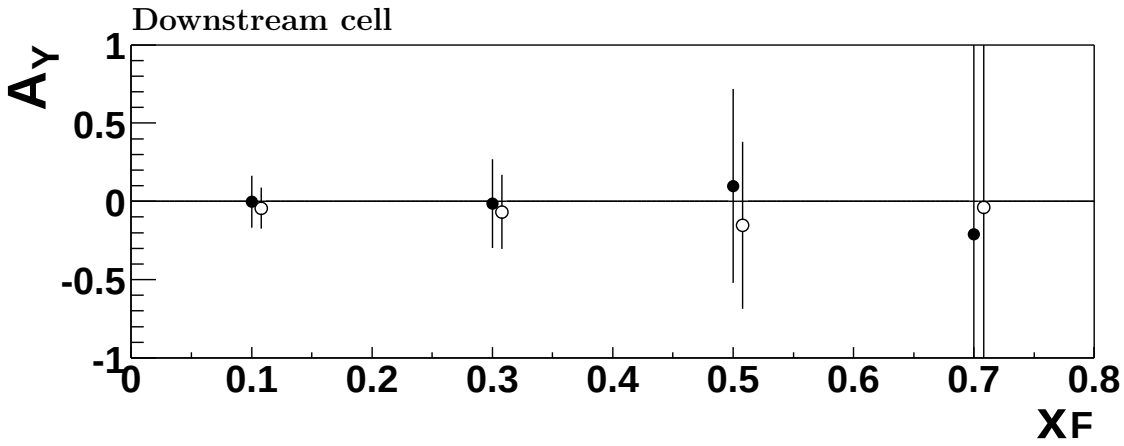

Figure 5.15: *Lambda sample: A_Y plotted as a function of x_F; downstream cell. Empty marks correspond to background contribution.*

marks). The measured A_Y is compatible with zero in all the presented distributions, except in the case of the p_T-dependence for the upstream cell. In that case anyway also the background contribution deviates from zero, an indication that further studies of the background behavior are needed. The preliminary conclusion is therefore that no spin dependence of the Λ production cross-section has been found in the transversity data sets currently available for the analysis.

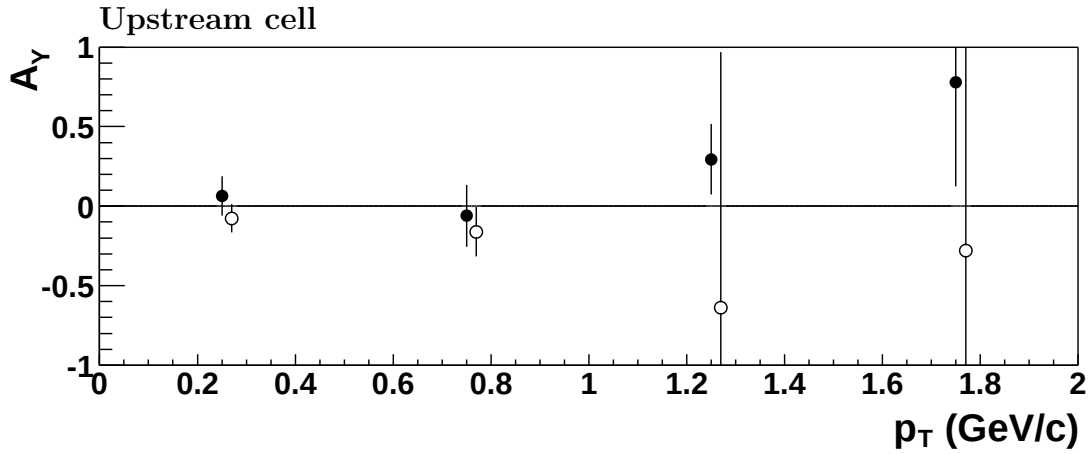

Figure 5.16: *Lambda sample: A_Y plotted as a function of p_T; upstream cell. Empty marks correspond to background contribution.*

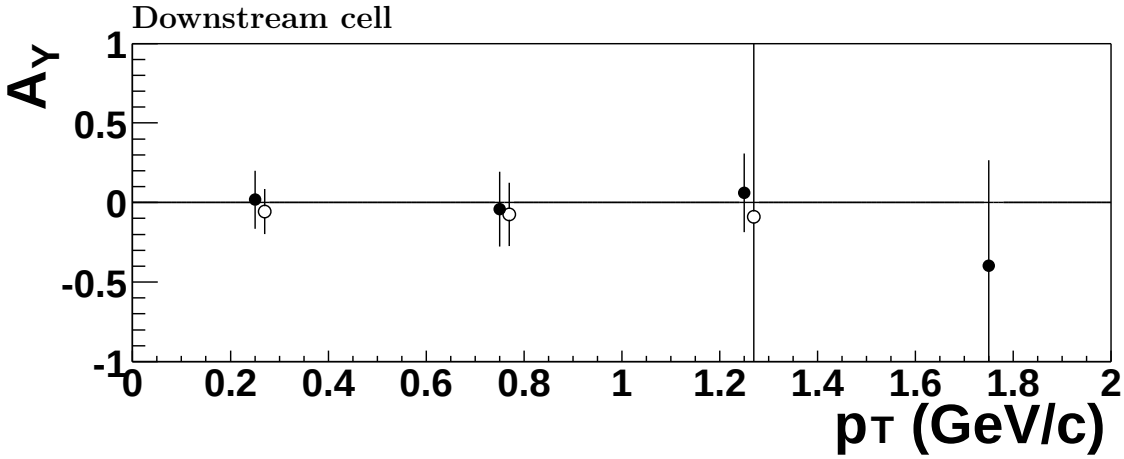

Figure 5.17: *Lambda sample: A_Y plotted as a function of p_T; downstream cell. Empty marks correspond to background contribution.*

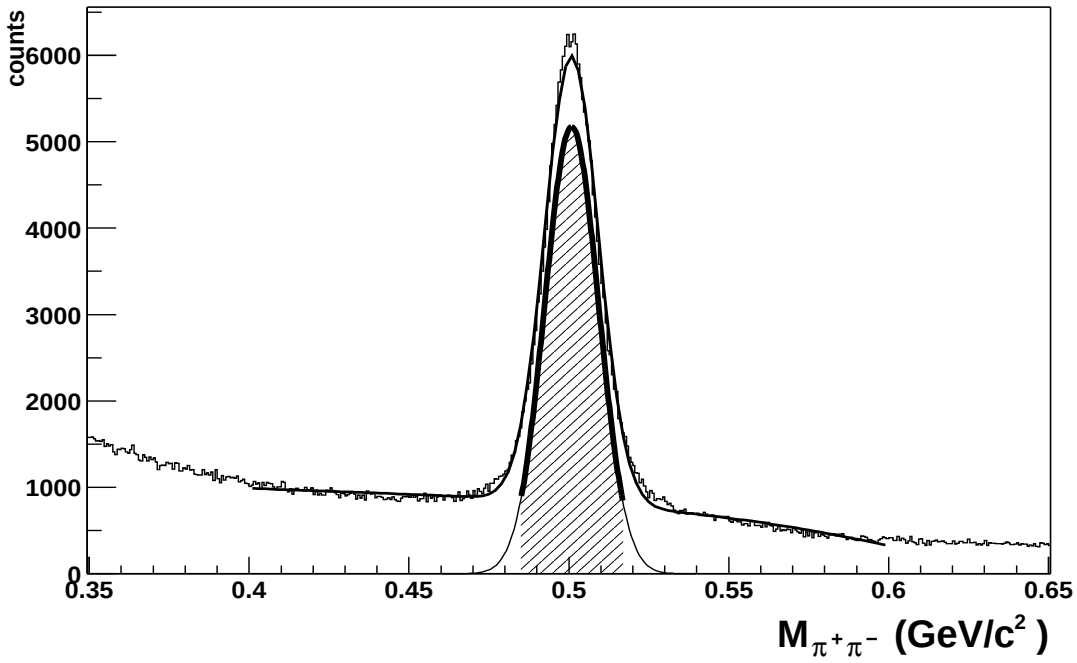

Figure 5.18: *Invariant mass distribution of the selected V^0 vertices, in the hypothesis of $K^0_S \to \pi^+\pi^-$ decay.*

5.7 Kaon contamination and asymmetries

The analysis procedure has been repeated on the kaon sample as well. The kaon statistics is much larger (see Fig. 5.18), and can be conveniently used to verify the results obtained in the previous section. Kaons are in fact spin 0 mesons, and therefore no spin-dependent effect should be observed when kaons are considered.

Moreover, the peak region of the Λ invariant mass distribution contains a non-negligible fraction of kaons. Fig. 5.19 shows the $\pi^+\pi^-$ invariant mass spectra when the Λ mass region is selected in the $p\pi^-$ invariant mass distribution. The number of kaons, resulting from the fit with a gaussian distribution plus a 3rd degree polynomial background, is ~ 3500, which is more than 10% of the reconstructed lambdas. The asymmetry calculation for the kaon sample therefore allows to evaluate the effect of the kaon background on the A_Y measurement for

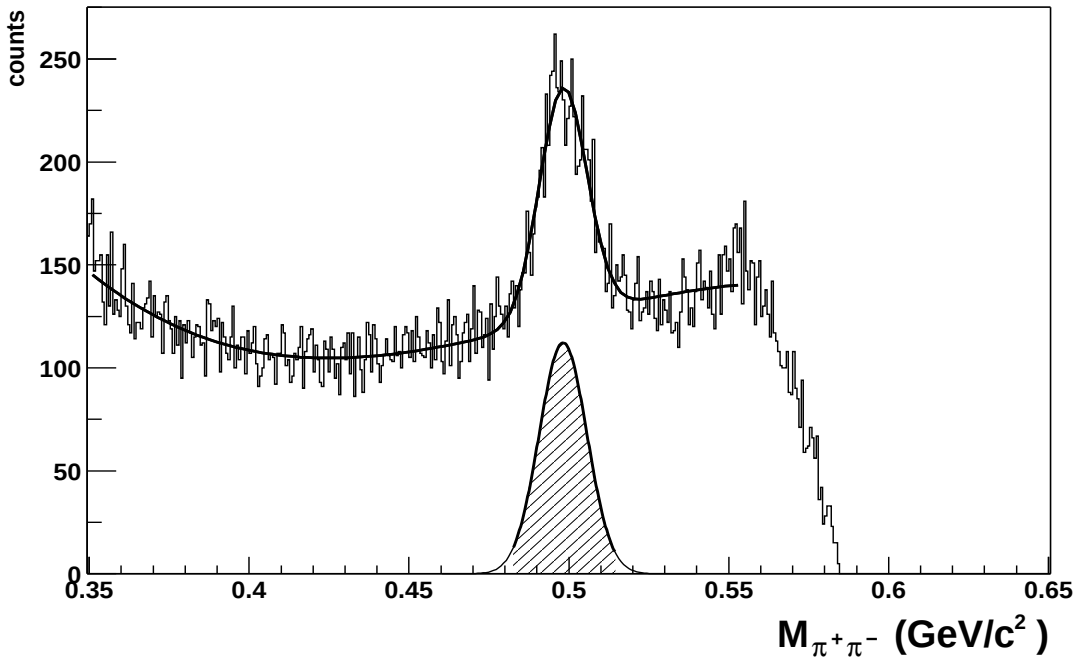

Figure 5.19: *K^0_S contamination below the Λ invariant mass peak. The estimated number of kaons is $\sim$ 3500, corresponding to the hatched area in the plot.*

the Λ sample. The results are shown in Figs. 5.20–5.23. The measured values of A_Y for the K^0 sample are all compatible with zero.

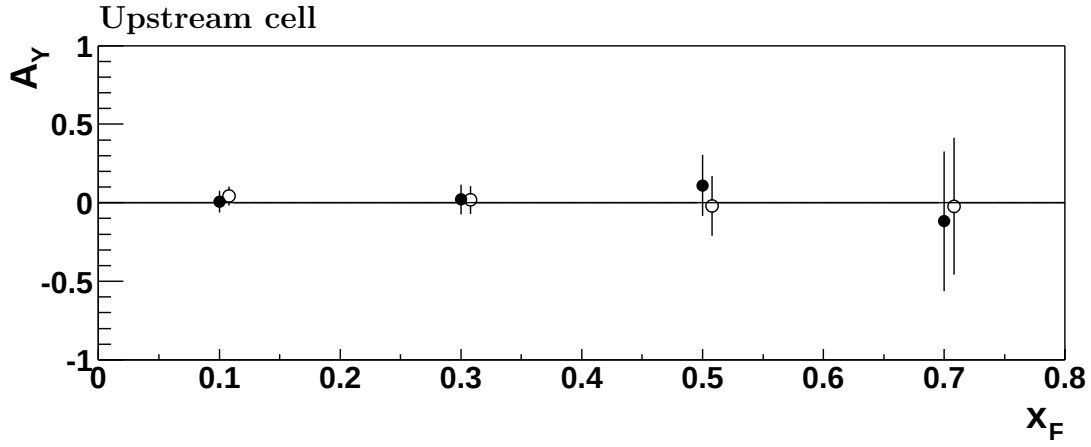

Figure 5.20: *Kaon sample: A_Y plotted as a function of x_F; upstream cell. Empty marks correspond to background contribution.*

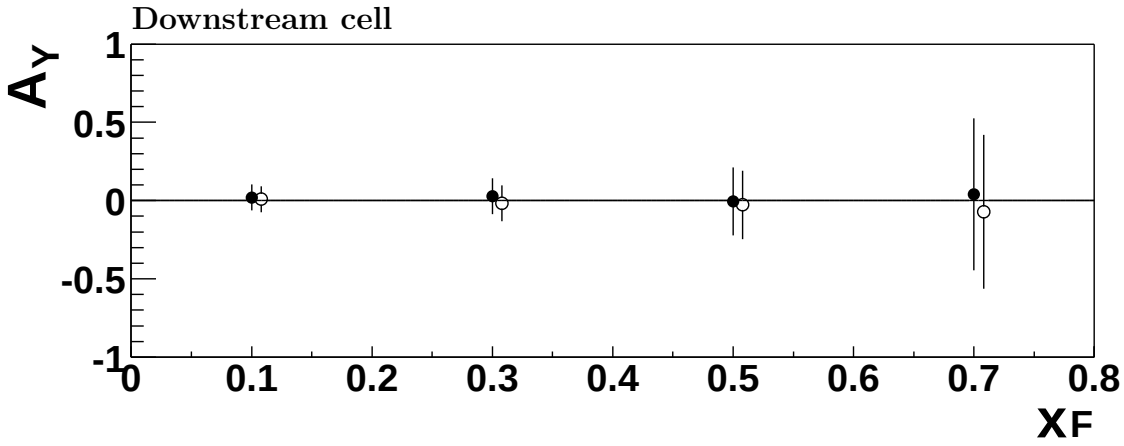

Figure 5.21: *Kaon sample: A_Y plotted as a function of x_F; downstream cell. Empty marks correspond to background contribution.*

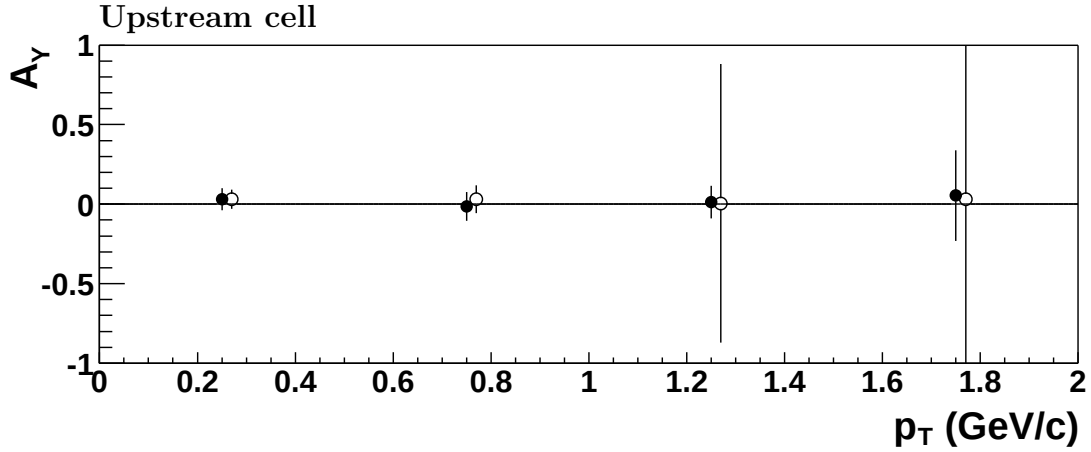

Figure 5.22: *Kaon sample: A_Y plotted as a function of p_T; upstream cell. Empty marks correspond to background contribution.*

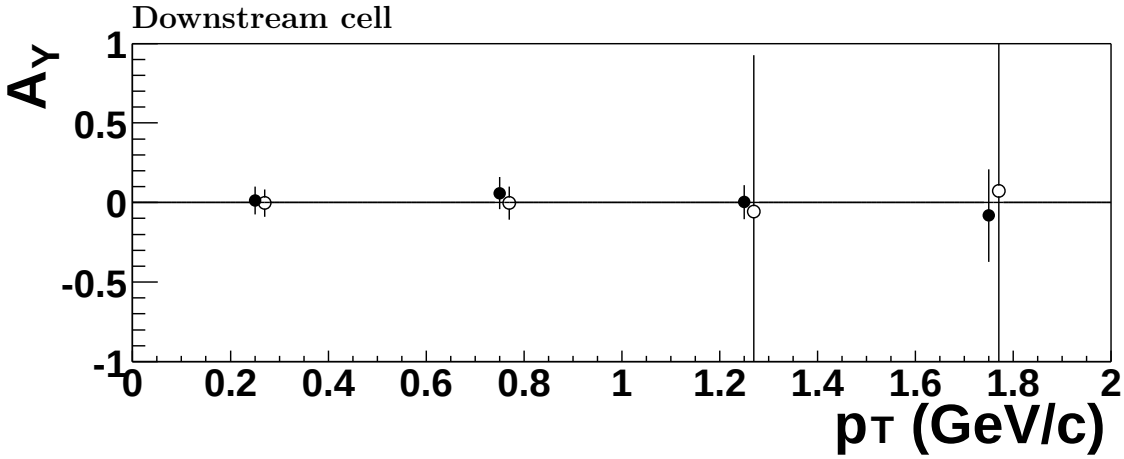

Figure 5.23: *Kaon sample: A_Y plotted as a function of p_T; downstream cell. Empty marks correspond to background contribution.*

Chapter 6

Conclusions

The COMPASS experiment has terminated its commissioning phase in the year 2000 and since then two years of data taking, with a polarized beam of 160 GeV positive muons and dedicated to the physical program, have been completed. This thesis has been developed in collaboration with the COMPASS-Torino group, that has several responsibilities in the experiment, both in the hardware, with the development of the MWPC read-out electronics, and in the software, with the development of the spectrometer alignment procedure and the analysis of spin observables in the Λ production channel.

MWPC detectors are a key project for the COMPASS experiment, since they represent the main tracking system of the small angle spectrometer where most of the scattered muons are identified and reconstructed. The COMPASS muon program requires the measurement of the DIS kinematics, and therefore of the momenta of the beam and of the scattered muons. The requirements for the muon trackers are high detection efficiency and performances to be stable all along the data taking periods, while the spatial resolution is not a really critical issue due to the long lever-arm available for the muon tracking. All these requirements are fulfilled by MWPC detectors with 2 mm wire spacing. However, the high particle flux existing in COMPASS obliges to keep their gas gain as low as possible, to prevent aging effects and to achieve long-term stability.

The COMPASS MWPC project is part of the long-term collaboration between the Torino group and the LNP Dubna group. The experience of the Dubna group has been extremely important for the refurbishing and operation of the MWPC detectors, previously used in the Ω spectrometer. The Torino group has taken responsibility of the development of the readout electronics.

A high performance readout electronics is essential to get the best results from the MWPC detectors. The work described in this thesis has lead to a final design of the frontend electronics which fulfills all the requirements for the muon tracking. This electronics allows to reach a high detection efficiency even for low gas gains needed to avoid detector aging. The analysis of the performances of the detector and of the electronics in terms of noise, cross-talk, efficiency, and spatial and time resolutions, which I performed using the available experimental data, have been presented in detail. The measured efficiency is above 98% for all the installed detectors, and the spatial resolution is ~ 0.7 mm.

The MWPC detectors, equipped with the final version of the readout electronics, have been operated for two years of data taking in standard conditions.

The MWPC system has also been fundamental in the early stage of the spectrometer assembly, when it was one of the few available tracking systems and has allowed to debug the offline analysis programs.

The stability of the MWPC readout system is continuously monitored by an online test system developed by the INFN laboratories in Torino, that has been part of the work of this thesis. In particular I have used it to implement an automatic procedure for the on-site calibration of all the $\sim$ 26000 MWPC readout channels.

In this phase of the experiment our analysis is concentrated on the transversity data, in particular on the Λ^0 production channel. The final goal is to measure spin observables, as the spin transfer from the target nucleon to the final-state Λ^0, that is the depolarization factor D_{YY}, together with the single-spin asymmetry A_Y. So far only some preliminary results on A_Y are available and are presented in this thesis. However all the software tools needed for the whole program of physics are ready. The preliminary A_Y measurement shows

no dependence of the Λ^0 production cross-section on the target spin. A second transversity data set, with a statistics comparable with the one used in this thesis, will be soon processed. New results on the Λ polarization and the D_{YY} are expected in the near future.

Appendix A

Calibration procedure of MWPC frontend electronics

The frontend electronics requires calibration of each preamplifier/discriminator channel, if low noise and high detection efficiencies have to be achieved. Calibrating a channel means finding, for a given input signal amplitude, the value of the threshold voltage for which the discriminator output frequency is half the input signal frequency. The calibration of the 26000 amplifier-discriminator channels used for the COMPASS MWPC readout is performed using the semi-automatic test system described in chapter 3. The calibration is performed by measuring the threshold voltage for three different values of input signal amplitude. Assuming a linear response of the discriminator chips, this completely defines the calibration curve parameters.

The step-like response of an ideal discriminator chip is smoothed in the real case by the electronics noise at the input of the discriminator. When a signal of fixed amplitude and frequency is injected at the input and the threshold voltage is varied around the threshold value, the counting rate varies smoothly between 0 and the input rate. The procedure used for the calibration of the MWPC frontend electronics uses this behavior for iteratively finding the threshold value for each given input amplitude.

As a matter of fact, the signal frequency at the output of the discriminator

goes to zero only if the threshold voltage is above the intrinsic noise level of the chip. For threshold values below the noise level self-oscillations of the chip produce an output signal even if the input amplitude is zero. This fact has to be taken into account in the calibration procedure, in order not to bias the threshold measurement at small input amplitudes. The first step of the procedure is therefore the measurement of the noise level for each discriminator chip. Starting from an high value, the threshold voltage for each discriminator chip is lowered in steps of 2 digits (~ 0.5 fC) until the output frequency is equal to 1/10 of the trigger frequency. The $(i-1)$-th threshold value, if i is the last step index, is stored as the noise level. The procedure is performed in parallel for all discriminator chips, until all noise levels have been found.

After that the real threshold measurement is performed. The input signal amplitude is set to a given value and the threshold for each readout channel is measured. To do that, the threshold voltage is set to an high value and lowered in steps of 20 digits. At each step 1000 pulses are injected in the discriminator input, and the number of output pulses is measured. The progressive decreasing of the threshold stops when the the number of output pulses is greater than 500, or the noise level is reached. In the second case, the channel is considered broken and the procedure stops, otherwise an interval in which the threshold value is included has been found. The interval is then splitted in two pieces, by measuring the counting rate in the middle point and keeping the half in which the threshold value is contained. The splitting procedure is iterated until the measured counting rate differs from the input rate of less than 10%.

The described procedure is repeated for three values of input signal amplitude (4, 8 and 12 fC), and the measurement is performed in parallel on 1/4 of the readout channels at a time. The reason for not measuring all readout channels in one go is to avoid cross-talk contributions to the counting rates. If adjacent channels are not injected both at the same time, the channel counting rate depends only on the signal amplitude at the corresponding input.

The result of the calibration procedure on one frontend triplet is shown in Figs. A.1–A.2. The plots show the counting rate of each of the 192 channels

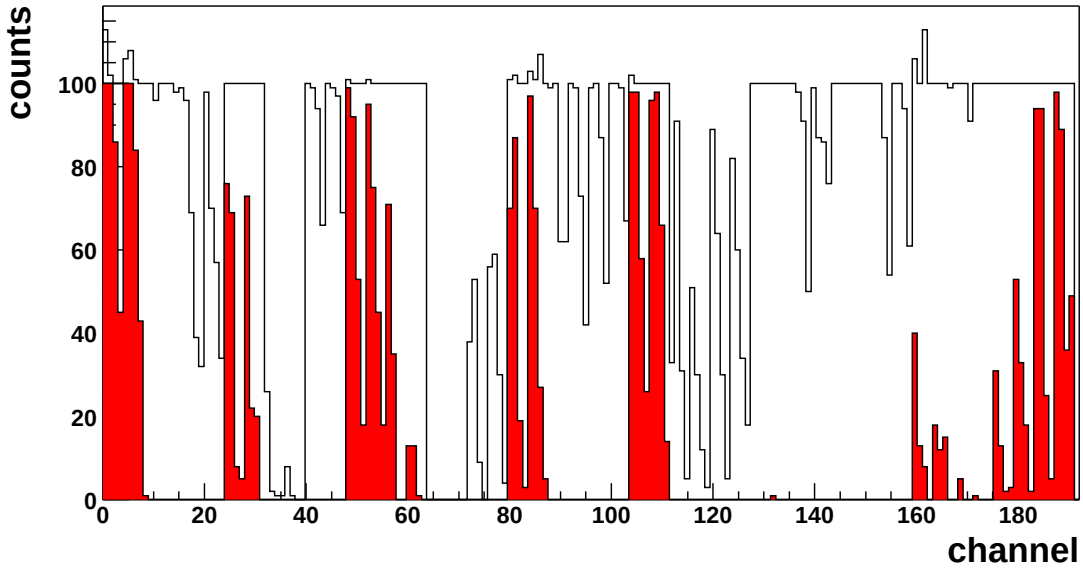

Figure A.1: *Raw hits profile for one frontend triplet, with an injected signal of 6 fC. Discriminator chips are not calibrated, common threshold is 55 digits*

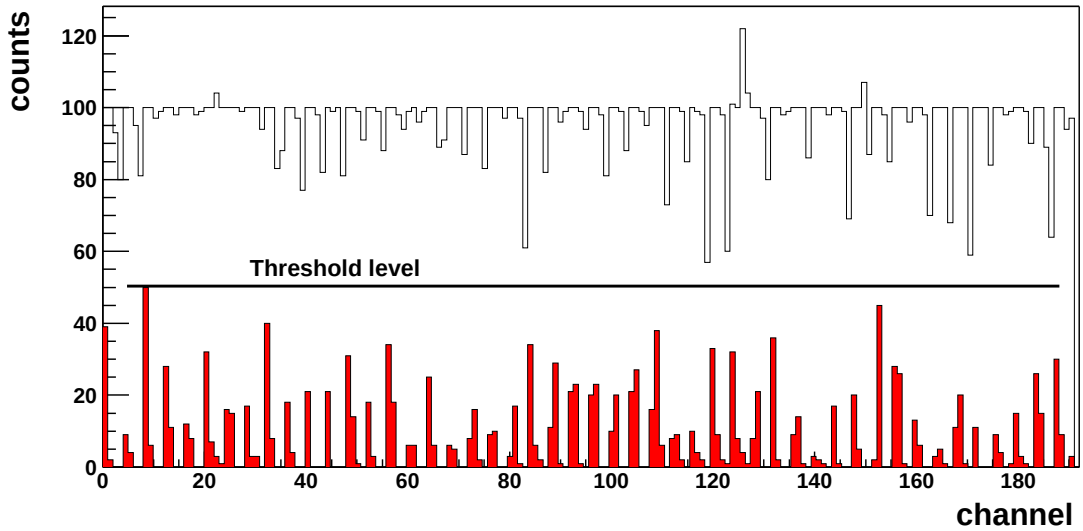

Figure A.2: *Raw hits profile for one frontend triplet, with an injected signal of 6 fC. Applied threshold after calibration is 5 fC (white plot) and 7 fC (red plot).*

when 100 pulses of 6 fC amplitude are injected at the inputs. The first plots are obtained by setting the threshold voltage to fixed digital values, while the second are obtained after performing the frontend triplet calibration. The white plot is obtained with a threshold voltage corresponding to 5 fC, the filled one with a threshold of 7 fC; the counting rate expected for a threshold voltage of 6 fC is shown as an horizontal line on the figure.

The described procedure requires ~ 30 minutes to calibrate all the ~ 26000 MWPC readout channels. The online test system used for injecting the calibrated pulses allows to perform the calibration when the detectors are installed in the experimental area. The procedure can therefore be repeated once in a while to compensate variations in the response of the discriminator chips and threshold DACs.

Appendix B

Tracking algorithm for MWPC efficiency analysis

A precise measurement of the detector efficiency can only be obtained from the analysis of reconstructed tracks. Despite the availability of the official COMPASS track reconstruction software (CORAL) a custom algorithm has been developed for the analysis of MWPC reconstruction efficiency. The custom software has the advantage to have been specifically tuned on MWPC characteristics; moreover it is faster and smaller than the whole CORAL code, which makes it ideal for online analysis of detector performances. Finally the results do not depend on the overall performances of the whole apparatus, since the 11 available MWPC stations can be treated as a standalone tracking system.

The number of MWPC stations installed in the COMPASS apparatus is 11, spread over a $\approx$ 40 m long region. The first three stations are placed before the second spectrometer magnet SM2, five stations are between SM2 and the second hadron absorber μF2, and three stations are behind μF2. The region covered by MWPC stations can thus be divided in three sections, containing 10, 15 and 9 planes respectively. If a minimum number of 7 planes is required for track reconstruction, all sections have a sufficient number of planes to perform tracking, even if some inefficiency exists.

Tracks in each section are reconstructed and fitted using simple straight

lines, since the effect of the magnetic field can be neglected. The tracking algorithm performs several steps:

1. reconstruction of space points for each MWPC station;
2. track candidates finding using space points;
3. track fitting and merging.

B.0.0.3 Space points reconstruction

The tracking procedure used for MWPC analysis takes advantage of the fact that MWPC planes are organized in stations in such a way that each station provides 3 or 4 coordinates and thus can identify the particle crossing point; a typical wire pattern defined by one MWPC station is shown in Fig. B.1. Only space points with at least 3 correlated wires are kept, in order to effectively reject combinatorial background. The developed algorithm allows to separate space points even in presence of very high multiplicities. No restriction is made on the number of space points to which a single hit wire can be associated, in order to account for ambiguous situations.

B.0.0.4 Candidate track finding

Reconstructed space points are used as pivots for finding candidate tracks. At the end of the previous step, a list of space points is created for each MWPC station. The next step is to identify candidate tracks in each section of the apparatus. This is done by selecting two stations of one section as pivots, and calculating the straight lines connecting all their space points. The lines are then extrapolated to non-pivot stations, and the intersection point is compared with fired wires. If their distance is smaller than a certain threshold, which has been set to four times the detector pitch, the wire is associated to the candidate track. The ratio between the number of associated wires and of intersected planes is used to select "good" candidate tracks, by requiring a value higher than 0.7. A plane is considered "intersected" if the extrapolated point falls

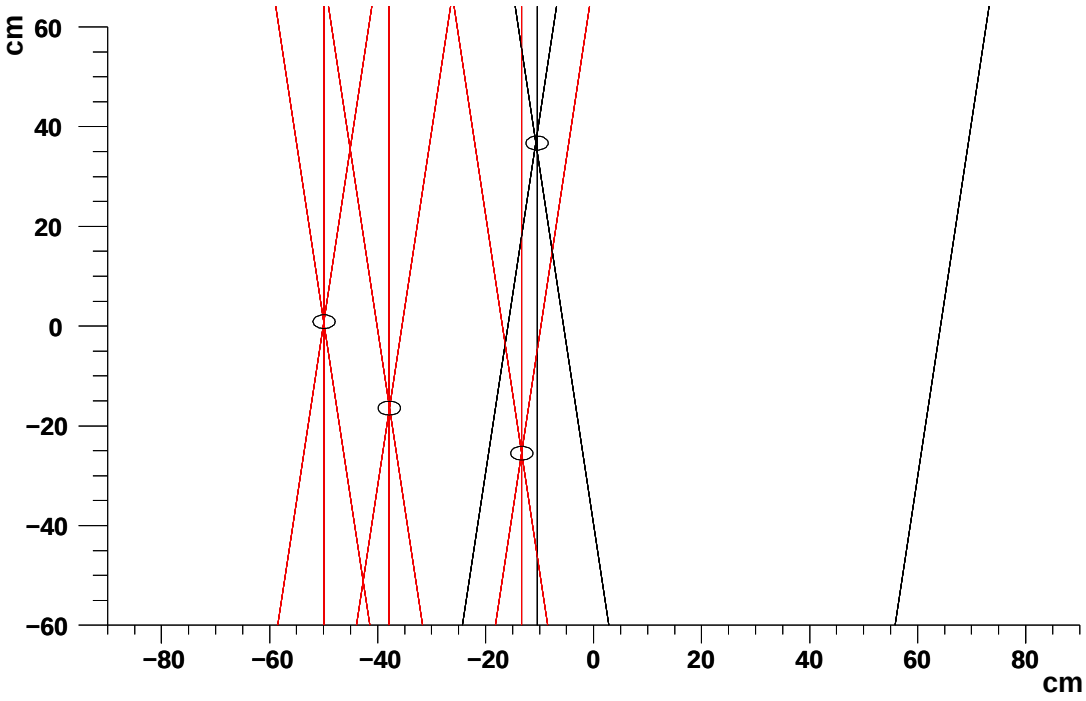

Figure B.1: *Typical wire pattern for a reconstructed event in one MWPC station with 3 planes. Circles represent accepted space points correlated with reconstructed tracks. The axis show the hit position with respect to the chamber center.*

inside the detector active area, taking into account the presence of a central dead zone. The procedure is repeated with all the possible combinations of pivot stations and a list of "good" candidates is created.

The described method has the disadvantage of creating up to N candidate tracks for each real track, with $N = n!$ if n is the number of stations in one section. A merging step is for this reason required at the end of the fitting procedure.

B.0.0.5 Track fitting & merging

Track candidates are fitted using a χ^2 minimization procedure. Plane resolution is assumed equal to the wire pitch. The candidate track is fitted a first time using the list of hits obtained in the previous phase. After that the correlated hits are

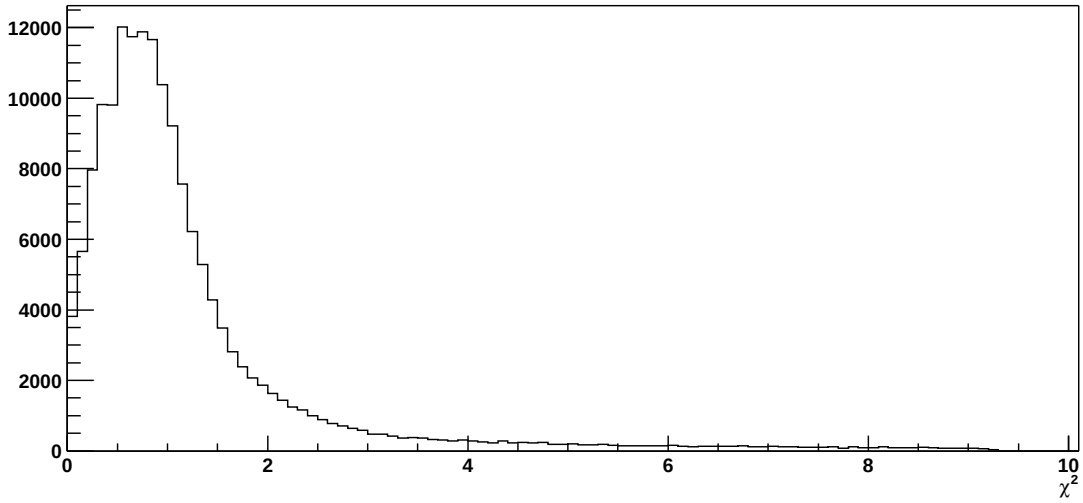

Figure B.2: χ^2 *distribution of reconstructed tracks.*

calculated again, using the new track parameters, and the fit is repeated. This two-step procedure allows to correct the possible extrapolation errors arising from the simple calculation of track parameters performed in the candidate finding phase.

After fitting the tracks are selected using some simple criteria based on χ^2 and track horizontal and vertical angles. We call α the angle existing between the track and the $y-z$ plane (vertical plane), and β the angle between the track and the $x-z$ plane (horizontal plane). A track is rejected if:

- the χ^2 *probability* of the track fit is lower than 0.01, or
- α or β angle is outside some section-dependent limits, which are set in a configuration file.

The α angle is typically constrained to be $-1 < \alpha < 1$ degrees, since all particles are deviated horizontally by the magnets and have no big angle with respect to the horizontal plane. The β angle can also have large values, but it is constrained to be $0 < \beta < 30$ in the last section, since all hadrons are stopped in the absorber and only scattered muons are reconstructed there.

If a track satisfies the above conditions, it is considered "good" and is passed to the final merging step. The list of hits associated to the track is compared to already accepted track, to find possible duplicated tracks. If another track with a similar list of hits is find, the two track are "merged", in the sense that the one with the best χ^2 probability is kept. This allows to reject all the duplicated tracks created in the candidate finding phase.

The χ^2 distribution of the reconstructed tracks is shown in Fig. B.2. The distribution is peaked around $\chi^2 = 1$, a typical value for well reconstructed particle trajectories. A comparison of the MWPC-based reconstruction with the standard COMPASS reconstruction packaged CORAL is shown in Fig. B.3; the event is not only correctly reconstructed, but also the extrapolation to the boundaries of the three sections covered by MWPC stations is good, even if no bridging is applied.

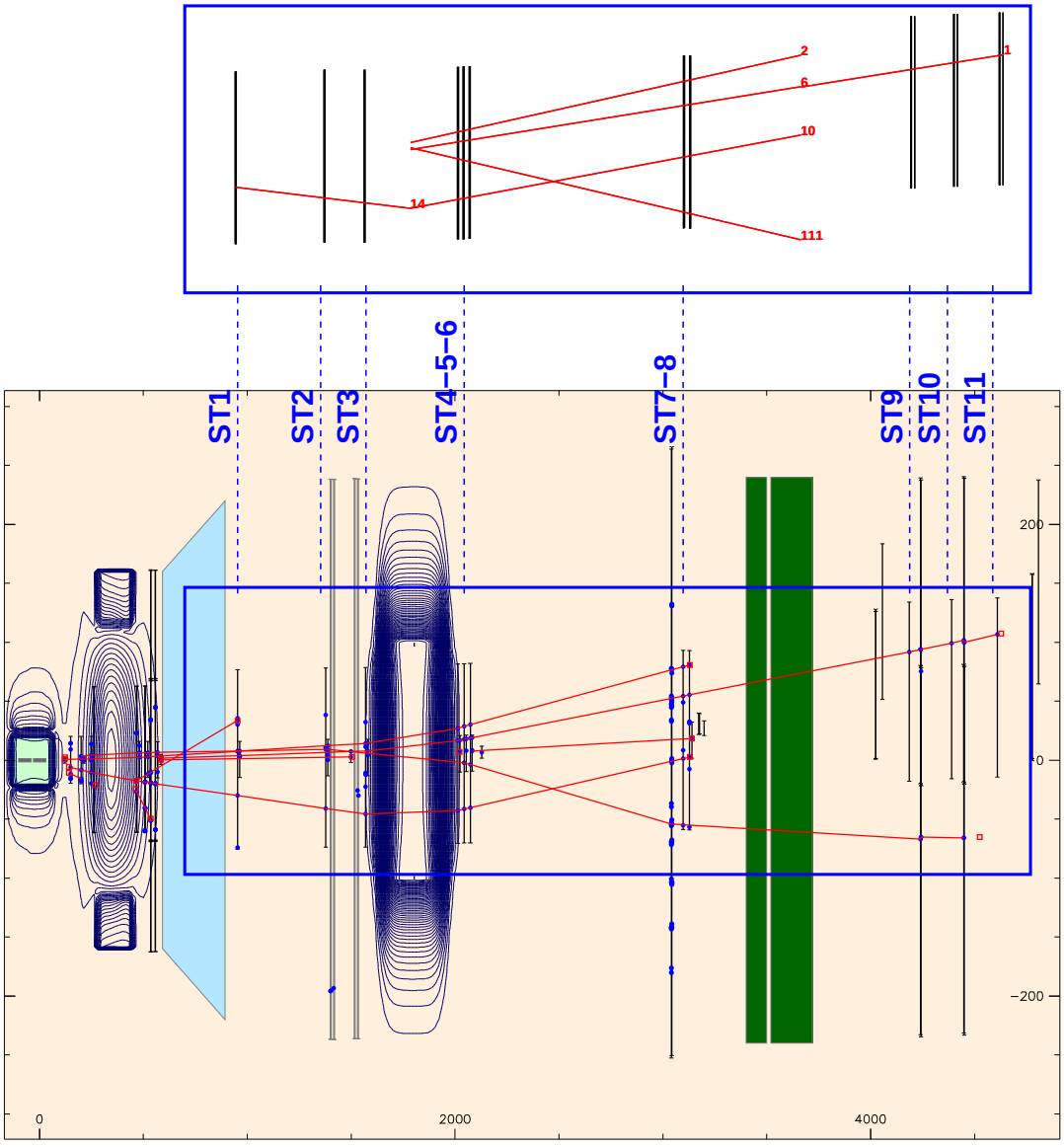

Figure B.3: *Comparison between MWPC-based track reconstruction and the standard COMPASS tracking package, named CORAL. Bottom picture shows CORAL reconstruction with all available detectors included; top picture shows the result of the custom tracking procedure, using only MWPC stations.*

Appendix C

Target acceptance correction by means of independent measurements with opposite cell polarizations

The analyzing power represents the dependence of the Λ production cross-section on the target spin orientation. In the case of transverse target spin configuration, the analyzing power is given by

$$A_Y = \frac{\mathrm{d}\sigma^{\uparrow} - \mathrm{d}\sigma^{\downarrow}}{\mathrm{d}\sigma^{\uparrow} + \mathrm{d}\sigma^{\downarrow}}, \tag{C.1}$$

where $\mathrm{d}\sigma^{\uparrow(\downarrow)}$ denotes the Λ production cross-section for target spin oriented along (opposite) to the y axis. The measurement of the cross-sections requires a correct evaluation of the apparatus acceptance.

When the target cells are transversely polarized the DIS process, in the hypothesis of virtual photon exchange, presents a rotational invariance along the beam axis. The rotational invariance of the production cross-section means that a Λ produced on the left with respect to the $y - z$ plane and from a cell with spin oriented upward, is "equivalent" to a Λ produced on the right from a cell with spin oriented downward.

For this reason for each target polarization the left and right samples have to be analyzed separately. Therefore we define a left and a right analyzing power by

$$A_Y^{L(R)} = \frac{\mathrm{d}\sigma^{\uparrow}_{L(R)} - \mathrm{d}\sigma^{\downarrow}_{L(R)}}{\mathrm{d}\sigma^{\uparrow}_{L(R)} + \mathrm{d}\sigma^{\downarrow}_{L(R)}}. \tag{C.2}$$

The extraction of A_Y requires to perform two measurements with opposite target cells orientations. In the simplest case of a single target cell the two independent measurements are performed before and after polarization reversal. Let's first of all introduce some useful notations:

- $\Phi_{1(2)} \rightarrow \mu$ flux,
- $n \rightarrow$ area density of target nucleons,
- $a_{L(R)} \rightarrow$ acceptance,
- $f \rightarrow$ dilution factor (useful fraction of target),
- $P_T \rightarrow$ target polarization.

In the previous definitions the subscript 1 (2) refers to the measurement performed before (after) polarization reversal, and $L(R)$ to the left/right Λ measurements.

The number of DIS events measured in the two data sets is given by

$$N_1^{L(R)} = n\Phi_1 a_{L(R)}(\bar{\sigma}_{L(R)} - \frac{1}{2} f P_T \Delta\sigma_{L(R)}) \tag{C.3}$$

and

$$N_2^{L(R)} = n\Phi_2 a_{L(R)}(\bar{\sigma}_{L(R)} + \frac{1}{2} f P_T \Delta\sigma_{L(R)}), \tag{C.4}$$

where we have defined

$$\bar{\sigma}_{L(R)} = \frac{1}{2}(\mathrm{d}\sigma^{\uparrow}_{L(R)} + \mathrm{d}\sigma^{\downarrow}_{L(R)}), \tag{C.5}$$

$$\Delta\sigma_{L(R)} = \mathrm{d}\sigma^{\uparrow}_{L(R)} - \mathrm{d}\sigma^{\downarrow}_{L(R)}. \tag{C.6}$$

The value of $\Delta\sigma$ is given by

$$\Delta\sigma_{L(R)} = \frac{1}{n a_{L(R)} f P_T} \left(\frac{N_2^{L(R)}}{\Phi_2} - \frac{N_1^{L(R)}}{\Phi_1} \right). \tag{C.7}$$

The flux values $\Phi_{1(2)}$ appearing in the above expression are generally unknown, and their difference can be of the order of $2 - 4\%$. This introduces an error in the measurement, which cannot be reduced by increasing N_1 and N_2.

The usual way to eliminate flux factors in the measurement of cross-section differences is to simultaneously perform the measurement on two target cells with opposite polarizations. In this case the beam flux on the two cells can be considered equal, but one has to account and correct for the different apparatus acceptance and target material of the two cells. It is necessary to introduce in this case separate values of $a_{u(d)}$ and $n_{u(d)}$, where the subscript $u(d)$ denotes the upstream (downstream) cell. From this point on the $L(R)$ notation will be dropped for the sake of simplicity; it will be reintroduced in the final expressions for completeness.

In the ideal case in which

$$a_u = a_d = a, \quad n_u = n_d = n, \tag{C.8}$$

the derivation of A_Y is straightforward. If we denote with $N_{u(d)}$ the counting rate for the upstream (downstream) cell, we have

$$N_d - N_u = n\Phi a f P_T \Delta\sigma, \tag{C.9}$$

$$N_d + N_u = 2n\Phi a \bar{\sigma} \tag{C.10}$$

and the relation between the counting rate asymmetry δ and the cross-section asymmetry is given by

$$\delta = \frac{N_d - N_u}{N_d + N_u} = f P_T \frac{\Delta\sigma}{2\bar{\sigma}} = f P_T A_Y. \tag{C.11}$$

In a real experiment the two cells are exposed to the same beam flux but they see different apparatus acceptances, and two independent measurements with opposite configurations of the cell polarization directions are needed. If we define $m = P_\mu |P_T| f$, the counting rates and experimental asymmetries for the two configurations are given by:

- configuration $u_\uparrow\ d_\downarrow$:

$$N'_u = n_u \Phi' a'_u \bar{\sigma}\,(1 + mA_Y)\,, \tag{C.12}$$

$$N'_d = n_d \Phi' a'_d \bar{\sigma}\,(1 - mA_Y)\,, \tag{C.13}$$

$$\delta' = \frac{N'_u - N'_d}{N'_u + N'_d} \tag{C.14}$$

- configuration $u_\downarrow\ d_\uparrow$:

$$N''_u = n_u \Phi'' a''_u \bar{\sigma}\,(1 - mA_Y)\,, \tag{C.15}$$

$$N''_d = n_d \Phi'' a''_d \bar{\sigma}\,(1 + mA_Y)\,, \tag{C.16}$$

$$\delta'' = \frac{N''_d - N''_u}{N''_d + N''_u}. \tag{C.17}$$

From the primed expressions we can derive, with $A \equiv A_Y$,

$$\delta' = \frac{(1 + mA) - x(1 - mA)}{(1 + mA) + x(1 - mA)}, \tag{C.18}$$

where we have defined $x = \dfrac{n'_d a'_d}{n'_u a'_u}$. From the double-primed expression we have, in a similar way,

$$\delta'' = \frac{kx(1 + mA) - (1 - mA)}{kx(1 + mA) + (1 - mA)}, \tag{C.19}$$

where $k = \dfrac{(a''_d/a''_u)}{(a'_d/a'_u)}$. Extracting x from the two above expressions we have

$$x = \frac{(1 + mA)(1 - \delta')}{(1 - mA)(1 + \delta')} = \frac{1}{k}\frac{(1 - mA)(1 + \delta'')}{(1 + mA)(1 - \delta'')}. \tag{C.20}$$

If we assume that $k = 1$, i.e. that the ratio of apparatus acceptances is the same before and after the polarization reversal, we obtain

$$\frac{(1 - mA)^2}{(1 + mA)^2} = \frac{(1 - \delta')(1 - \delta'')}{(1 + \delta')(1 + \delta'')} = \frac{N'_d N''_u}{N'_u N''_d} = J. \tag{C.21}$$

This is a 2^{nd} order equation in A, with solutions

$$A = \frac{(1 + J) \pm 2\sqrt{J}}{m(1 - J)}. \tag{C.22}$$

The value of A is constrained to be $|A| < 1$, so we take the solution with the "$-$" sign. From eq. C.21 we have

$$(1+J) = \frac{2(1+\delta'\delta'')}{(1+\delta')(1+\delta'')}, \tag{C.23}$$

$$(1-J) = \frac{2(\delta'+\delta'')}{(1+\delta')(1+\delta'')}, \tag{C.24}$$

$$\sqrt{J} = \frac{\sqrt{(1-\delta'^2)(1-\delta''^2)}}{1+\delta')(1+\delta'')} \approx \frac{1-\frac{1}{2}(\delta'^2+\delta''^2)}{(1+\delta')(1+\delta'')}, \quad \text{if } \delta', \delta'' \text{ small} \tag{C.25}$$

which leads to

$$A = \frac{(1+\delta'\delta'') - (1-\frac{1}{2}(\delta'^2+\delta''^2))}{m(\delta'+\delta'')} = \frac{\boldsymbol{\delta'+\delta''}}{\mathbf{2m}}. \tag{C.26}$$

The corrected asymmetry is therefore equal to the arithmetical mean of the asymmetries before and after polarization reversal.

C.0.0.6 Statistical error

The statistical error on the counting rate asymmetries δ' and δ'' is given by

$$\nu(\delta') = \frac{4N'_u N'_d}{(N'_u+N'_d)^3} = \frac{1}{N'}\frac{1}{1-\alpha^2}, \tag{C.27}$$

$$\nu(\delta'') = \frac{4N''_u N''_d}{(N''_u+N''_d)^3} = \frac{1}{N''}\frac{1}{1-\alpha^2}, \tag{C.28}$$

where $\alpha = \dfrac{a_u - a_d}{a_u + a_d}$ is a factor which takes into account the error due to differences of acceptance of the two cells. If we assume $N' \simeq N'' = N_{Tot}/2$ the statistical error on the measured asymmetry is

$$\sigma(A) = \frac{1}{m\sqrt{1-\alpha^2}}\frac{1}{\sqrt{N_{Tot}}}. \tag{C.29}$$

C.0.0.7 Second-order acceptance corrections

If $k \neq 1$, i.e. the ratio of the cells acceptances is different before and after polarization reversal, an additional factor appears in the expression C.26 for A:

$$A = \frac{\delta'+\delta''}{2m} - \frac{k-1}{4m}. \tag{C.30}$$

This correction is not taken into account in the analysis presented in this thesis. However, the effect could be quite significant: if $\frac{\delta'+\delta''}{2} \simeq 0.01$ and $k \simeq 0.97$, the magnitude of the correction is equal to the asymmetry itself.

C.0.0.8 A_Y measurement using left/right data samples

The rotational symmetry of the Λ production cross-section allows to write equivalence expressions like

$$\mathrm{d}\sigma_L^{\uparrow} \equiv \mathrm{d}\sigma_R^{\downarrow} \tag{C.31}$$

The left and right samples therefore play the same role as the spin-up cell and spin-down cell samples discussed before, and the cross-section asymmetry can be written as

$$A_Y^{\uparrow} = \frac{\mathrm{d}\sigma_R^{\uparrow} - \mathrm{d}\sigma_L^{\uparrow}}{\mathrm{d}\sigma_R^{\uparrow} + \mathrm{d}\sigma_L^{\uparrow}} \equiv \frac{\mathrm{d}\sigma_R^{\uparrow} - \mathrm{d}\sigma_R^{\downarrow}}{\mathrm{d}\sigma_R^{\uparrow} + \mathrm{d}\sigma_R^{\downarrow}} = A_Y^R, \tag{C.32}$$

where $A_Y^{\uparrow}$ denotes the left/right asymmetry calculated from the target cell with spin oriented upward. The above expression involves the measurement of the counting rates only from one target cell, either the upstream or downstream. For an ideal apparatus this would be enough to get a correct result. A real experiment has on the other hand in general different acceptances for left- and right-produced lambdas. The error arising from the difference in the left/right acceptance can be corrected in a similar way as for upstream and downstream cells. This alternative approach has however some advantages:

1. the target polarization value for the left and right samples is exactly the same;

2. the larger acceptance of the downstream cell can be exploited in order to get an higher statistics;

3. the difference in the left/right acceptance is smaller than the upstream/downstream, and therefore the $\sqrt{1-\alpha^2}$ factor in the statistical error of the measured asymmetry is smaller.

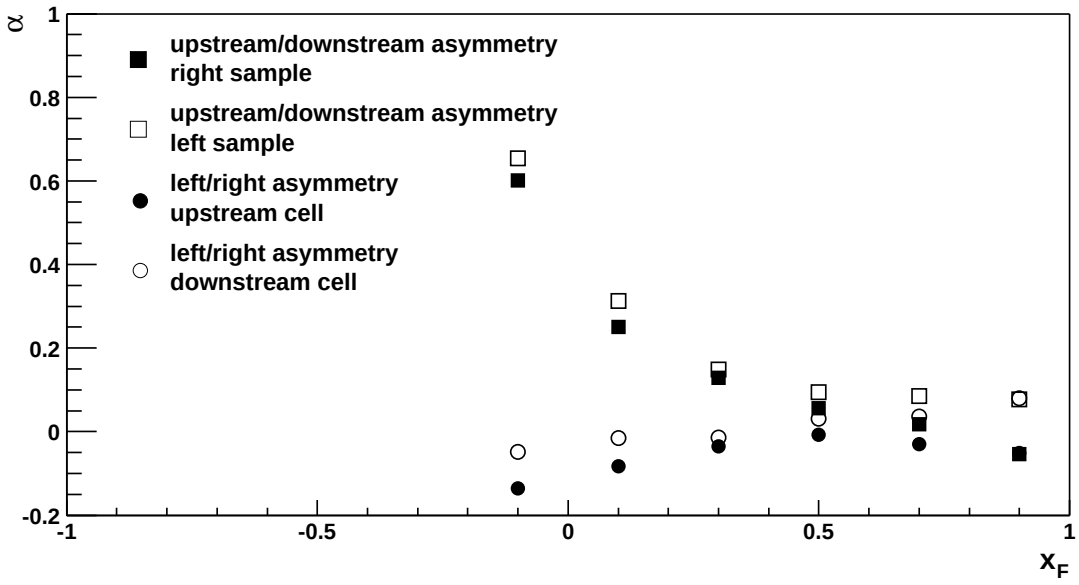

Figure C.1: *Values of α calculated from MonteCarlo analysis in transverse spin configuration. Circular marks represent $(a_R - a_L)/(a_R + a_L)$ for upstream and downstream cells, while rectangular marks represent $(a_d - a_u)/(a_d + a_u)$ for left and right samples.*

The last point is confirmed by the MonteCarlo analysis of the apparatus acceptance. Fig. C.1 shows the values of α as a function of x_F and p_T for upstream/downstream and left/right data sets.

References

[1] COMPASS, A Proposal for a COmmon Muon and Proton Apparatus for Structure and Spectroscopy, (CERN/SPSLC 96-14, SPSLC/P297, 1996).

[2] E.W. Hughes and R. Voss, Annu. Rev. Nucl. Part. Sci. **49** (1999), 303

[3] J. Ellis and R.L. Jaffe, Phys. Rev. **D 9** (1974), 1444; Phys. Rev. **D 10** (1974), 1669

[4] M. Vetterli, **hep-ph/9812420**.
Prepared for "Lake Louise Winter Institute: Quantum Chromodynamics", Lake Louise, Alberta, Canada, 15-21 Feb 1998.
In "Lake Louise 1998, Quantum chromodynamics", 49-98.

[5] G.K. Mallot, habilitationsschrift.

[6] J. Ashman *et al.*. Nucl. Phys. **B328** (1989), 1

[7] S.J. Brodsky, J. Ellis, M. Karliner, Phys. Lett. **B206-2** (1988), 309

[8] F. Bradamante, contribution to SPIN2000 conference.

[9] A. Bacchetta, PhD thesis.

[10] M. Alberg *et al.*, Phys. Lett. **B356** (1995), 113

[11] J. Ellis *et al.*, Nucl. Phys **A673** (2000), 256

[12] J. Ellis, D. Kharzeev and A. Kotzinian, Z. Phys. **C69** (1996), 467

[13] W. Lu and B. Ma, Phys. Lett. **B 357** (1995), 419

[14] M. Anselmino *et al.*, Phys. Lett. **B 481** (2000), 253

[15] M. Anselmino, contribution to the COMPASS Physics Workshop, September 2002.

[16] R.L. Jaffe, Phys. Rev. **D 54** (1996) no.11, 6581

[17] V. Barone *et al.*, Phys. Rep. **359** (2002), 1

[18] D. de Florina *et al.*, Phys. Lett. **B439** (1998) no.1/2, 176

[19] F. Sauli, *Principles of Operation of Multiwire Proportional and Drift Chambers*, Lectures given in the Academic Trining Programme of CERN 1975–1976, CERN 77–09, 3 Maggio 1977

[20] W. Blum, L. Rolandi, *Particle Detection with Drift Chambers*, Springer–Verlag

[21] G. Charpak, F. Sauli: Nucl. Instr. and Meth. **162** (1979), 405

[22] J. Fischer *et al.*: Nucl. Instr. Meth. Phys. Res. **A238** (1985), 248

[23] L.G. Christophorou *et al.*: Nucl. Instr. Meth. **163** (1979), 141

[24] F. Balestra et al., IEEE Trans. Nucl. Sci. **NS45** (1998), 868

[25] F.M. Newcomer et al., Nucl. Instr. and Meth. **A283** (1989), 806

[26] F.M. Newcomer et al., IEEE Trans. Nucl. Sci. **NS40** (1993), 630

[27] F.M. Newcomer et al., Nucl. Instr. and Meth. **A381** (1996), 355

[28] F. Gonnella and M. Pegoraro A prototype front-end asic for the read-out of the drift tubes of CMS barrel muon chambers, in: *fourth workshop on electronics for LHC experiments - LEB98, Rome, 21-25 September 1988* (CERN/LHCC/98-36) 257.

[29] G. Braun, et al. TDC chip and read-out driver developments for COMPASS and LHC experiments, in: *fourth workshop on electronics for LHC experiments - LEB98, Rome, 21-25 September 1988* (CERN/LHCC/98-36) 564.

[30] A. Maggiora et al. Fast front-end electronics for COMPASS MWPCs, in: *IEEE '99, Nuclear Science Symposium,, Seattle (USA), Oct. 26-28 (1999)* IEEE Trans. Nucl. Sci. **47** (2000), 791

[31] P. Barberis *et al.*, *http://wwwcompass.cern.ch/compass/notes/1998-9/1998-9.html*

[32] N. Dibiase *et al.*, *http://wwwcompass.cern.ch/compass/notes/1998-17/1998-17.ps.gz*

[33] N. Dibiase *et al.*, *http://wwwcompass.cern.ch/compass/notes/1999-4/1999-4.ps.gz*

[34] GEANT Documentation page: *http://wwwinfo.cern.ch/asd/geant/*

[35] CORAL Documentation page: *http://coral.cern.ch*